Title
Sum Frequency Generation Studies of Hydrogenation Reactions on Platinum Nanoparticles

Author
Krier, James Michael

Publication Date
2013

Peer reviewed|Thesis/dissertation

Sum Frequency Generation Studies of Hydrogenation Reactions on Platinum Nanoparticles

By
James Michael Krier

A dissertation submitted in partial satisfaction of the
requirements for the degree of

Doctor of Philosophy
in
Chemistry
in the
Graduate Division
of the
University of California, Berkeley

Committee in charge:
Professor Gabor A. Somorjai, Chair
Professor Heino Nitsche
Professor Kyriakos Komvopoulos

University of California
Berkeley, CA 94720

Fall 2013

Sum Frequency Generation Studies of Hydrogenation Reactions on Platinum Nanoparticles

By
James Michael Krier

Abstract

Sum Frequency Generation Studies of Hydrogenation Reactions

on Platinum Nanoparticles

By

James Michael Krier

Doctor of Philosophy in Chemistry

University of California, Berkeley

Professor Gabor A. Somorjai, Chair

Sum Frequency Generation (SFG) vibrational spectroscopy is used to characterize intermediate species of hydrogenation reactions on the surface of platinum nanoparticle catalysts. In contrast to other spectroscopy techniques which operate in ultra-high vacuum or probe surface species after reaction, SFG collects information under normal conditions as the reaction is taking place. Several systems have been studied previously using SFG on single crystals, notably alkene hydrogenation on Pt(111). In this thesis, many aspects of SFG experiments on colloidal nanoparticles are explored for the first time. To address spectral interference by the capping agent (PVP), three procedures are proposed: UV cleaning, H_2 induced disordering and calcination (core-shell nanoparticles). UV cleaning and calcination physically destroy organic capping while disordering reduces SFG signal through a reversible structural change by PVP.

Disordering is a dynamic and powerful way to perform SFG experiments on colloidal nanoparticles. Simply adding H_2 (a reactant) to Pt-PVP reduces signal of PVP by >90%, making

it possible to resolve intermediates. The selection rules of SFG indicate intensity may be reduced by a decrease in concentration or an increase in disorder. As H_2 dissociates on Pt, the bond between PVP and Pt is weakened and PVP is able to rearrange into an unstructured geometry. Disordering makes size-controlled SFG studies possible for the first time because with PVP left intact, the nanoparticles are much less likely to aggregate. As evidence that a chemisorbed reaction intermediate is can be monitored, cyclohexene hydrogenation is performed. When PVP is disordered and the particles are "solvent-cleaned," the distinct C-H stretch of adsorbed 1,4-cyclohexadiene (1,4-CHD) appears at 2765 cm^{-1}. In addition, the mechanism of hydrogenation of 1,3-butadiene (1,3-BD) at 75 °C is characterized using the disordering procedure. For larger Pt-PVP nanoparticles (4.6-6.7 nm), one major pathway is preferred (2-buten-1-yl). However, using smaller nanoparticles (0.9-1.8 nm), two major pathways exist (1-buten-4-yl and 2-buten-1-yl) and coincide with preference for full hydrogenation.

Growth in the aliphatic stretch range following H_2 dosing shows UV treatment is not able to produce "naked" nanoparticles. Although outer layers removed quickly, persistent C fragments remain near the Pt surface. The properties of residual fragments of PVP following UV treatment are very mystifying. PVP is known to block active sites on Pt and reduce turnover frequency for ethylene hydrogenation. (After three hours of UV treatment, ethylene hydrogenation increases tenfold.) However, it is shown that for methanol oxidation, residual fragments become impermeable and actually reduce the turnover rate. Under oxidation conditions, the regular capped Pt-PVP nanoparticles are more active than the same particles following PVP removal with UV treatment. As further evidence of this effect, cyclohexene hydrogenation is performed with different level of H_2. Residual fragments are permeable with H_2 and the 1,4-CHD

intermediate appears in the SFG spectrum. However, once H_2 is removed, chemisorbed 1,4-CHD completely disappears in favor of molecular (physisorbed) cyclohexene (not bonded to Pt). Even for a strongly bound dehydrogenated intermediate like 1,4-CHD, access to Pt is only possible with H_2. Under varying amounts of UV treatment (PVP removal), the mechanism of cyclohexene hydrogenation varies widely among 1,4-CHD, 1,3-cyclohexadiene and π-allyl. Removing PVP does not simply open equivalent sites but shifts the reaction mechanism in this case.

Using Stöber encapsulation, a variety of PVP-capped catalysts can be coated in a thin porous SiO_2 shell (5-10 nm) and used for *in situ* characterization. Surrounding the catalyst with SiO_2 allows PVP to be thoroughly removed without compromising morphology. It is shown that alloying Pt with Sn (with SiO_2 shell) allows a new reaction mechanism of CO oxidation to take place which is not limited by surface O_2 concentration (as on pure Pt). In addition, 1,3-BD hydrogenation on 4 nm Pt@SiO_2, Pd@SiO_2 and Rh@SiO_2 is studied with SFG. Previous work shows Pd makes only partially hydrogenated products while Pt makes all products. SFG and kinetic experiments indicate multiple pathways (1-butene-4-yl, butan-1,3-diyl and 2-buten-1-yl) are possible on Pt@SiO_2 while only one (2-buten-1-yl) is favored on Pd@SiO_2. This work is the first SFG reaction selectivity study on core-shell nanoparticles. Using catalysts inside SiO_2 shells in dense 2-D films, it may become possible to assess industrial 3-D catalysts at a molecular level.

Table of Contents

Acknowledgements

I am grateful for the opportunity to study at UC-Berkeley and to work with many talented people in the Somorjai group. After going to high school a few miles away in the Bay Area and admiring Berkeley, getting admitted to the chemistry PhD program remains one my best memories. First and foremost, I would like to extend my most sincere thanks to Professor Gabor Somorjai. I have an interesting and rewarding project at LBL exploring new science and this is a direct result of the plans he put in place over the years. Professor Somorjai has innate leadership skills and has created countless opportunities for the people that have come through his group. In addition, I thank Inger Coble for her help planning group meetings and for countless small favors over four years in the group. Inger was an enormous help when I needed her the most. I also thank Professor Kyriakos Komvopoulos, a longtime collaborator of the Somorjai group. I am grateful for his scientific feedback – especially in manuscript editing – and for generous funding through his KAUST grants.

Although I performed SFG independently, I have been fortunate to have a number of excellent collaborators. First, I would like to thank Dr. William Michalak for his experimental contributions to this thesis and for his advice during two years of collaborating. Will has more catalysis expertise than any postdoc in the group and helped to focus my project around the most interesting questions in the field. I would also like to thank Dr. Hailiang Wang for giving me the opportunity to work with him on his Pt-Fe experiments. And I thank Dr. Andreas Sapi for sharing his ethylene hydrogenation results and allowing me to do SFG based on his specifications. Although I did not directly collaborate with Dr. Selim Alayoglu, I thank him for

his advice and assistance over all four years. Selim is incredibly generous with his time and was willing to offer his expertise on nanosynthesis and electron microscopy to anyone who asks. Furthermore, I thank Rebecca, Kwangjin, Feifei, Robert, Chris, Griffin, Walter, Lindsay, Gerome, Fan, Rob and other members for their advice and assistance. Lastly, I thank Dr. Joel Henzie (from Professor Peidong Yang's group) for the opportunity to study in Japan for a few weeks at the National Institute of Materials Science prior to beginning work at Intel.

I would also thank my mom and step dad, Scott, for support and encouragement throughout graduate school. I have learned so much from them over the years and it helped me complete my PhD. I also thank Professor Gilbert Nathanson at UW-Madison for his mentorship during my undergraduate research project before coming to Berkeley.

This work was generously supported by the U.S. Department of Energy under Contract no. DE-AC02-05CH11231. Additional funding is provided by UCB−KAUST Academic Excellence Alliance (AEA) Program (through Professor Kyriakos Komvopoulos) and the Honda Corporation.

Chapter 1: Introduction

The standard of living enjoyed in the industrialized world is thanks in large part to the discovery of catalysis. With a range of noble metals developed in the laboratory, crude oil and other natural resources are converted into transportation fuels, pharmaceuticals and a near infinite number of commodity chemicals.[1] Crop fertilizer with ammonia from the Haber-Bosch process made food affordable and is a major contributor to the worldwide population increase in the past century. Today, two thirds of the GDP in the United States involve a catalyst in one stage of production. From an economic perspective, focus on catalysts is easy to justify, however, it is not trivial to explain why chemical reactions occur on metals in the first place. In 1817, Englishman Humphry Davy conducted the one of the first systematic inquiries in this field. He documented visible changes on metals in reaction conditions, noting platinum and palladium were effective for the oxidation of coal gas at high temperatures while silver, iron, zinc and gold were inactive. Since Davy catalytic processes on many metal compositions, including alloys, have been refined through mostly empirical methods.

The importance is widely recognized but catalysis is often referred to as “black box” technology. Good catalysts were identified by guess-and-check because few techniques can legitimately assess molecular processes on a metal surface. The experimental challenges are enormous: there are eight orders of magnitude separating surface and bulk phases, making most chemical characterization methods inapplicable to surface science. However, in the past fifty years, fundamental techniques have emerged, beginning with Low Energy Electron Diffraction (LEED). Using LEED, early studies demonstrated that metals restructure when molecules adsorb – a revolutionary idea at the time.[2] More techniques became available like X-ray Photoelectron

Spectroscopy (XPS), Auger, Scanning Tunneling Microscopy (STM), Electron Energy Loss Spectroscopy (EELS) and Reflection Adsorption Infrared Spectroscopy (RAIRS). These experiments reveal composition (Auger, XPS), oxidation state (XPS), morphology (STM) and molecular vibrations of adsorbed hydrocarbons (RAIRS and EELS) from the surface of heterogeneous catalysts. When used together, they provide a fundamental picture of adsorption and reaction processes. Nonetheless, a limitation of traditional surface techniques is the requirement for ultra-high vacuum conditions. In XPS, for example, the ejected photoelectrons must not undergo inelastic collisions before arriving at a hemispherical analyzer. (Traditional XPS experiments are performed at $<10^{-8}$ Torr.) The requirement for low pressures is a major hurdle for studying industrial catalysts which operate at ambient or elevated pressures. Because of the "pressure gap," catalysis research has been a balancing act between the acquisition of fundamental information and the simulation of relevant conditions.

The modern era of surface science has seen the development of fundamental characterization techniques which operate close to atmospheric pressure. For example, Ambient Pressure X-ray Photoelectron Spectroscopy (AP-XPS) at the Advanced Light Source at Lawrence Berkeley National Laboratory can run over 1 Torr. In addition, Sum Frequency Generation (SFG) vibrational spectroscopy with ultrafast lasers was first implemented at Berkeley and can probe reaction intermediates on metal catalysts under any reaction cell laser pulses can penetrate. Because SFG signal must originate from a surface, the concentration factors in surrounding bulk media are irrelevant, so any temperature and pressure regime is theoretically plausible.
Using SFG to study noble metal single crystal catalysts, researchers in the Somorjai group have studied many surface phenomena. Cremer *et al.* observed ethylidyne, di-σ ethylene and ethyl

species during ethylene hydrogenation on Pt(111).[3] This work was interpreted and compared using ultra-high vacuum data. Yang *et al.* documented interesting effects by simply adding the hexane to Pt(111) in the presence or absence of H_2.[4] When hexane was flat-lying there were asymmetric and symmetric CH_2 and CH_3 vibrations. When hydrogen was evacuated from the cell, hexane dehydrogenated to benzene. (Because all C-H vibrations are in-plane with the Pt(111) surface, no SFG signal is generated.) When the hexane chain is standing up (e.g., hexylidyne), the spectrum was dominated by a CH_3 symmetric (very little CH_2 contribution) despite that the molecule still has CH_2 groups. SFG spectra can indicate the presence of organic species and suggest orientation.

The first SFG investigation into reaction selectivity on Pt(111) was cyclohexene hydrogenation.[5] The chemisorbed intermediates of this reaction under most conditions are 1,3-cyclohexadiene (1,3-CHD), 1,4-cyclohexadiene (1,4-CHD) and π-allyl. The reaction processes of cyclohexene are well-studied with SFG (more than any other hydrogenation reaction) because the vibrational signatures of each intermediate are mutually exclusive from one another, making spectral analysis straightforward. In addition, molecular 1,3-CHD and 1,4-CHD are stable and can be studied independently with kinetic tests to correlate SFG spectra with catalytic activity. The 1,3-CHD hydrogenation reaction has a higher turnover frequency and produces less benzene than 1,4-CHD hydrogenation on Pt(111).[6] In addition, the SFG spectrum for 1,3-CHD shows less chemisorbed 1,4-CHD. Using this information, it can be inferred that the reduction of 1,4-CHD peak intensity from the SFG spectra of Pt(111) during cyclohexene hydrogenation results in higher turnover.

Single crystals provide well-defined surfaces and are treated as model systems for catalysis studies. However, most noble metal catalysts used in industry are nanoparticles. Metal ions are loaded into high surface area mesoporous supports (wet impregnation) and reduced at high temperature to create nanoparticle islands. Because industrial catalysts are not monodispersed, colloidal synthesis recipes have been developed which create size and shape controlled 0.5-10 nm platinum nanoparticles. The control of size of 0.5-3 nm Pt is particularly important because below ~2 nm, electronic structure changes and reaction selectivity can shift dramatically.[7] In one recent example, the hydrogenation of furfural was shown to depend strongly on nanoparticle size.[8] For 1-2 nm Pt-PVP, decarbonylation is preferred and furan is the dominant product.[8] As size is increased >3 nm, the activation barrier for C=O hydrogenation is decreased and furfuryl alcohol becomes dominant. The focus of this thesis is SFG studies of reaction selectivity on size-controlled nanoparticle catalysts. Preliminary studies are performed with cyclohexene because the 1,4-CHD intermediate has a strong signature in a unique wavenumber region and there is so much existing literature on this reaction and related reactions on Pt(111). Because the 1,4-CHD peak is highly red-shifted, it provides unambiguous evidence of a chemisorbed molecule on Pt. Through my time in Berkeley, I have resolved the 1,4-CHD peak (2765 cm^{-1}) on three types of Pt nanoparticle systems: UV cleaned, H_2 disordered and calcined core-shell nanoparticles.

A major point of contention of SFG experiments on nanoparticle catalysts arises from the following issue: what should be done with the capping agent? All nanoparticles made in colloidal synthesis become enveloped with an organic ligand such as polyvinyl pyrrolidone (PVP), tetradecyltrimethylammonium bromide (TTAB) or oleylamine. The organic ligand stabilizes small clusters in solution and makes nanosynthesis possible. However, the presence of CH_2 and

CH_3 groups on the surface of the nanoparticles make SFG experiments challenging. The strong SFG background in the aliphatic range overlaps with CH_2 and CH_3 stretches of reaction intermediates. Therefore, the cap must either be removed or somehow minimized to use SFG to study reaction selectivity on nanoparticles.

Chapter 3 of this thesis directly addresses the issue of SFG studies on capped Pt-PVP nanoparticles. UV cleaning (UV-ozone) removes PVP and allows for SFG experiments to be performed on nanoparticles. However, one drawback of removal is the possibility of aggregation. It is shown that 4.2 nm Pt-PVP nanoparticles typically remain stable immediately following UV cleaning but tend to aggregate when exposed to hydrogenation reaction conditions. Instead of fully removing the capping agent, it is advantageous to disorder PVP by adding hydrogen gas. It is shown that as hydrogen dissociates on platinum, PVP is restructured into a disordered geometry which dramatically reduces SFG signal. Because SFG is a coherent laser process, vibrational modes must have concentration and order. No matter how concentrated PVP is, it can be diminished in SFG spectra by effective disordering. And because PVP remains around the nanoparticle, the tendency to aggregate is significantly reduced. Figure 1 shows adsorbed 1,4-CHD on 4.2 nm Pt-PVP during cyclohexene hydrogenation. Using the disordering procedure, it is possible for the first time to study reaction selectivity as a function of size on Pt-PVP.

Because cyclohexene and molecular 1,4-CHD produce the same distinct peak (2765 cm^{-1}) in SFG spectra (during reaction and in ultra high vacuum), they were thought to produce the same adsorbed surface species when introduced to Pt(111).[5] SFG spectra taken before, during and after cyclohexene and 1,4-CHD hydrogenation on Pt-PVP show there are “reactive” and “unreactive” forms of adsorbed 1,4-CHD. Cyclohexene and 1,4-CHD hydrogenation proceed through

mutually exclusive pathways. The 1,4-CHD peak quickly disappears when H_2 is recirculated after cyclohexene hydrogenation conditions. In contrast, 1,4-CHD hydrogenation proceeds very slowly and results in persistent poisoning of the Pt surface. This data is still being analyzed and should appear in publication shortly.

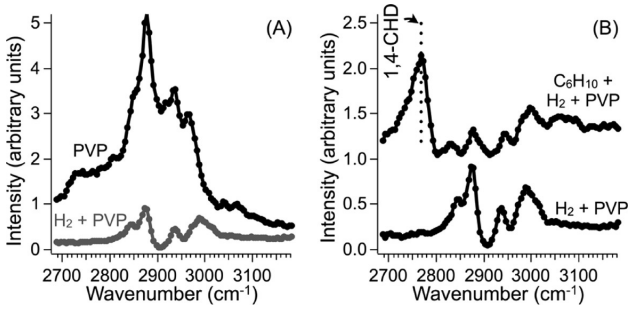

Figure 1: SFG spectra of solvent-cleaned 4.2 nm Pt-PVP nanoparticles obtained at 298 K in different atmospheres: (A) 760 Torr Ar (top) and 200 Torr H_2, 560 Torr Ar (bottom) and (B) 10 Torr C_6H_{10}, 200 Torr H_2, 550 Torr Ar (top) and 200 Torr H_2, 560 Torr Ar (bottom). Spectra shown in (B) are offset for clarity. Unlabeled features are attributed to PVP.

Although UV cleaning can remove most PVP in less than an hour of treatment, that does not mean "naked" Pt nanoparticles are generated. It is difficult to prepare atomically clean nanoparticles and the nature of remaining carbon fragments is not well understood. In Chapter 4, it is shown that residual PVP fragments can have a pronounced impact on catalytic activity. For ethylene hydrogenation, there is ~10X increase in activity following UV cleaning which is expected because PVP is thought to block active sites. However, for methanol oxidation, there is a major decrease in activity following UV cleaning. Residual PVP fragments block Pt under oxidation conditions. When hydrogen is introduced, the fragments do not bind tightly to Pt and active sites are liberated. In addition, when no hydrogen is present, adsorption of 1,4-CHD – a

strongly chemisorbed intermediate of cyclohexene hydrogenation – is inhibited in favor of molecular cyclohexene that is not strongly bound to platinum.

SFG experiments on core-shell nanoparticles were also performed. Using a modified Stöber synthesis method, relatively thin, porous shells of SiO_2 can be created around almost any metal nanoparticle surrounded by PVP. Encapsulated Pt nanoparticles can be aggressively calcined like 3-D industrial catalysts, and despite close proximity within the shell, they do not appear to aggregate (Figure 2). In addition, Pt@SiO_2 can be used with in similar experimental protocols used for Pt-PVP for SFG experiments, including Langmuir Blodgett film deposition. Figure 2 shows the 1,4-CHD intermediate on 4 nm Pt@SiO_2. As a reaction selectivity study, butadiene hydrogenation was compared with SFG for 4 nm Pt@SiO_2, Pd@SiO_2 and Rh@SiO_2. While Pd produces almost exclusively partially hydrogenated products (butenes), butane is a significant product on Pt and Rh. The SFG spectra of reaction intermediates is recorded for Pt@SiO_2 and Pd@SiO_2, and the selectivity difference produced on Pd@SiO_2 is attributed to a preference for the 2-buten-1-yl radical (2B1R) and exclusion of butan-1,3-diyl radical (B13R). The most intense peak in the Pt@SiO_2 SFG spectrum is a CH_2 asymmetric stretch, which cannot be produced by 2B1R (CH_3 stretch only). This data is still being analyzed and should appear in publication shortly.

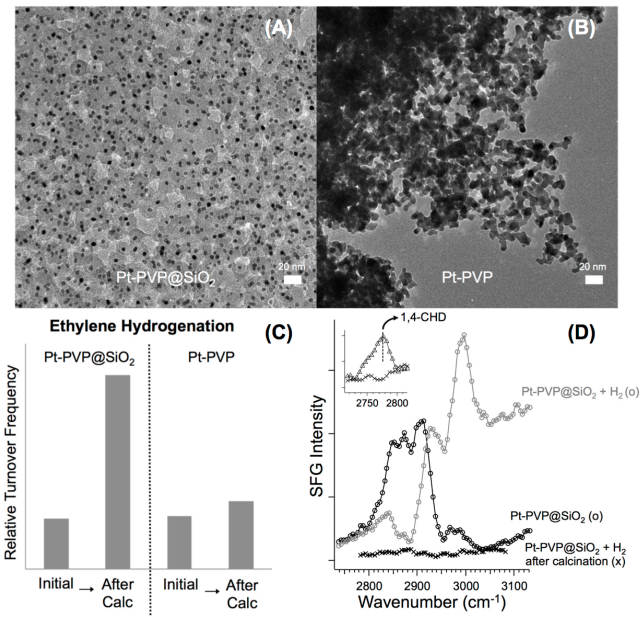

Figure 2: (A) Pt-PVP@SiO_2 after 10 min calcination in air at 350 °C. (B) Pt-PVP after 10 min calcination in air at 350 °C. (C) Ethylene hydrogenation rate before and after calcination (normalized to the initial rate for clarity). (D) SFG spectra showing Pt-PVP@SiO_2 in 760 Torr Ar (o), in 100 Torr H_2 and 660 Torr Ar (o) and in 100 Torr H_2 and 660 Torr Ar after calcination (x). The inset image shows the baseline spectrum (100 Torr H_2 and 660 Torr Ar after calcination) followed by 1,4-CHD hydrogenation conditions (2 Torr 1,4-CHD, 100 Torr H_2 and 660 Torr Ar).

Chapter 5 discusses 1,3-butadiene hydrogenation on 0.8, 1.8, 4.6 and 6.7 nm Pt-PVP nanoparticles at 75 °C. Four products are produced by this reaction: butane, 1-butene, trans-2-butene and cis-2-butene. For 0.9 and 1.8 nm Pt-PVP butane is the primary product while 1-butene is the primary product for 4.6 and 6.7 nm Pt-PVP. SFG spectra for this reaction show more CH_2 stretch intensity for 0.9 and 1.8 nm compared to 4.6 and 6.7 nm. The reaction intermediates of 1,3-butadiene hydrogenation are previously determined with density functional theory calculations on Pt(111), so one can postulate that the SFG results indicate an increased presence of the 1-buten-4-yl radical (1B4R) on 0.9 and 1.8 nm Pt-PVP (Figure 3).

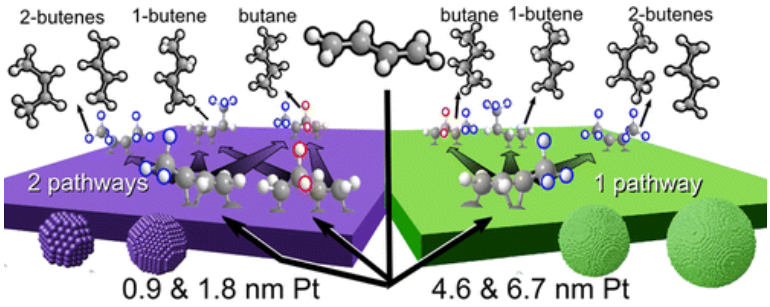

Figure 3: Preferred 1,3-butadiene reaction pathways on size-controlled Pt-PVP.

Using *in situ* X-ray photoelectron spectroscopy with colloidally prepared, monodisperse ~2 nm Pt and PtSn nanoparticle catalysts, it is shown in Chapter 6 that the addition of Sn to Pt provides a distinctly different reaction mechanism for CO oxidation compared to pure Pt. The kinetic mechanism of CO oxidation on PtSn catalysts is not limited by O_2 adsorption as on pure Pt catalysts. Instead, the PtSn catalyst is highly populated by O on the surface and subsurface regions of Sn. While pure Pt catalysts displayed a reaction mechanism with an activation barrier of 133 kJ/mol, the PtSn catalysts displayed a reaction mechanism with an activation barrier of 35 kJ/mol. While chemical signatures of Pt and Sn indicated intermixed metallic components under reducing conditions, Pt and Sn were found to reversibly separate into isolated domains of Pt and Sn oxide on the nanoparticle surface under reaction conditions of 100 mTorr CO and 40 mTorr O_2 between temperatures of 200-275 ˚C. The significant differences in activation barriers, zero-order dependence in O_2, and appearance of partially oxidized Sn indicate that enhanced activity is due to a reaction mechanism that occurs at a Pt/Sn-oxide interface present at the nanoparticle surface.

In Chapter 7, 2 nm Pt-Fe bimetallic nanoparticles with tunable composition are compared based on hydrogenation rate. The turnover rates of ethylene and cyclohexene hydrogenation were increased by incorporation of Fe into Pt nanoparticles. This is relatively unexpected because Pt is the only active metal for hydrogenation (adding Fe would presumably just reduce active sites). SFG vibrational spectroscopy indicated that the activity enhancement is achieved by displacing less active intermediates of the catalyst surface (Figure 4). It appears that Fe changes the electronic structure or disrupts three and four fold sites of Pt. By blocking three and four fold sites, strongly adsorbed intermediates which are less active do not form and the catalyst is more active. In ethylene hydrogenation, ethylidyne is less active than di-σ-bonded ethylene.

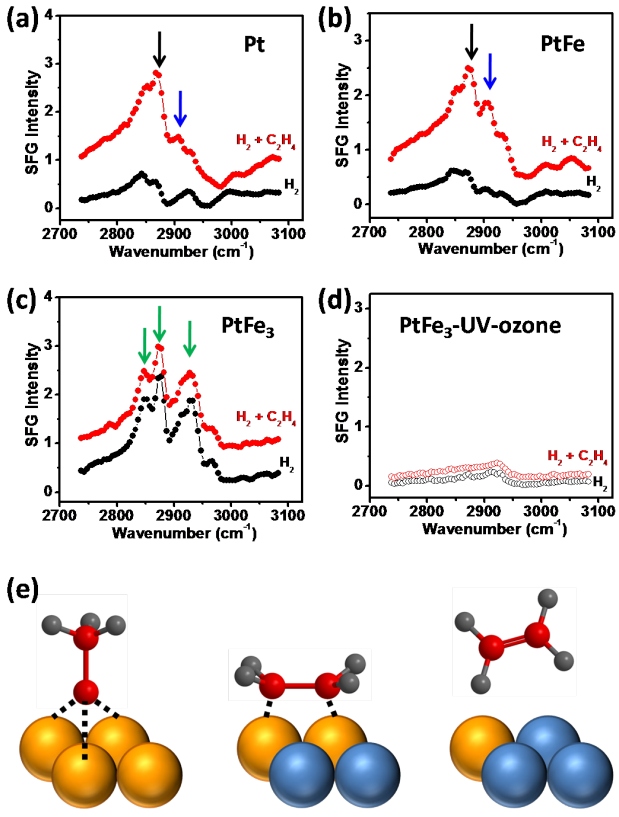

Figure 4: SFG vibrational spectroscopy study of ethylene intermediates adsorbed on the surface of Pt, PtFe and $PtFe_3$ nanoparticles under hydrogenation reaction conditions. SFG vibrational spectra of 2 nm (a) Pt, (b) PtFe, (c) $PtFe_3$ and (d) UV-ozone treated $PtFe_3$ nanoparticles obtained

at 20 °C under hydrogen and ethylene hydrogenation conditions. The cell was first filled with 100 Torr of H_2 and 660 Torr of Ar (black curves). Then the cell was evacuated and filled with 35 Torr of C_2H_4, 100 Torr of H_2 and 625 Torr of Ar (red curves). Black and blue arrows in (a) and (b) mark the vibrational frequencies of ethylidyne (~2875 cm^{-1}) and di-σ-bonded ethylene (~2910 cm^{-1}) adsorbed on the catalyst surface, respectively. The green arrows in (c) mark the vibrational frequencies of PVP on the nanoparticle surface. (e) Schematic illustration of ethylidyne adsorbed on Pt surface (left), di-σ-ethylene adsorbed on PtFe surface (middle), and weak ethylene interaction with the $PtFe_3$ surface (right).

A theme among all chapters is maintaining the integrity of nanoparticles during *in situ* characterization. Because almost every fundamental technique – SFG, STM, XPS, EXAFS, etc. – uses 2-D samples, nanoparticles are inherently close together. When exposed to reactions conditions, nanoparticles may migrate and collide with one another during surface diffusion, and shape changes and aggregation may occur. In contrast, nanoparticles on industrial 3-D catalysts may be separated by hundreds of nanometers, making aggregation unlikely. Future efforts will propose new ways to sustain stability and explore the degree to which dense 2-D samples can duplicate real-world reactions in 3-D.

The focus of this project was to address how SFG can be performed on nanoparticle catalysts to monitor hydrogenation reactions. Disordering, UV cleaning and calcination (core-shell) are effective in removing the cap signal and showing reaction intermediates for a variety of colloidal nanoparticles. Calcination and UV cleaning remove PVP, while under H_2 gas, PVP can be disordered to reduce SFG signal. In light of these SFG procedures, organic capping may be

viewed as a nuisance but further research may use the cap to creatively tune catalytic properties. The key to disordering is the lower adsorption energy of PVP on Pt. As H_2 dissociates, PVP becomes "unhinged" from the Pt surface. If a reaction pathway is found to depend on PVP or some other capping agent, then the reaction may be tuned by the degree of disordering – a quantity which can be closely monitored with SFG. This approach may provide a new way to adjust the electronic structure of surface Pt. Because many catalysts operate in the presence of surface carbonaceous fragments – either there initially or accumulated during reaction – it is likely that reaction pathways can be adjusted through rearrangements of such fragments.

References

(1) Norskov, J. K.; Bligaard, T.; Rossmeisl, J.; Christensen, C. H. *Nature Chemistry* **2009**, *1*, 37.

(2) Somorjai, G. A.; Li, Y. *Introduction to surface chemistry and catalysis*; Wiley, **2010**.

(3) Cremer, P.; Stanners, C.; Niemantsverdriet, J. W.; Shen, Y. R.; Somorjai, G. *Surf. Sci.* **1995**, *328*, 111.

(4) Yang, M.; Somorjai, G. A. *Journal of the American Chemical Society* **2004**, *126*, 7698.

(5) Su, X. C.; Kung, K.; Lahtinen, J.; Shen, R. Y.; Somorjai, G. A. *Catalysis Letters* **1998**, *54*, 9.

(6) McCrea, K. R.; Somorjai, G. A. *Journal of Molecular Catalysis A-Chemical* **2000**, *163*, 43.

(7) Li, L., *et al. The Journal of Physical Chemistry Letters* **2012**, *4*, 222.

(8) Pushkarev, V. V.; Musselwhite, N.; An, K.; Alayoglu, S.; Somorjai, G. A. *Nano Letters* **2012**, *12*, 5196.

Chapter 2: Sum Frequency Generation Vibrational Spectroscopy and Complementary Characterization Techniques

The primary focus of this thesis is to detect reaction intermediates on nanoparticle catalysts under ambient conditions. To achieve this, sum frequency generation (SFG) vibrational spectroscopy was used and in the subsequent sections both the background theory (including Raman and infrared spectroscopy) and the laboratory protocols of the laser system are discussed in detail. In contrast to SFG experiments on single crystals, all nanoparticle experiments were performed on monolayer films with total internal reflection laser geometry. And because no single technique can answer all relevant questions, complementary experiments were performed, including transmission electron microscopy (TEM) for imaging, X-ray photoelectron spectroscopy (XPS) for chemical composition, and gas chromatography (GC) for kinetics. Using multiple *in situ* characterization techniques with atomic and molecular-level detail with reaction statistics, it is possible to understand fundamental factors that affect catalysts operating under normal conditions.

2.1 Vibrational Spectroscopy with Raman and Infrared

The Raman effect occurs when an inelastic scattering elicits a shift in energy of incident light (often visible or ultraviolet). When an organic molecule is irradiated with visible light, three electronic transition events are possible: Stokes, Rayleigh and anti-Stokes scattering (Figure 2.1). The most likely scattering process is elastic scattering where an electron is excited to a virtual state and simply decays to the original energy level (Rayleigh). Rayleigh scattering does not yield chemical information since the same energy photon is generated before and after excitation. Stokes and anti-Stokes, however, both can be used to determine the change in energy from the

ground state to the first excited state (ΔE_υ). The ratio of Stokes and Anti-Stokes Raman peaks depends on the initial population of the first excited state and follows a Boltzmann distribution according to temperature. At high temperatures more molecules are excited and the intensity of Anti-Stokes peaks increases.

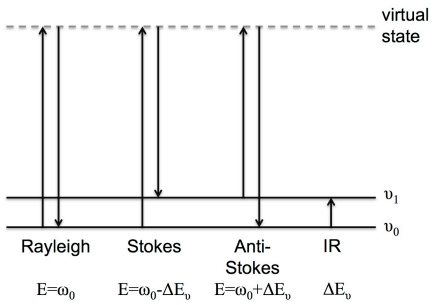

Figure 2.1: Rayleigh, Stokes, Anti-Stokes and infrared (IR) transitions involved in Raman and IR vibrational spectroscopy.

When inelastic scattering occurs from a photon onto a molecule an electron changes energy levels resulting in a shift in dipole moment. The dipole moment with an external oscillating electric field is linearly proportional to the polarizability of the chemical bond:

$$\mu = \alpha E_0 \cos(2\pi \nu t)$$

As the bond vibrates and changes shape along the normal coordinate q, polarizability also changes. The polarizability can be expressed as:

$$\alpha = \alpha_0 + \frac{\partial \alpha}{\partial q} q_0 \cos(2\pi \nu t)$$

Where q_0 is the equilibrium position, α_0 is initial polarizability and ν_1 is the frequency of the vibration. Rearranging the two previous equations gives:

$$\mu = \alpha_0 E_0 \underbrace{\cos(2\pi(\nu)t)}_{\text{Rayleigh}} + \frac{\partial\alpha}{\partial q}\frac{E_0 q_0}{2}[\underbrace{\cos(2\pi(\nu-\nu_1)t}_{\text{Stokes}} + \underbrace{\cos(2\pi(\nu+\nu_1)t)}_{\text{Anti-Stokes}}]$$

The three terms in the expression correspond to Rayleigh, Stokes and Anti-Stokes transitions discussed previously. In addition, the differential term reveals the major selection rule of Raman spectroscopy (shown below): polarizability must change during the vibration for a mode to be Raman active.

$$\left(\frac{\partial\alpha}{\partial q}\right) \neq 0$$

Infrared spectroscopy involves a molecule absorbing a photon and being excited from the ground vibrational level to an excited state with higher energy (i.e., $\upsilon_0 \rightarrow \upsilon_1$). By measuring absorption at different wavelengths, the presence of distinct chemical groups can be determined. By definition, the dipole moment must change with the normal coordinate (q):

$$\left(\frac{\partial\mu}{\partial q}\right) \neq 0$$

This selection rule is illustrated in Figure 2.2, which shows two stretching vibrations of ethylene, symmetric and asymmetric. Only asymmetric stretching is infrared active because of the net change in dipole during symmetric stretches cancel.

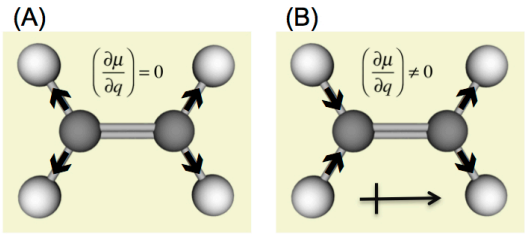

Figure 2.2: (A) Ethylene CH_2 symmetric stretch. (B) Ethylene CH_2 asymmetric stretch. Only the asymmetric vibration is infrared active.

2.2 Non-Linear Effects of Light and Sum Frequency Generation

When an oscillating electric field from light propagates through a material, a force is applied which perturbs electrons away from equilibrium locations.[1] The induced dipole created by the movement of an electron relates to the applied electric field (E), polarizability (α) and dipole (μ):

$$\mu = \mu_0 + \alpha E$$

When considering an ensemble of electrons in a large molecular system, the polarization (P) is useful for representing the cumulative change in dipole moment in a fixed volume. A Taylor series expansion of the polarization expression can be expressed as:

$$P = P^{(1)} + P^{(2)} + \cdots = \varepsilon_0(\chi^{(1)}E + \chi^{(2)}E^2 + \cdots)$$

where ε_0 is the vacuum permittivity and $\chi^{(1)}$ and $\chi^{(2)}$ are the first order and second order (linear and non-linear) susceptibilities, respectively. When the dipole oscillation occurs at the frequency of the electric field of incident light, the emitted photon matches the incoming photon (due to linear polarization). Linear behavior can explain the many observed properties of light including reflection and scattering. However, using high-powered pulsed lasers, non-linear behavior can be observed as the applied electric field begins to match the force felt by electrons in atoms. Analysis of the energy shifts resulting from non-linear activity can provide information about the surface of materials.

If we consider two separate photons from an SFG laser system, the second order polarization is expressed this way:

$$P^{(2)} = \varepsilon_0 \chi^{(2)}(E_1 \cos(\omega_1 t) + E_2 \cos(\omega_2 t))^2$$

where the E_1 and E_2 terms reflect the electric field of each incident laser beam. When the equation is expanded, more terms appear:

$$P^{(2)} = \varepsilon_0 \chi^{(2)}(E_1^2 + E_2^2 + E_1^2 \cos 2\omega_1 t + E_2^2 \cos 2\omega_2 t + \frac{1}{2} E_1 E_2 \cos(\omega_1 + \omega_2)t + \frac{1}{2} E_1 E_2 \cos(\omega_1 - \omega_2)t)$$

The 2ω terms reflect second harmonic generation of identical photons, which for the case of visible light radiation, is used to probe electronic transitions. Both E^2 terms are electric fields which do not depend on wavelength. Sum frequency generation ($\omega_1+\omega_2$) and difference frequency generation ($\omega_1-\omega_2$) involve photons with different energy and these processes can reveal the vibrational transitions at a surface or interface.

The selection rules and surface sensitivity of SFG vibrational spectroscopy originate from the second order non-linear susceptibility, $\chi^{(2)}$.[1] In bulk centrosymmetric media, the macroscopic average of $\chi^{(2)}$ is zero because the upward environment equals the downward ($\chi^{(2)}_{xyz} = \chi^{(2)}_{-x-y-z}$). However, at an interface inversion symmetry is broken and $\chi^{(2)} \neq 0$ and SFG signal can be created. Considering resonant (R) and non-resonant (NR) effects, $\chi^{(2)}$ can be expressed as:

$$\chi^{(2)} = \chi^{(2)}_{NR} e^{i\phi} + \chi^{(2)}_{R} e^{i\theta}$$

where each $\chi^{(2)}$ term has both a magnitude and phase. For vibrational spectroscopy and chemical analysis, the resonant contributions are more important than non-resonant contributions. In fact, there have been efforts to suppress non-resonant features so resonant peaks can be identified

without interference in SFG vibrational spectra. The origin of non-resonance can be somewhat ambiguous, however, resonant features directly originate from molecular vibrations:

$$\chi_R^{(2)} = \frac{A_q}{\omega_{IR} - \omega_q + i\Gamma}$$

where A_q, ω_{IR}, ω_q, and Γ are vibrational amplitude, infrared frequency, qth vibrational mode frequency and damping factor (broadening), respectively. The amplitude is proportional to infrared and Raman transitions (discussed in earlier sections):

$$A_q \propto \left(\frac{\partial \mu}{\partial q}\right)\left(\frac{\partial \alpha}{\partial q}\right)$$

Therefore, vibrations present in SFG spectra must be both Raman and infrared active. The SFG photon equals the energy of the visible photon plus the infrared photon, which also matches the energy of an anti-Stokes transition in Raman spectra (Figure 2.3). SFG with tunable infrared 2700-3200 cm^{-1} (used in this thesis), aliphatic and aromatic C-H stretches can be identified at an interface.

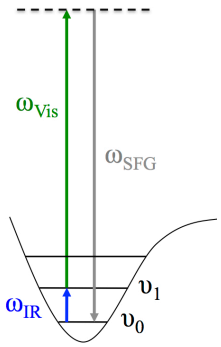

Figure 2.3: Schematic of sum frequency generation (SFG) vibrational spectroscopy with visible and infrared light. First, a vibration is stimulated ($\upsilon_0 \rightarrow \upsilon_1$), followed by an excitation to a virtual electronic state. When both processes are coupled together, the energy visible and infrared photons combine to make one SFG photon.

2.3 Sum Frequency Generation Vibrational Spectroscopy Laser System

All SFG experiments described herein were conducted using 20 ps pulse widths with 532 nm visible and 2700-3200 cm^{-1} tunable infrared (Figure 2.4). The lasing material itself is a Nd:YAG (Continuum Leopard D-20). In the oscillator, the picosecond pulse is generated and then dumped into the amplifier where intensity is increased two orders of magnitude. The oscillator is responsible for generating a temporally narrow pulse and maintaining stable output into the amplifier. Several components allow relatively crude electronic excitation from flash lamps to be finessed into consistent, narrow pulses with high power density. To create SFG, the outgoing 1064 nm pulse (~20 mJ) is passed through a series of non-linear optics, which will be discussed in detail in subsequent sections.

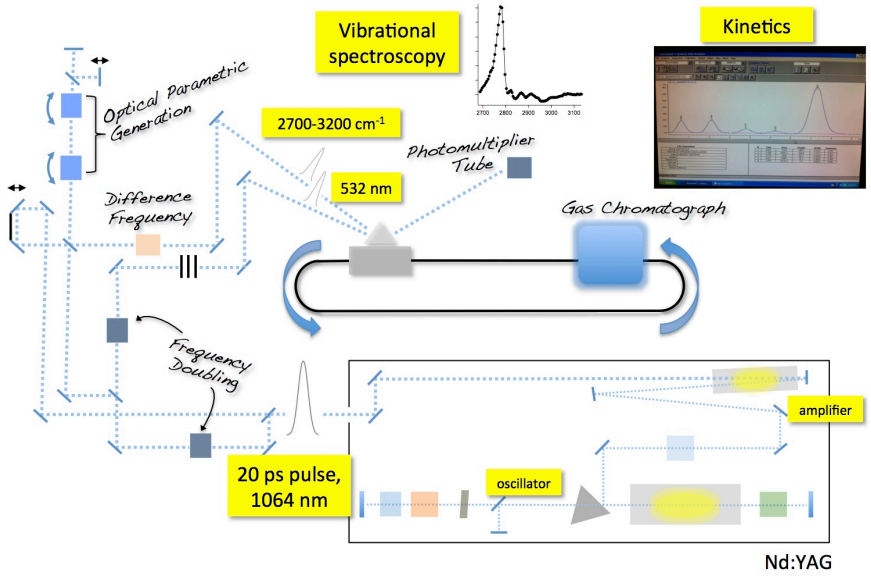

Figure 2.4: Picosecond sum frequency generation (SFG) vibrational spectroscopy system with gas chromatography. The aliphatic and aromatic C-H stretching range (2700-3200 cm^{-1}) is scanned with SFG as reactions are taking place on nanoparticle catalysts under ambient conditions. Kinetic data such as reaction rate, reaction selectivity and activation barriers can be monitored as SFG spectra are collected.

Light is first generated in the oscillator (Figure 2.5) as flash lamps are run at a 20 Hz repetition rate. Initially, light is emitted spontaneously in an uncontrolled fashion. However, as the first photons hit the end mirrors of the cavity and bounce back through the Nd:YAG rod, stimulated coherent emission – a process critical to all lasers – begins to occur. By having a closed loop for light to pass back and forth between end mirrors through the laser rod, the beam gradually amplifies itself into a consistent packet of photons with the same wavelength.

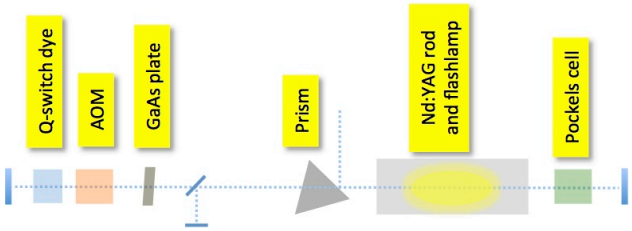

Figure 2.5: Oscillator of Continuum Leopard D-20 laser. Two end mirrors enclose several major components: Q-switch dye cell, acousto-optical modulator (AOM), GaAs plate, prism, Nd:YAG rod and flashlamp, and Pockels cell (with photodiode trigger perpendicular to beam path).

The heart of the laser is the Nd:YAG rod – a material with Nd^{3+} dopants in a yttrium aluminum garnet (YAG) used throughout spectroscopic science. Flash lamps pump ~800 nm light, which elicit an electronic excitation whose decay results in the well-known 1064 nm output (Figure 2.6). Lasing occurs through a four level transition scheme where an electron travels among discreet energy levels. Optical excitation with flash lamps to achieve population inversion is the first step. At the maximum energy level, the electron is not stable, which results in rapid decay to a quasi-stable state. The lifetime at the quasi-stable state is long enough for light to pass back and forth through the oscillator many times. Under these conditions, lasing occurs as photon packets trigger the release of additional photons ($E_2 \rightarrow E_1$) during each pass.

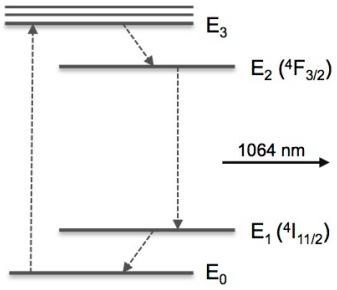

Figure 2.6: Energy level diagram for Nd:YAG electronic transitions. Flash lamps trigger initial excitation ($E_0 \rightarrow E_3$) where many possible states exist. From E_3, the electron quickly decays to a quasi-stable state (E_2). 1064 nm light is generated when ($E_2 \rightarrow E_1$) and this is followed by a transition to the ground state ($E_1 \rightarrow E_0$).

The journey of photons through the oscillator can be characterized by a pulse train (Figure 2.7). As the laser operates a photodiode detects traces of scattered light very quickly and the measurement is displayed using an oscilloscope. If too little laser dye is present in the Q-switch dye cell, the pulse train will resemble a Gaussian distribution (Figure 2.7(C)). However, as the appropriate amount of dye is added and other parts of the oscillator are tuned correctly – including the acousto-optical modulator (AOM), end mirror, threshold level and prism – the pulse train will appear as shown in Figure 2.7(A). In this case, the pulse train is over thirty passes long and maintains a stable region in the middle, where the amplifier seed is generated. The flatness of the middle region indicates that the amount of photons gained from the Nd^{3+}:YAG rod per pass are equal to losses due to absorption into the dye, the GaAs plate and other optical components.

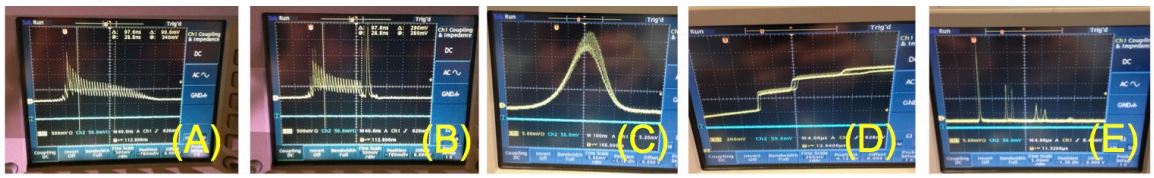

Figure 2.7: Oscilloscope screen shots showing pulse train in oscillator as measured by a photodiode trigger. (A) Full pulse train. (B) Pulse train with Pockels cell engaged (large trailing peak is pulse in amplifier). (C) Gaussian pulse train observed with low dye level. (D) Integrated pulse train with AOM turned OFF. (E) Pulse train (not integrated) with AOM turned OFF.

The AOM is a glass medium with a perpendicular piezoelectric transducer (sound speaker). As light passes through the glass, sound waves constructively and destructively interfere with the light transforming multiple pulse trains into a single pulse train in the oscillator cavity. Figure 2.7 (D) and (E) show the integrated and non-integrated pulse trains if the AOM is OFF. When the AOM is ON, (E) becomes (A). The time for light to make a round trip through the oscillator is 2L / c. The AOM frequency required to create a single pulse train is related to the length of the oscillator (where cavity mode spacing is $\Delta\nu = c / 2L$). The half maximum pulse width (often in picoseconds or femtoseconds) is:

$$\Delta t = \frac{2\pi}{\Delta\nu(2N+1)}$$

Therefore, active mode locking allows ultra-short pulse widths to be achieved and occurs when the AOM operates at $\Delta\nu$.

The Pockels cell is responsible for dumping a seed from the oscillator to the amplifier at the right time. The Pockels cell operates as a fast half-wave plate with voltage control. As potential is applied to a non-linear crystal, the polarization of the outgoing pulse is rotated so a higher

percentage is reflected from the prism (into the amplifier) rather than transmitted. Importantly, Pockels cells can activate/deactivate in a few picoseconds using a photodiode trigger. In the amplifier, the pulse intensity is increased by two orders of magnitude using the same Nd:YAG crystal as the oscillator.

Non-linear crystals generate the tunable infrared (2700-3200 cm^{-1}) and visible beams (532 nm) in a series of steps which modify the monochromatic 1064 nm output from the laser. Sum frequency generation, optical parametric generation and optical parametric amplification (difference frequency generation) steps are included. When two photon combine into one with double the energy, sum frequency generation occurs:

$$\omega_3 = \omega_1 + \omega_2$$

In this laser system two 1064 nm photons combine to make one 532 nm photon. When two photons of equal energy combine (frequency doubling), second harmonic generation – a form of sum frequency generation – occurs:

$$\omega_2 = 2\omega_1$$

In Figure 2.8 (cut out from Figure 2.4) the first frequency doubling crystal (1) is BBO followed by KTP (2). Importantly, the BBO crystal (1) is responsible for partitioning power between the optical parametric generation crystals and the visible beam line. If 1064 nm photons do not combine to make 532 nm, they will pass through the mirror and be completely converted to 532 nm with the thick KTP crystal (2). The 532 nm photons made at (1) feed the optical parametric generation crystals and directly correlate to the power of the tunable infrared.

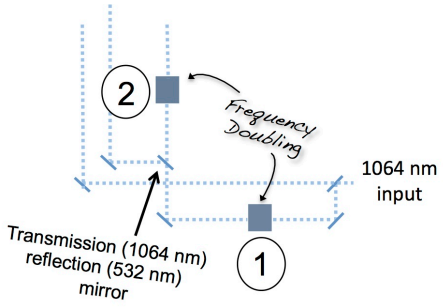

Figure 2.8: Frequency double with non-linear crystals is the first step after the laser. The orientation of (1) can affect the power of the visible and tunable infrared beams used for SFG.

Adjusting the tilt/yaw of (1) allows the final visible (532 nm) and tunable infrared power to be tuned to ~150 μJ for each. (Small changes in orientation strongly affect path length and phase matching conversion.) Therefore, the characteristics of (1) are detrimental to the overall performance of the SFG system (specifications of the BBO crystal appear in the Appendix of this chapter). Phase matching occurs when wavevector (k) mismatch is equal to zero:

$$\Delta k = k_1 + k_2 - k_3 = 0$$

where k_1 and k_2 represent two incoming photon's wavevector and k_3 is the outgoing photons wavevector. In addition, the maximum intensity (I_3) of the outgoing photons (graphed in Figure 2.9) depends on the effective path length (L) of the material:

$$I_3 = I_3^{MAX}\left(\frac{\sin(\Delta kL/2)}{(\Delta kL/2)}\right)^2$$

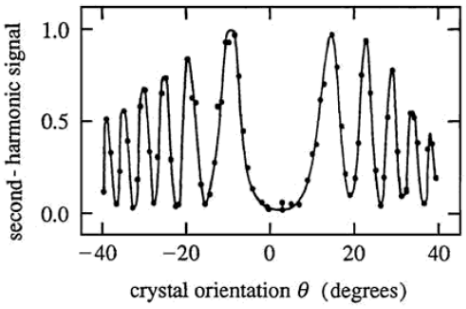

Figure 2.9: As the quartz crystal is rotated, the path length of the beam – a function of θ – changes and the second harmonic conversion varies according to the I_3 expression.[2]

Once 532 nm light is created, the next step is optical parametric generation and difference frequency generation to make the tunable infrared for SFG (Figure 2.10). Optical parametric generation occurs when 532 nm light is passed through two KTP ($KTiOPO_4$) crystals. One 532 nm photon is converted to two lower energy photons called signal and idler:

$$\omega_{idler} + \omega_{signal} = \omega_{532nm}$$

The idler photon is subsequently used to create the tunable infrared while the signal photon is discarded. 532 nm light passes through the KTP crystals twice and during the second pass, the idler intensity is amplified considerably. The angular orientation of the KTP crystals determines the frequency of the signal and idler photons (Figure 2.11). As the angle changes, phase matching conditions change, making the output tunable. Because both KTP crystals are turned with motors to the same complementary angle and alignment is equivalent, identical phase matching conditions of both passes are maintained.

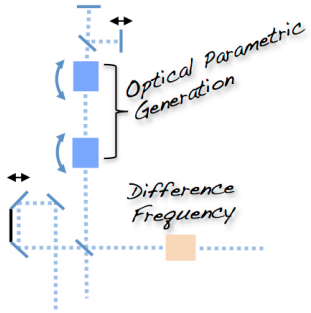

Figure 2.10: Two KTP crystals perform optical parametric generation (OPG) with 532 nm input. The idler beam from the OPG is then combined with 1064 nm for difference frequency generation with a $LiNbO_3$ (LNO) crystal, where the tunable infrared is made for SFG.

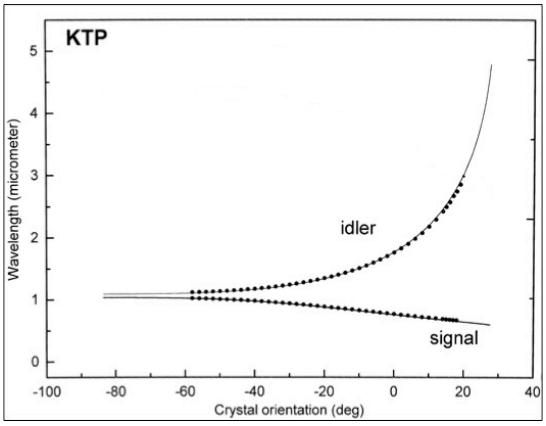

Figure 2.11: Example type II KTP ($KTiOPO_4$) tuning curve from Girardeau-Montaut *et al*.[3] where one 532 nm photon is split into signal and idler photons of different energy.

With the idler beam supplied by the OPA, difference frequency generation occurs with a LNO ($LiNbO_3$) crystal:

$$\omega_{IR} = \omega_{1064\,nm} - \omega_{idler}$$

As the energy of the idler increases, the wavenumber value of the tunable infrared decreases. Using the OPA and OPG together, the tunable infrared (2700-3200 cm^{-1}) is created.

SFG experiments are conducted using Langmuir-Blodgett (LB) films on a fused silica prism (Figure 2.12). There are several advantages to using a prism instead of a simple flat substrate such as a glass slab. With a prism, it is relatively easy to achieve total internal reflection (TIR) without losing light intensity to reflection at the first surface. Figure 2.12 illustrates that both the visible and infrared beams go into the prism at angles nearly perpendicular to the silica face, resulting in nearly complete transmission based on Fresnel equations. Figure 2.13 shows the SFG spectra of polystyrene collected on a glass slab and on a prism. Using TIR geometry, which produces an evanescent wave at the surface of the prism, the SFG signal from the nanoparticle film is significantly enhanced (Figure 2.14).

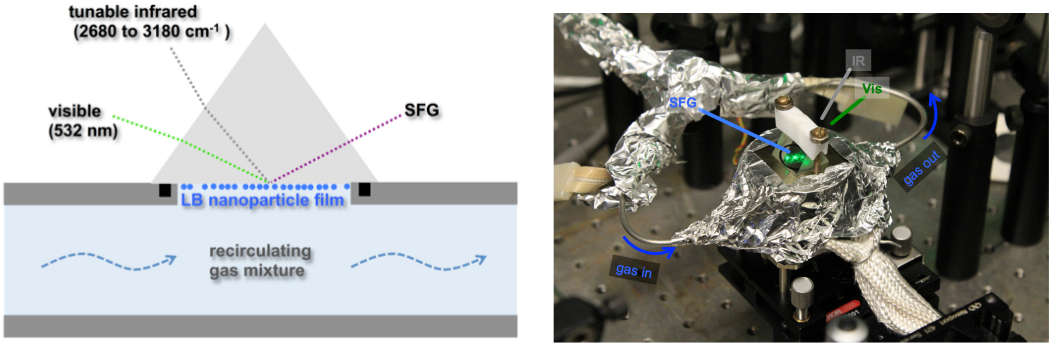

Figure 2.12: Setup for studying nanoparticle catalysts with SFG under ambient conditions (schematic on left and lab reactor on right). SFG scans are collected as 2-D nanoparticle films are exposed to various reaction conditions. Both visible and tunable infrared beams operate with total internal reflection (TIR) geometry. Temperature is controlled with heating tape and monitored with a K-type thermocouple touching the center of the prism. The reactor forms a seal to the prism with a Kalrez o-ring.

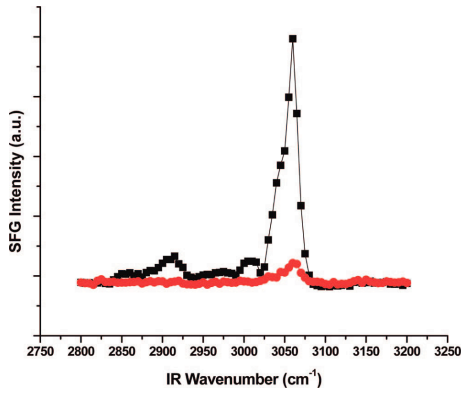

Figure 2.13: SFG spectra of equivalent polystyrene film on a prism (black) and a flat slab (red). The prism utilizes TIR geometry, which amplifies SFG intensity.[4]

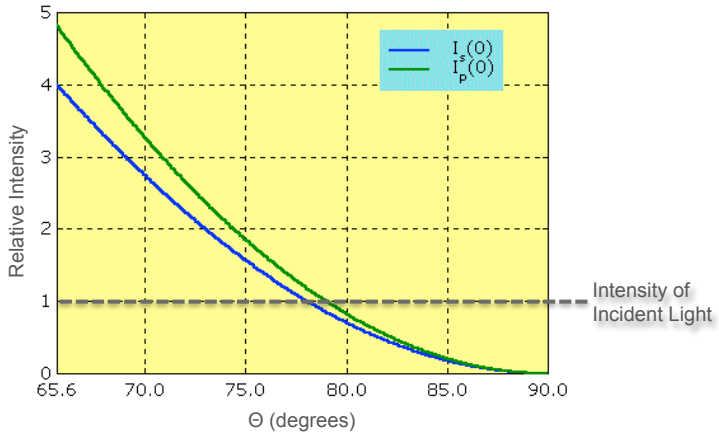

Figure 2.14: Example evanescent wave intensity (I_s, I_p) where $\theta > 65.6°$ (θ_c) -- total internal reflection conditions for s and p polarized light. The maximum intensity of the evanescent wave near the critical angle (θ_c) is 4-5 times the maximum of incident light.[5]

Langmuir-Blodgett (LB) monolayer film deposition (Figure 2.15) was used for all SFG experiments on nanoparticles. First, Pt-PVP nanoparticles (1-10 nm) were dissolved in 50/50 EtOH/$CHCl_3$. This solution is added dropwise to the surface of water and left for 30 min for the solvent to evaporate. Then the barrier is slowly compressed at 10 mm/min until the surface

pressure exceeds 25 mN/m. At this point, the film is near maximum compression and the prism is slowly lifted at 3 mm/min through the surface from the subphase. The resulting monolayer film on the prism was visible to the naked eye and suitably dense in Pt for SFG reaction studies.

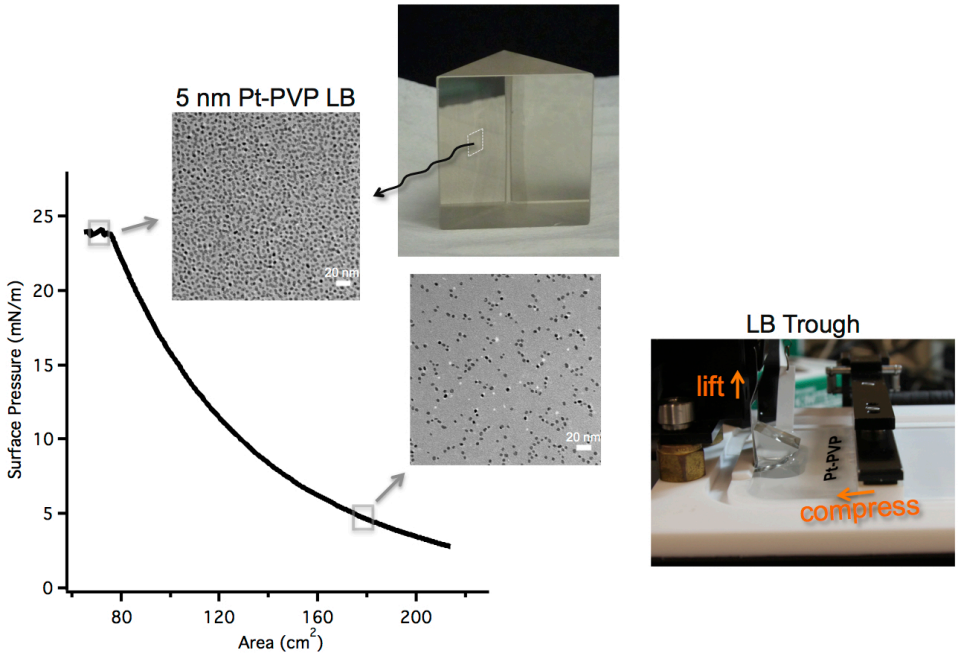

Figure 2.15: Langmuir-Blodgett (LB) film deposition for SFG experiments. Pt-PVP nanoparticles are dispersed on the surface of water and compressed near maximum surface pressure resulting in a dense monolayer. The SFG prism is lifted through the surface after the film is compressed.

Transmission electron microscopy (TEM) was utilized in several chapters of this thesis to image nanoparticle catalysts (Figure 2.16). High energy (200 kV) electrons from an electron gun are focused onto the thin sample, visualized using a fluorescent screen and ultimately captured with a CCD camera. A TEM image is a two dimensional representation of the transmission probability, where the contrast varies by the material mass and diffraction patterns. Within the microscope, several electromagnetic lenses are used to focus the electrons. The condenser lens

and aperture controls the spot size of the electron beam. The objective and projector lenses mainly control focus and magnification, respectively.

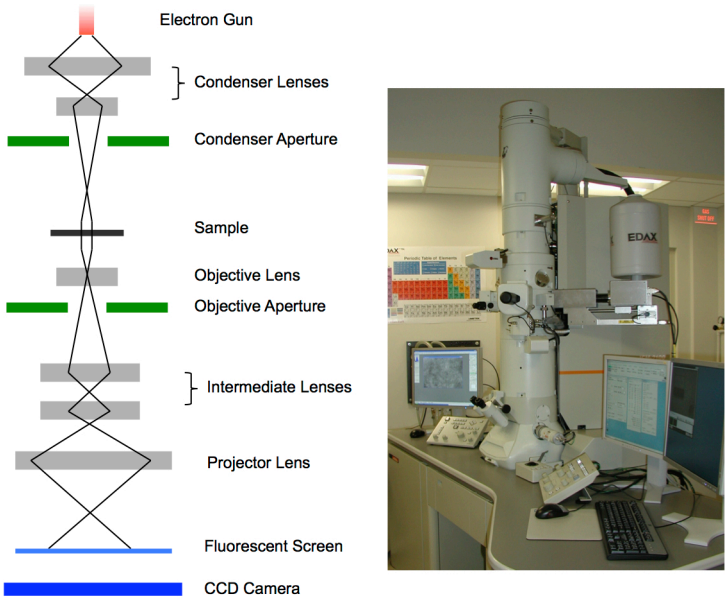

Figure 2.16: Schematic of a transmission electron microscope (TEM) (left) and photograph of a JOEL 2100 TEM with an energy-dispersive X-ray spectroscopy (EDS) attachment (right).

Besides transmission, several other processes simultaneously occur in a TEM microscope. When electrons of the beam inelastically collide with the sample, secondary electrons are produced along with electron-hole pairs, X-ray photons and Auger electrons. The formation of X-rays is particularly important because their wavelengths can reveal electronic transitions of the sample. Energy-dispersive X-ray spectroscopy (EDS) is often used within TEM microscopes for elemental analysis (Figure 2.17). As electrons are ejected from core orbitals, holes are created and subsequently filled by electrons from higher orbitals. As the energy of the electron changes during the orbital transition, an X-ray photon is emitted. The energy of the X-ray photon equals the energy difference between the orbitals. Because each atom has unique orbital spacing, the wavelength of the X-ray can be used to determine atomic identity. The physics of EDS is

comparable to XPS except EDS is an electron in, photon out process while XPS is photon in, electron out. Because X-rays penetrate deeply into matter, information from EDS is not as surface sensitive as XPS.

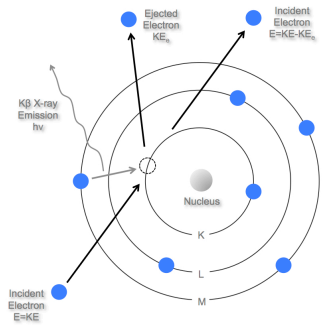

Figure 2.17: Fundamental process required for energy dispersive X-ray spectroscopy (EDS). High energy incident electrons cause electrons to be ejected which then leads to X-ray emission. From the wavelength of the outgoing X-rays, atomic identity can be determined.

X-ray photoelectron spectroscopy (XPS) can reveal the oxidation state and surface composition of metal catalysts. As illustrated in Figure 2.18, X-rays eject electrons which are subsequently collected and separated by their kinetic energy. The difference in kinetic energy of electrons suggests the atom from which they originated. The binding energy of an electron varies significantly based on the atom and orbital. For example, the binding energy core 1s electrons of Ga (10,367 eV) is much higher than the binding energy of valence 3d electrons (20 eV). The binding energy of core 1s electrons of Si (1,839 eV) is considerably weaker than Ga because of the effective nuclear charge of Si (14 protons) compared to Ga (31 protons). In addition, as atoms adopt different oxidation states, the binding energy shifts. For the 4f electrons of Pt, the binding energy increases 3 eV – from 71 to 74 eV – when Pt^0 is oxidized to Pt^{4+}. Because electrons reveal the information in XPS, the technique is inherently surface sensitive. The mean

free path of electrons of most materials is near 1 nm (depending on the universal curve of elements), so the effective probing depth of XPS is typically near 1 nm. If electrons travel beyond this length, they undergo one or more inelastic collisions, lose energy and become secondary electrons. The background intensity in XPS spectra is due to secondary electrons which have a random energy distribution and do not provide much chemical information.

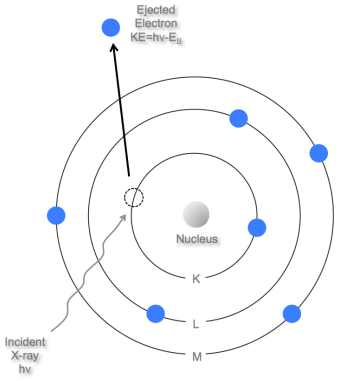

Figure 2.18: Fundamental process for X-ray photoelectron spectroscopy (XPS). X-rays eject electrons from the core orbitals of atoms. Composition can be determined from the kinetic energy of the outgoing electrons.

Because electrons cannot travel far in air without collisions, XPS is most commonly used as an ultra-high vacuum characterization technique. Today, XPS instruments are modified to operate under ambient conditions to study materials in normal reaction environments. Ambient pressure XPS (AP-XPS) systems (Figure 2.19) include sophisticated differential pumping stages and electron-focusing lenses which allow experiments up to 5 Torr in pressure. Other features, such as the X-ray source and hemispherical electron energy analyzer, are similar to conventional XPS. AP-XPS experiments discussed in this thesis were performed at the Advanced Light Source at Lawrence Berkeley National Laboratory.

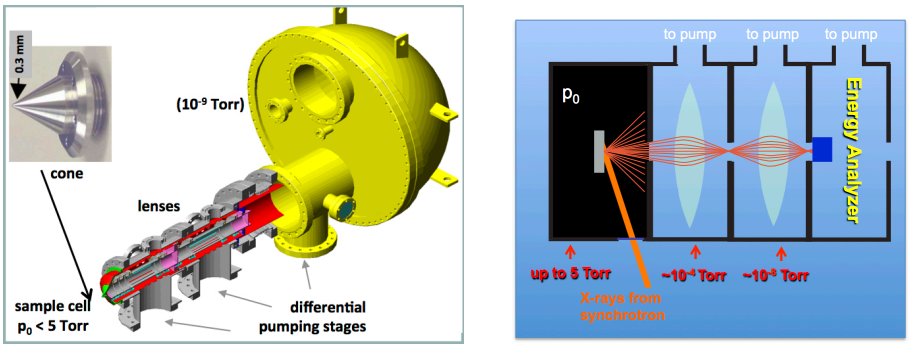

Figure 2.19: Ambient pressure X-ray photoelectron spectroscopy (AP-XPS) apparatus. A cone is used to syphon electrons from the sample into focused differential pumping stages before being separated by kinetic energy.

References

(1) Lambert, A.; Davies, P. *Applied Spectroscopy* **2005**.
(2) Boyd, R. W. *Nonlinear Optics*, 2nd ed.; Elsevier: Amsterdam, The Netherlands, 2003.
(3) Carrion, L.; Girardeau-Montaut, J. P. *Optics communications* **1998**, *152*, 347.
(4) York, R. L.; Li, Y. M.; Holinga, G. J.; Somorjai, G. A. *Journal of Physical Chemistry A* **2009**, *113*, 2768.
(5) Image modified from <http://www2.bioch.ox.ac.uk/oubsu/ebjknight/tirtheory.html>

Chapter 3: Sum Frequency Generation Vibrational Spectroscopy of Colloidal Platinum Nanoparticle Catalysts: Disordering versus Removal of Organic Capping

3.1 Introduction

Sum frequency generation (SFG)[1, 2] vibrational spectroscopy is a second-order optical process that measures the vibrational spectrum of molecules on a surface or an interface. This technique is a powerful tool for studying heterogeneous catalysis because it enables the observation of surface intermediates during catalytic reactions. SFG vibrational spectroscopy has been used to study reactions on both single-crystal catalysts[3-5] and 2D films of nanoparticle catalysts.[6, 7] Recent work on nanoparticle catalysts has shown that size and shape control on the nanometer scale is critical for reaction selectivity.[8-12] This is a major advance for heterogeneous catalysis and motivates the present effort to observe reaction intermediates on size- and shape-controlled nanoparticles under reaction conditions.

A major challenge in the detection of reaction intermediates is the background of molecular stretches originating from the organic capping layer of colloidal nanoparticles. Nanoparticles require a layer of organic ligands to stabilize both size and shape. However, the organic capping layer has two major effects on catalytic reaction studies. First, it blocks active sites on the nanoparticles reducing catalytic activity. Second, it produces a strong signal in the SFG spectrum, making the observation of reaction intermediates on the nanoparticles difficult or impossible. Common capping agents, including poly(vinylpyrrolidone) (PVP),[13] cetyltrimethylammonium bromide (CTAB),[14] tetradecyltrimethylammonium bromide (TTAB),[15] hexadecylamine (HDA),[16] and oleylamine[17] produce a signal in the aliphatic range, preventing the identification of C–H vibrations of reactive catalytic intermediates.

UV light has been previously used to remove the organic capping agent from nanoparticles.[7, 18, 19] This study compares UV cleaning of nanoparticles (often called "UVO" or "UV-ozone") and a simpler, yet more effective method, termed solvent cleaning, which removes excess capping (PVP) from the nanoparticles. It is shown that both UV and solvent cleaning of Pt nanoparticles enable the observation of reaction intermediates by SFG spectroscopy. However, solvent cleaning leaves more PVP intact and relies on disordering under hydrogen to reduce its SFG signal, whereas UV cleaning reduces the signal from PVP by nearly complete removal. It is also shown that solvent cleaning produces nanoparticles that are stable under reaction conditions, whereas UV cleaning results in nanoparticle aggregation during reaction. Therefore, solvent cleaning makes it possible to study size- and shape-dependent nanoparticle selectivity using SFG vibrational spectroscopy.

Cyclohexene (C_6H_{10}) hydrogenation is a good reaction for SFG analysis because it produces intermediates with unique and well-documented[5, 20-25] vibrational signatures. Three different reaction intermediates of cyclohexene hydrogenation exist on Pt that are easily identifiable in the SFG spectrum: 1,4-cyclohexadiene (1,4-CHD), 1,3-cyclohexadiene (1,3-CHD), and π-allyl. The spectrum of 1,4-CHD has a single peak at 2765 cm^{-1}, corresponding to a strongly red-shifted CH_2 asymmetric stretch. 1,3-CHD has three CH_2 stretches at 2830, 2875, and 2900 cm^{-1}, whereas the π-allyl has a strong CH_2 asymmetric stretch at 2920 cm^{-1} and a weak symmetric CH_2 stretch at 2840 cm^{-1}. Using cyclohexene hydrogenation on Pt as a model reaction, the catalytic activity and vibrational spectra of solvent-cleaned Pt nanoparticles were examined under reaction conditions and compared with those of UV-cleaned Pt nanoparticles.

3.2 Experimental Methods

3.2.1 Nanoparticle Synthesis. Pt particles of 4.2 nm average size were synthesized using 100 mg chloroplatinic acid hexahydrate ($H_2Pt(IV)Cl_6 \cdot 6H_2O$, 37.5% metal basis, Sigma-Aldrich), 440 mg PVP (29 K, Sigma-Aldrich), and 20 mL of ethylene glycol (ReagentPlus, Sigma-Aldrich). The mixture was combined in a 25 mL round-bottomed flask, pumped to remove air, and flushed with Ar. The flask was then placed in an oil bath at 165 °C for 1 h under Ar flow. Pt nanoparticles of 3.0 nm average size[26] were synthesized using 40 mg ammonium tetrachloroplatinate(II) ($(NH_4)_2Pt(II)Cl_4$), 220 mg PVP (29 K, Sigma-Aldrich), and 20 mL of ethylene glycol (ReagentPlus, Sigma-Aldrich). The mixture was combined in a 25 mL round-bottomed flask, pumped to remove air, and flushed with Ar. The flask was then placed in an oil bath at 165 °C for 30 min under Ar flow. Pt nanoparticles of 1.7 nm average size[27] were synthesized by combining 250 mg chloroplatinic acid hexahydrate ($H_2Pt(IV)Cl_6 \cdot 6H_2O$, 37.5% metal basis, Sigma-Aldrich), 25 mL of ethylene glycol (ReagentPlus, Sigma-Aldrich), and 0.00625 g NaOH under Ar at 433 K for 1 h. After synthesis, the nanoparticles were precipitated with 1.0 M HCl and then combined with PVP. Nanoparticles of different sizes were separated from the ethylene glycol synthesis mixture by precipitation with acetone and centrifugation at 4000 rpm for 5 min. Then, the nanoparticles were dissolved by sonication in 20 mL of ethanol, mixed with 25 mL of hexane, and centrifuged again for precipitation. This process was repeated three times to remove ethylene glycol and excess chloroplatinic acid from the synthesis. Hereafter, these nanoparticles will be referred to as fully-capped nanoparticles.

3.2.2 Solvent Cleaning. For the 4.2 and 3.0 nm nanoparticles, solvent cleaning consisted of five additional cycles of ethanol washing, followed by precipitation in hexane for a total of eight ethanol washes after synthesis. Following these cycles of ethanol washing, the nanoparticles

were further washed two times, once in chloroform and once in isopropyl alcohol. Because the 1.7 nm nanoparticles retained less PVP, they did not require as many washing cycles. Therefore, these nanoparticles were washed only one additional time in ethanol for a total of four ethanol washes after synthesis. If washed more times, 1.7 nm nanoparticles aggregate in solution.

3.2.3 Langmuir-Blodgett Film Deposition. Nanoparticles were first dissolved in a 50/50 ethanol/chloroform mixture and then deposited onto a water surface.[28] For Langmuir–Blodgett (LB) deposition, a suspension of nanoparticles in the ethanol/chloroform mixture was dispersed onto a water surface. Sufficient time was allowed for the organic solvent to evaporate, leaving a 2D dispersion of nanoparticles on water. The film was then compressed, and the increase in surface pressure was monitored. When the desired surface pressure was reached, the SFG prism was pulled through the water at a rate of 3 mm/min, and a monolayer film of nanoparticles was deposited onto the prism surface. For SFG experiments, a surface pressure of 20 mN/m was used for LB films. Film deposition on transmission electron microscopy (TEM) grids was accomplished by dropping the grid on the compressed LB film for 10 s and then retrieving the grid with tweezers. For TEM experiments, a surface pressure of 8 mN/m was used to obtain nanoparticle films of low density. This provided better visibility of nanoparticle aggregation that occurred for some samples under reaction conditions. The Nima 611 LB trough with filter paper as the surface tension probe was used in all film depositions.

3.2.4 UV Cleaning. Two low-pressure mercury lamps (Lights Sources, model number GPH357T5VH/4P) were used for UV treatment inside a clean aluminum box. Samples were placed 5 mm below one lamp and exposed to 254 and 185 nm irradiation for a specified time.

3.2.5 Sum Frequency Generation Vibrational Spectroscopy. A mode-locked Nd:YAG dye laser (Continuum D-20) with 1064 nm fundamental output, 20 Hz repetition rate, and 20 ps pulse

width was used in all of the experiments described herein. A frequency-doubling crystal was used to generate a visible (532 nm) beam from the fundamental beam. An optical parametric generator/amplifier produced tunable infrared in the range 2680–3180 cm^{-1}, corresponding to the stretching modes of aliphatic and aromatic groups. Visible and infrared beams of 130 μJ power were spatially and temporally overlapped at the base of the SFG prism at angles of 63 and 48°, respectively, from the surface normal to achieve total internal reflection (Figure 3.1). All of the experiments were performed in ppp polarization combination. Polished fused silica equilateral (60°) prisms (ISP Optics) were used in all experiments. A photomultiplier tube with a gated boxcar integrator detected SFG photons. Each LB nanoparticle film was probed with SFG under 1 atm of total pressure.

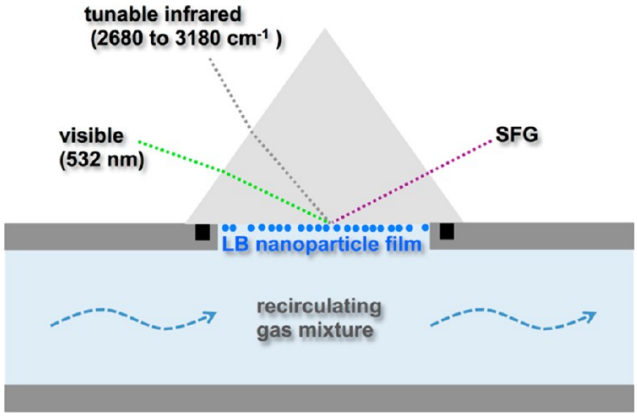

Figure 3.1: Schematic of SFG experiment with LB nanoparticle films deposited on a silica prism. Gas mixtures (Ar, H_2/Ar, and C_6H_{10}/H_2/Ar) are flowed over the sample while SFG spectra are recorded.

The SFG signal intensity I^{SFG} can be understood in terms of the second-order non-linear susceptibility constant $\chi^{(2)}$:

$$I_{\mathrm{SFG}} \propto |\chi_{\mathrm{NR}}^{(2)} + \chi_{\mathrm{R}}^{(2)}|^2 = \left|\chi_{\mathrm{NR}}^{(2)} + \frac{A_q}{\omega_{\mathrm{IR}} - \omega_q + i\Gamma}\right|^2$$

with

$$A_{q,ijk} = N_{\mathrm{S}} \sum_{lmn} a_{q,lmn} \langle (\hat{i}\cdot\hat{l})(\hat{j}\cdot\hat{m})(\hat{k}\cdot\hat{n}) \rangle$$

where $\chi_{NR}^{(2)}$, $\chi_{R}^{(2)}$, A_q , ω_{IR}, ω_q and Γ are non-resonant[30] contributions, resonant contributions, amplitude, infrared frequency, qth mode frequency, and damping factor, respectively. Oscillator strength A_q reflects the number density N_S, Raman/infrared response a_q, and average oscillator orientation <···> (encompassing both lab coordinates *ijk* and molecular coordinates *lmn*). Unlike the varied forms of linear vibrational spectroscopy, SFG requires a net orientation along the z axis (perpendicular to the surface), which gives surface selectivity. This indicates that even concentrated vibrational modes will ultimately cancel if present only in random disordered directions.

3.6 Transmission Electron Microscopy. TEM images of LB films were obtained with a JEOL 2100 microscope operated at 200 kV. Silicone (SiO) films on copper grids (Electron Microscopy Sciences) were used as substrates for all TEM images presented here.

3.7 Kinetic Measurements. Turnover rates were measured with a Hewlett-Packard 5890 Series II gas chromatograph connected to a circulating batch reactor. The Restek Haysep Q 80/100 column was used to measure ethylene hydrogenation rate, and the Alltech AT-1000 column was used to measure cyclohexene hydrogenation rate.

3.3 Results and Discussion

3.3.1 Effect of PVP Removal on Detection of Reaction Intermediates on Pt Nanoparticles

The capping agent presents a challenge for SFG studies of colloidal nanoparticle catalysts because its signal often overlaps with that of the reactive intermediate of interest and also blocks catalytically active surface sites. In the presence of H_2, PVP becomes disordered on fully-capped nanoparticles, as shown by the significant decrease in background signal intensity (Figure 3.2A). However, even in the absence of a background signal from the PVP, a signal from the reaction intermediate (1,4-CHD) cannot be easily observed during cyclohexene hydrogenation (Figure 3.2B) because of site blocking by disordered PVP.

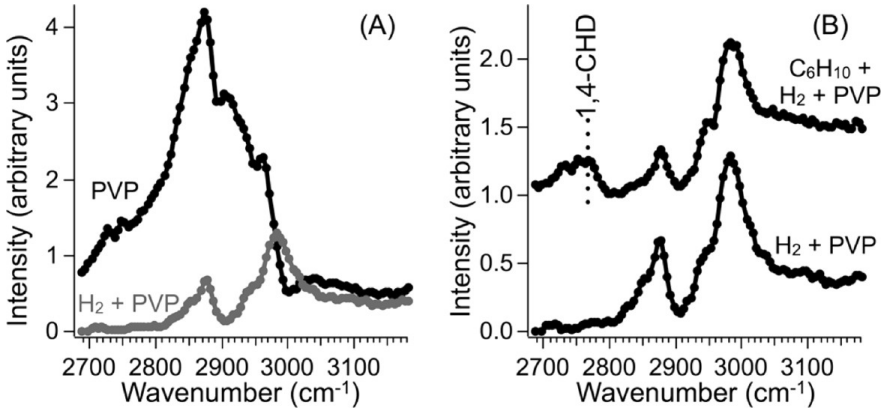

Figure 3.2: SFG spectra of fully-capped 4.2 nm Pt-PVP nanoparticles obtained at 298 K in different atmospheres: (A) 760 Torr Ar (top) and 200 Torr H_2, 560 Torr Ar (bottom) and (B) 10 Torr C_6H_{10}, 200 Torr H_2, 550 Torr Ar (top) and 200 Torr H_2, 560 Torr Ar (bottom). Spectra shown in (B) are offset for clarity. Unlabeled features are attributed to PVP.

In the case of solvent-cleaned nanoparticles, a strong signal from PVP is still observed in the SFG spectrum (Figure 3.3A). This is because solvent cleaning does not remove all PVP; if it did, then the nanoparticles would aggregate in solution. Similar to fully-capped nanoparticles (Figure

3.2A), the signal from PVP diminishes in H_2 due to the disordering effect (Figure 3.3A). To see the degree of disordering on 4.2 nm Pt-PVP with different H_2 pressures, see Figure S.3.1. The major difference between fully-capped and solvent-cleaned nanoparticles can be observed by comparing the spectra obtained under reaction conditions (Figures 3.2B and 3.3B). Under cyclohexene hydrogenation conditions, the 1,4-CHD intermediate is clearly visible in the SFG spectrum of the solvent-cleaned Pt nanoparticles (Figure 3.3B), indicating significant adsorption on the Pt nanoparticle surface. This finding indicates that although the solvent-cleaned nanoparticles are lightly capped with PVP, there are sufficient Pt sites available for catalysis and for observing reaction intermediates with SFG.

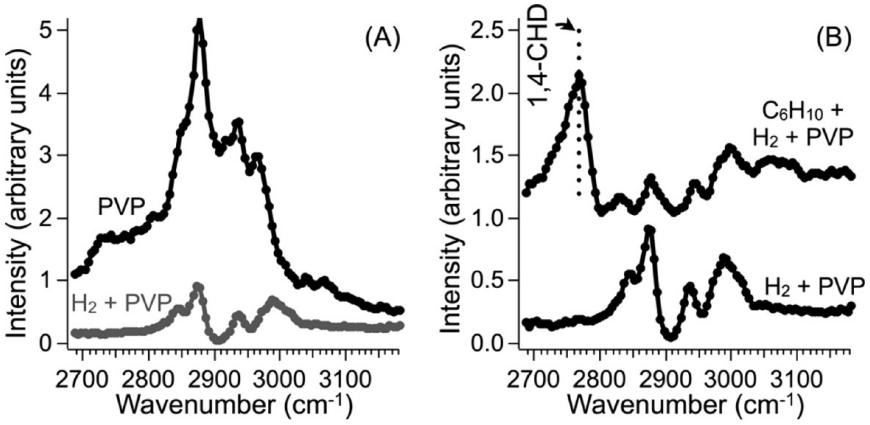

Figure 3.3: SFG spectra of solvent-cleaned 4.2 nm Pt-PVP nanoparticles obtained at 298 K in different atmospheres: (A) 760 Torr Ar (top) and 200 Torr H_2, 560 Torr Ar (bottom) and (B) 10 Torr C_6H_{10}, 200 Torr H_2, 550 Torr Ar (top) and 200 Torr H_2, 560 Torr Ar (bottom). Spectra shown in (B) are offset for clarity. Unlabeled features are attributed to PVP.

Because the peak of 1,4-CHD occurs at a unique wavenumber position compared to other aliphatic vibrations, it is certain that it arises from a chemisorbed reaction intermediate on the surface of the Pt nanoparticle and not from PVP. Interestingly, when cyclohexene is introduced

with H_2, the remaining PVP peaks are further suppressed from the level observed with only H_2. This suggests that 1,4-CHD displaces PVP from the Pt surface into a disordered geometry. SFG spectra were also collected during cyclohexene hydrogenation on 1.7 and 3.0 nm Pt nanoparticles. The spectra of 1.7 nm and 3.0 nm Pt-PVP (1.7 nm shown in Figure S.3.2A) also indicate a strong peak corresponding to the 1,4-CHD intermediate. The 1.7 nm Pt nanoparticles retain less PVP than larger nanoparticles and do not require as much solvent cleaning for observing surface intermediates (see Section 2.2). In addition, reaction intermediates can be observed in the same range as PVP peaks. S.3.2B shows the *di-σ* intermediate on 3.0 nm Pt-PVP during cis-2-butene hydrogenation.

Although the role of solvent cleaning to increase the available Pt surface area through PVP removal is intuitive, the role of H_2 to decrease the background signal of PVP is less obvious and needs further interpretation. H_2 dramatically reduces the signal from PVP on both fully-capped and solvent-cleaned nanoparticles (Figures 3.2A and 3.3A). Under an inert atmosphere of Ar gas, the full signal of PVP capping is strong for both types of nanoparticles. However, adding H_2 reduces the signal of PVP to relatively weak peaks located at 2850 (symmetric CH_2, chain), 2870 (symmetric CH_2, chain), 2930 (asymmetric CH_2, chain), and 2980 cm^{-1} (asymmetric CH_2, ring).[31]

SFG selection rules indicate that decreasing concentration or increasing disorder reduce signal. Although the effect of concentration on the spectral intensity is expected, it is important to recognize the effect of molecular ordering on the spectral intensity. Because SFG vibrational spectroscopy is a coherent process, it is not only sensitive to individual molecular susceptibilities

but also to the net susceptibility of the ensemble of molecular oscillators. Consequently, if molecules on a surface are highly disordered, then the net ensemble will not produce a strong SFG signal, even if the concentration is high.

The following two examples emphasize this concept. In a recent study,[32] the ordering of mixed self-assembled monolayers of fluorinated alkyl phosphonic acid and C_{60} functionalized octadecyl phosphonic acid was tuned by varying the amounts of each component. For certain mixtures, the SFG intensity from C_{60} molecules decreased even as its surface density increased. This effect is attributed to disordering of the self-assembled monolayer. In another case,[5] the observed peaks from the π-allyl intermediate on Pt(111) increased in intensity by eight-fold when the pressure was changed from ambient to ultrahigh vacuum. Because the surface concentration did not increase dramatically in vacuum relative to ambient pressure, the increased ordering strongly contributed to the signal enhancement. Therefore, it may be concluded that the addition of H_2 disorders PVP on Pt, as indicated by the decrease in SFG signal intensity by 90%. This spectral change is reversible – when the cell is evacuated to vacuum, the full signal of PVP reappears. Disordering likely arises because of a weakened interaction between PVP and Pt. Several previous studies[11, 33, 34] report lower adsorption energies of organic molecules on Pt in the presence of H_2. When no H_2 is present and cyclohexene is introduced, 1,4-CHD does not form on Pt-PVP (Figure S.3.2). On Pt(111), 1,4-CHD – a dehydrogenated reaction intermediate – occurs in the presence or absence of H_2.[5] The absence of 1,4-CHD with no H_2 further indicates that PVP binds strongly with Pt and can completely block strongly adsorbing species (binding energy of 1,4-CHD = 1.5 eV).

UV light of 254 and 185 nm wavelength is known to photodecompose organic materials, including PVP, through photolysis and ozonolysis mechanisms.[35] Accordingly, UV cleaning has been proposed[18] as a viable method for removing PVP from Pt nanoparticles. However, the effects of UV cleaning on the catalytic behavior of Pt nanoparticles are not fully understood. Figure 3.4 shows SFG spectra of PVP-capped Pt nanoparticles after 180 min of UV exposure. The spectrum of the Pt nanoparticles in Ar (Figure 3.4A) shows a significant signal reduction in the aliphatic range compared to fully-capped and solvent-cleaned nanoparticles under the same conditions. This is attributed to the photodecomposition of PVP by UV light. Supporting evidence of PVP removal by UV cleaning was obtained from XPS analysis. It was found that the C content relative to Pt decreases by at least 90% after 10 min of UV cleaning. However, when the UV-cleaned nanoparticles are exposed to H_2, the signal in the aliphatic range increases significantly (Figure 3.4A), suggesting that although UV cleaning removes the majority of PVP, a C shell remains ("residual PVP") that subsequently reacts with H_2. This observation highlights the difficulty of preparing atomically clean Pt nanoparticles by UV cleaning. Under Ar, a low background is achieved after UV cleaning. However, once H_2 is added, the background of disordered PVP is considerably lower than the background of UV-cleaned Pt-PVP. Further studies are in progress to probe the effect of the C shell on Pt catalysis. However, the shell does not prevent adsorption of cyclohexene – 1,4-CHD, 1,3-CHD, and π-allyl intermediates are readily observed on the UV-cleaned nanoparticles under reaction conditions (Figure 3.4B).

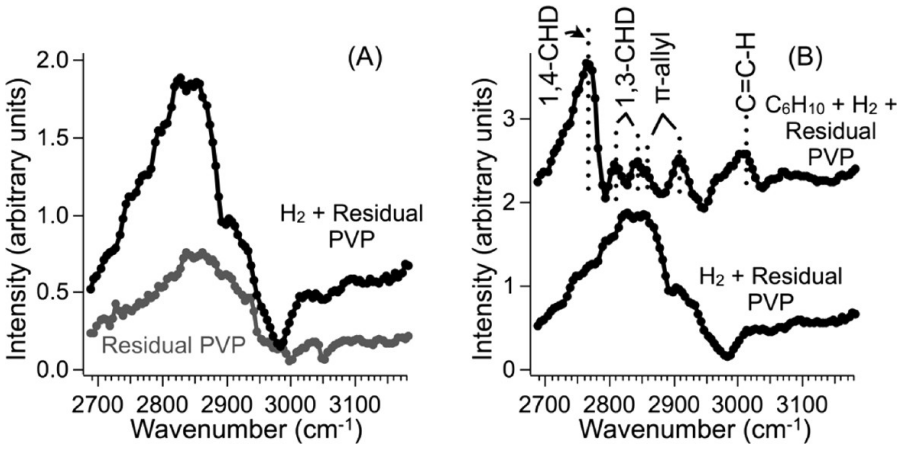

Figure 3.4: SFG spectra of UV-cleaned (180 min) 4.2 nm Pt-PVP nanoparticles obtained at 298 K in different atmospheres: (A) 760 Torr Ar (bottom) and 200 Torr H_2, 560 Torr Ar (top) and (B) 10 Torr C_6H_{10}, 200 Torr H_2, 550 Torr Ar (top) and 200 Torr H_2, 560 Torr Ar (bottom). Spectra shown in (B) are offset for clarity. Unlabeled features are attributed to PVP.

Figure 3.5A shows SFG spectra of 4.2 nm Pt nanoparticles during cyclohexene hydrogenation at 298 K versus UV cleaning time. The removal of PVP is confirmed by the change in C/Pt atomic ratio (obtained by XPS) versus UV cleaning time shown in Figure 3.5B. As expected, the signal from cyclohexene hydrogenation intermediates steadily increases with UV treatment, indicating increased coverage by reactants. This is most obvious for the 1,4-CHD intermediate (2765 cm^{-1}). Further changes in the SFG spectrum occurred with increasing UV cleaning time. UV treatment up to 3 min indicated the formation of only 1,4-CHD, which is consistent with the spectrum of solvent-cleaned nanoparticles (Figure 3.3B). However, longer UV treatment (10 min) produced an intense new peak at 2900 cm^{-1} with a weak counterpart at 2850 cm^{-1}, both assigned to π-allyl. For UV cleaning times ranging from 30 to 180 min, the π-allyl signal decreases, and new peaks appear (2810 and 2845 cm^{-1}), indicating 1,3-CHD. To observe each of these three intermediates on the Pt(111) single crystal with a comparable cyclohexene/H_2 ratio, the temperature must be

increased from 303 to 483 K.[24] In this case, all three intermediates are observed at 298 K on 4.2 nm Pt by removing PVP. For the entire data set including Ar, H_2/Ar and cyclohexene/H_2/Ar for all UV cleaning times, see Figures S.3.3A and S.3.3B.

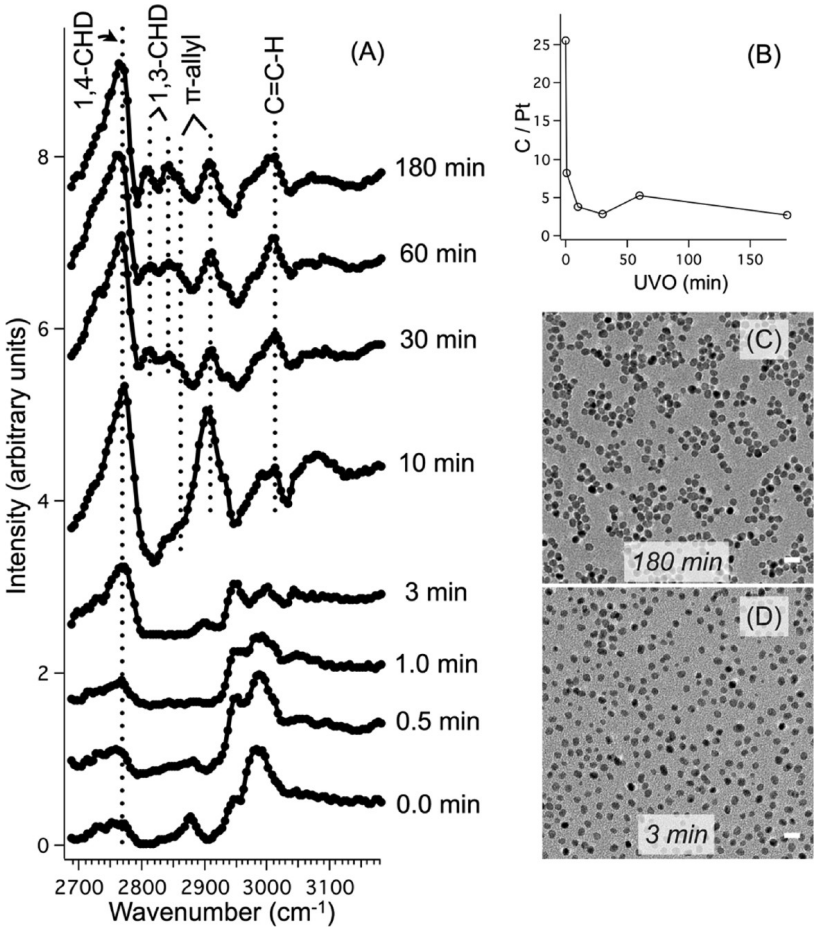

Figure 3.5: (A) SFG spectra of 4.2 nm Pt-PVP nanoparticles obtained at 298 K after UV cleaning (0 to 180 min) under cyclohexene hydrogenation reaction conditions (10 Torr C_6H_{10}, 200 Torr H_2, 550 Torr Ar). The observed intermediates change from exclusively 1,4-CHD (0–3 min) to 1,4-CHD, 1,3-CHD, and π-allyl (30–180 min). (B) XPS results showing the C/Pt ratio as a function of UV exposure time. (C,D) TEM images of UV-cleaned 4.2 nm Pt nanoparticles showing clustering after long treatment (180 min) but no aggregation (scale bar = 10 nm).

The morphological stability of 4.2 nm nanoparticles during UV cleaning at 298 K is demonstrated by TEM images shown in Figure 3.5. Although long UV treatment (180 min) causes nanoparticle clustering (Figure 3.5C), aggregation does not occur – the nanoparticle size and shape is similar to that observed after 3 min of UV cleaning (Figure 3.5D). Consequently, changes in observed intermediates cannot be attributed to nanoparticle size or shape effects. Interestingly, the 1,3-CHD intermediate is much more active for cyclohexene hydrogenation on Pt(111) than the 1,4-CHD intermediate.[24] Therefore, it may be inferred that 180 min of UV cleaning produces nanoparticles that are more catalytically active than the fully-capped nanoparticles because the 1,3-CHD intermediate is observed only after extensive UV cleaning. Kinetic experiments of the present study show that the UV-cleaned catalyst is approximately three times more active for cyclohexene hydrogenation than the fully-capped catalyst, even after correcting for the number of Pt active sites (counted with ethylene hydrogenation). These spectral changes correlate with reaction kinetics and suggest that besides simply blocking equivalent Pt sites, the capping agent may actively promote or inhibit the formation of certain reaction intermediates. Considering the capping agent as an active, dynamic support for nanoparticle catalysis is an intriguing concept that will be investigated in future studies.

3.3.2 Effect of Solvent Cleaning on Size Monodispersity of Pt Nanoparticles During Reaction

The stability of Pt nanoparticles under reaction conditions after solvent cleaning or UV cleaning can be assessed in the light of TEM results presented in this section. Figure 3.6 shows TEM images of fully-capped Pt nanoparticles of three sizes (4.2, 3.0, and 1.7 nm) as LB films before and after two treatments (60 min of UV cleaning, followed by 60 min under hydrogenation

reaction conditions). Although 60 min of UV cleaning caused 4.2 and 3.0 nm nanoparticles to cluster closely together, these nanoparticles maintained a monodisperse size distribution. However, exposure to H_2 at 373 K resulted in melting and loss of size monodispersity. For 3.0 nm nanoparticles, various film compressions were tested (Figure S.3.4). Although lower LB compressions lessen aggregation, the problem cannot be eliminated. (It should be noted that the compression in Figure 3.6 is considerably below what is used for SFG experiment). Compared to larger nanoparticles, 1.7 nm Pt are even less stable and melted after UV cleaning, even before exposure to elevated temperature. Although the images shown in Figure 3.6 were obtained with silicone TEM grids, the same phenomena were observed with other supports, including SiO_2 and TiO_2 (see Figure S.3.5).

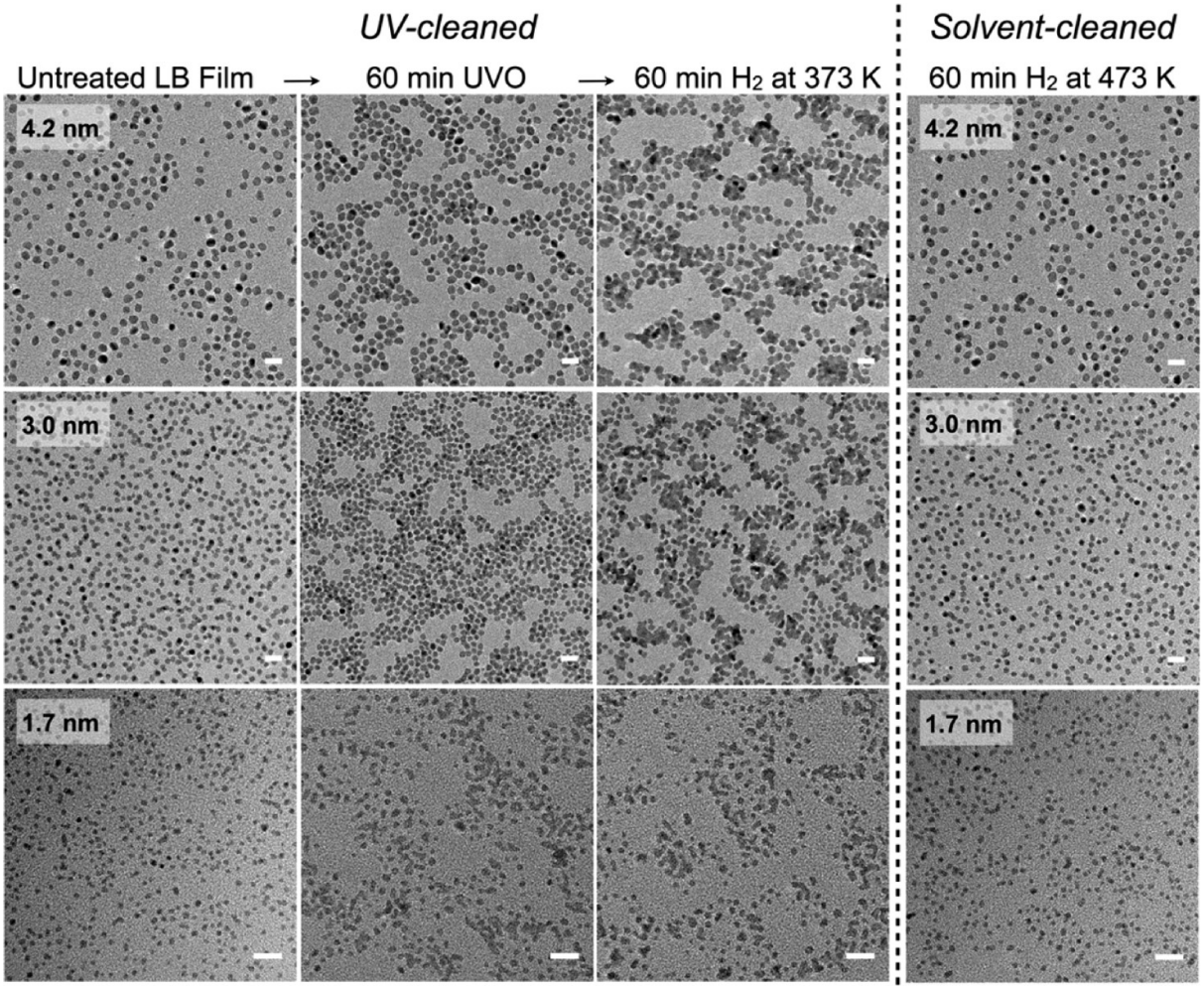

Figure 3.6: TEM images (scale bar = 10 nm) showing UV-cleaned and solvent-cleaned Pt-PVP nanoparticles under reaction conditions. For 4.2 and 3.0 nm nanoparticles, 60 min of UV treatment resulted in clustering, with neighboring nanoparticles moving closer to each other while maintaining their size. Under hydrogenation reaction conditions (200 Torr H_2, 560 Torr Ar, 373 K), clustered nanoparticles often melted together to produce much larger particles. Spherical 1.7 nm nanoparticles aggregated after 60 min of UV treatment. In contrast, under hydrogenation reaction conditions (200 Torr H_2, 560 Torr Ar) solvent-cleaned Pt-PVP nanoparticles did not exhibit changes up to at least 473 K.

Figure 3.6 also shows TEM images demonstrating the stability of solvent-cleaned Pt nanoparticles. These images show solvent-cleaned nanoparticles of 4.2, 3.0, and 1.7 nm sizes after H_2 exposure at 473 K (i.e., 100 K higher temperature than that applied to UV-cleaned nanoparticles). It is clear that solvent-cleaned nanoparticles are very stable because they appear the same as the untreated LB film. This represents the major advantage of solvent cleaning compared to UV cleaning. Although UV cleaning is effective in removing PVP, it compromises nanoparticle stability under reaction conditions, resulting in the loss of size monodispersity. Alternatively, solvent cleaning produces stable nanoparticle catalysts that allow for nanoscale size effects of selectivity to be studied by SFG vibrational spectroscopy.

3.3.3 Effect of Solvent and UV Cleaning on Number Density of Pt Active Sites

The role of solvent and UV cleaning on the number of available active sites of Pt nanoparticles was examined with ethylene hydrogenation experiments performed at 298 K. Ethylene hydrogenation on Pt is a structure insensitive reaction with a well-characterized turnover frequency.[26] Accordingly, the activity of a catalyst for ethane production from ethylene can be used to determine the number of active Pt sites on the catalyst.

Figure 3.7 shows the number density of active sites for fully-capped, solvent-cleaned, and UV-cleaned 4.2 nm Pt-PVP films. Surface coverage of the nanoparticles was controlled by the surface pressure applied during LB film deposition and should not vary significantly among samples. For a surface pressure of 20 mN/m, surface coverage by the nanoparticles was found to be 30–50%. Assuming 4.2 nm spherical nanoparticles with a (111) surface and no poisoning by the PVP capping agent, this surface coverage implies 2×10^{15} Pt sites per cm^2.

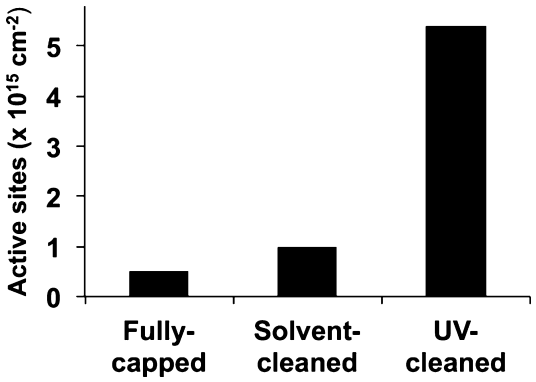

Figure 3.7: Active sites on layers of fully-capped, solvent-cleaned, and UV-cleaned 4.2 nm Pt nanoparticles with PVP capping agent determined from ethylene hydrogenation.

Fully-capped nanoparticles contain 5×10^{14} active Pt sites per cm^2, as determined from ethylene hydrogenation measurements, representing 20% of the apparent area. UV-cleaned nanoparticle LB films demonstrate higher densities of active sites by about an order of magnitude. Using ethylene hydrogenation measurements, the number densities of active sites on solvent- and UV-cleaned nanoparticle films are estimated to be 1×10^{15} and 4×10^{15} active sites per cm^2, corresponding to 40 and >100% of the apparent area, respectively. The higher activity of the UV-cleaned nanoparticles is attributed to a deviation of the actual number of active sites per nanoparticle from what is expected by assuming a sphere with a perfect (111) surface. However, this comparison is still insightful and shows that although solvent cleaning increases the available number of Pt sites by a factor of 2, UV cleaning is much more effective in removing PVP, increasing the number of available Pt sites by a factor of 10. This may also explain the instability of UV-cleaned nanoparticles during reaction compared to solvent-cleaned nanoparticles. It appears that solvent-cleaned nanoparticles are stabilized by a significant amount of PVP that covers more than half of the nanoparticle surface.

3.4 Conclusions

Two major challenges of observing catalytic reaction intermediates on ligand-capped nanoparticles were addressed in this study – interference by the organic capping agent in the SFG signal and blocking of active sites. Under hydrogenation reaction conditions, the capping agent (PVP) undergoes disordering on Pt, resulting in negligible SFG signal from PVP in the C–H stretch range. This is significant because it provides a clean background for probing reaction intermediates with SFG vibrational spectroscopy. Solvent cleaning removes PVP and increases the number of Pt active sites. This enhances catalytic activity and allows reaction intermediates to be observed with SFG. Although a larger increase in catalytic activity can be obtained with UV cleaning, this method results in aggregation of nanoparticles during reaction at temperatures as low as 373 K. However, solvent-cleaned nanoparticles demonstrate good stability up to at least 473 K. Accordingly, solvent cleaning is desirable when probing size and shape effects on nanoparticle catalysts, because it allows for SFG studies to be carried out without compromising size monodispersity under reaction conditions.

3.5 References

(1) Shen, Y. R. *Nature* **1989**, *337*, 519.
(2) Lambert, A. G.; Davies, P. B.; Neivandt, D. J. *Appl. Spectrosc. Rev.* **2005**, *40*, 103.
(3) Kliewer, C. J.; Bieri, M.; Somorjai, G. A. *J. Am. Chem. Soc.* **2009**, *131*, 9958.
(4) Yang, M.; Somorjai, G. A. *J. Am. Chem. Soc.* **2004**, *126*, 7698.
(5) Yang, M.; Chou, K. C.; Somorjai, G. A. *J. Phys. Chem. B* **2003**, *107*, 5267.
(6) Bratlie, K. M.; Komvopoulos, K.; Somorjai, G. A. *J. Phys. Chem. C* **2008**, *112*, 11865.
(7) Kliewer, C. J.; Aliaga, C.; Bieri, M.; Huang, W.; Tsung, C.-K.; Wood, J. B.; Komvopoulos, K.; Somorjai, G. A. *J. Am. Chem. Soc.* **2010**, *132*, 13088.
(8) Bratlie, K. M.; Lee, H.; Komvopoulos, K.; Yang, P.; Somorjai, G. A. *Nano Lett.* **2007**, *7*, 3097.
(9) Kuhn, J. N.; Huang, W.; Tsung, C.-K.; Zhang, Y.; Somorjai, G. A. *J. Am. Chem. Soc.* **2008**, *130*, 14026.
(10) Somorjai, G. A.; Park, J. Y. *J. Chem. Phys.* **2008**, *128*, 182504.
(11) Lee, I.; Delbecq, F.; Morales, R.; Albiter, M. A.; Zaera, F. *Nat. Mater.* **2009**, *8*, 132.

(12) Narayanan, R.; El-Sayed, M. A. *Nano Lett.* **2004**, *4*, 1343.
(13) Borodko, Y.; Humphrey, S. M.; Tilley, T. D.; Frei, H.; Somorjai, G. A. *J. Phys. Chem. C* **2007**, *111*, 6288.
(14) Ullah, M. H.; Chung, W. S.; Kim, I.; Ha, C. S. *Small* **2006**, *2*, 870.
(15) Kim, J.; Chou, K. C.; Somorjai, G. A. *J. Phys. Chem. B* **2003**, *107*, 1592.
(16) Ramirez, E.; Eradeѐ, L.; Philippot, K.; Lecante, P.; Chaudret, B. *Adv. Funct. Mater.* **2007**, *17*, 2219.
(17) Zheng, H.; Smith, R. K.; Jun, Y.-W.; Kisielowski, C.; Dahmen, U.; Alivisatos, A. P. *Science* **2009**, *324*, 1309.
(18) Aliaga, C.; Park, J. Y.; Yamada, Y.; Lee, H. S.; Tsung, C. K.; Yang, P. D.; Somorjai, G. A. *J. Phys. Chem. C* **2009**, *113*, 6150.
(19)Vidal-Iglesias, F.J.; Solla-Gulloń, J.;Herrero, E.;Montiel, V.; Aldaz, A.; Feliu, J. M. *Electrochem. Commun.* **2011**, *13*, 502.
(20) Su, X. C.; Kung, K.; Lahtinen, J.; Shen, R. Y.; Somorjai, G. A. *Catal. Lett.* **1998**, *54*, 9.
(21) Su, X. C.; Kung, K. Y.; Lahtinen, J.; Shen, Y. R.; Somorjai, G. A. *J. Mol. Catal A: Chem.* **1999**, *141*, 9.
(22) McCrea, K. R.; Somorjai, G. A. *J. Mol. Catal A: Chem.* **2000**, *163*, 43.
(23) Yang, M.; Somorjai, G. A. *J. Phys. Chem. B* **2004**, *108*, 4405.
(24) Yang, M. C.; Chou, K. C.; Somorjai, G. A. *J. Phys. Chem. B* **2004**, *108*, 14766.
(25) Manner, W. L.; Girolami, G. S.; Nuzzo, R.G. *J. Phys. Chem. B* **1998**, *102*, 10295.
(26) Kuhn, J. N.; Tsung, C.-K.; Huang, W.; Somorjai, G. A. *J. Catal.* **2009**, *265*, 209.
(27) Rioux, R. M.; Song, H.; Hoefelmeyer, J. D.; Yang, P.; Somorjai, G. A. *J. Phys. Chem. B* **2005**, *109*, 2192.
(28) Song, H.; Kim, F.; Connor, S.; Somorjai, G. A.; Yang, P. D. *J. Phys. Chem. B* **2005**, *109*, 188.
(29) Kweskin, S. J.; Rioux, R. M.; Habas, S. E.; Komvopoulos, K.; Yang, P.; Somorjai, G. A. *J. Phys. Chem. B* **2006**, *110*, 15920.
(30) Curtis, A. D.; Burt, S. R.; Calchera, A. R.; Patterson, J. E. *J. Phys. Chem. C* **2011**, *115*, 11550.
(31) Borodko, Y.; Habas, S. E.; Koebel, M.; Yang, P. D.; Frei, H.; Somorjai, G. A. *J. Phys. Chem. B* **2006**, *110*, 23052.
(32) Rumpel, A.; Novak, M.; Walter, J.; Braunschweig, B.; Halik, M.; Peukert, W. *Langmuir* **2011**, *27*, 15016.
(33) Perry, D. A.; Hemminger, J. C. *J. Am. Chem. Soc.* **2000**, *122*, 8079.
(34) Hirschl, R.; Delbecq, F.; Sautet, P.; Hafner, J. *J. Catal.* **2003**, *217*, 354.
(35) Vig, J. R. *J. Vac. Sci. Technol. A* **1985**, *3*, 1027.

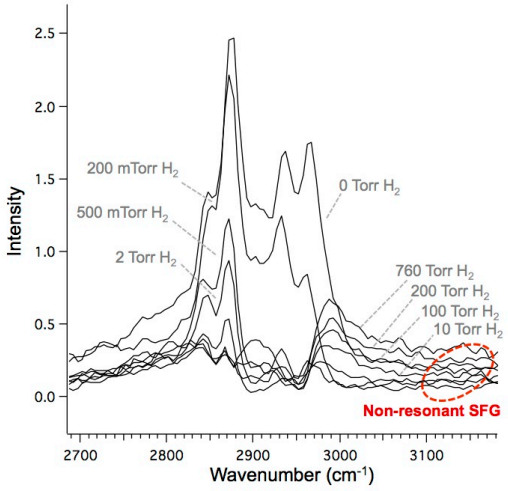

Figure S.3.1: Solvent-cleaned 4.2 nm Pt-PVP exposed to different levels of H_2 (0-760 Torr) with Ar fill at 298 K. Signal from PVP is significantly reduced with only 2 Torr H_2. As H_2 pressure is increased, a relatively flat non-resonant feature begins to grow above 3000 cm^{-1}. The non-resonant contribution depends on wavenumber frequency.

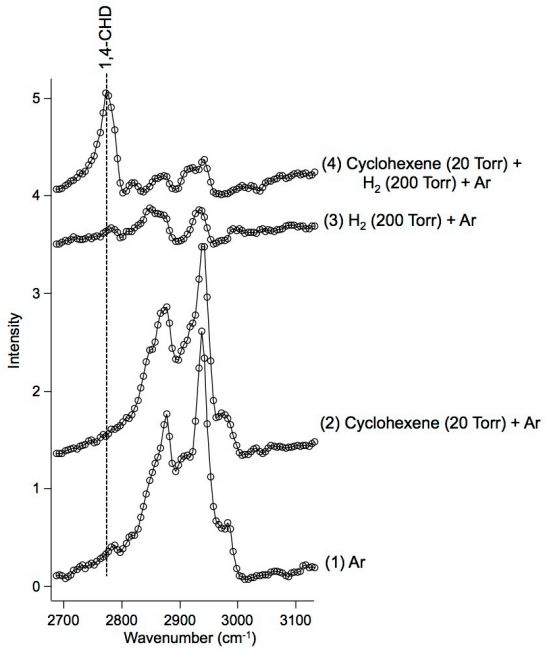

Figure S.3.2A: Sequential SFG experiment (1→4) on 1.7 nm Pt-PVP at 298 K comparable to Figure 3.3. Without H_2 no 1,4-CHD peak is observed. Under reaction conditions (4), as expected, PVP is disordered and a major peak at 2765 cm^{-1} (1,4-CHD) appears, like on 4.2 nm Pt-PVP.

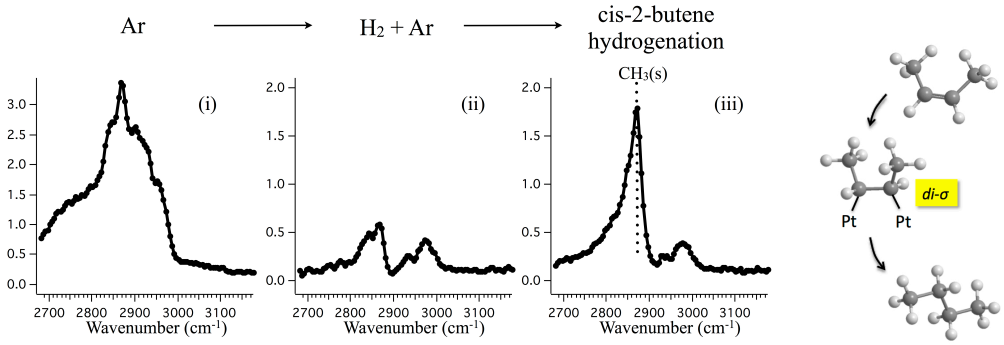

Figure S.3.2B: SFG spectra of heavily washed 3.0 nm Pt nanoparticles treated to a sequence of conditions at 298 K: 760 Torr Ar (first column), 200 Torr H_2 and 560 Torr Ar (second column), 50 Torr cis-2-butene with 200 Torr H_2 and 510 Torr Ar (third column). Substantial growth is observed when cis-2-butene is introduced at 2870 cm^{-1} (CH_3(s)). The CH_3(s) indicates the presence of the *di-σ* reactive intermediate adsorbed on the surface of Pt.

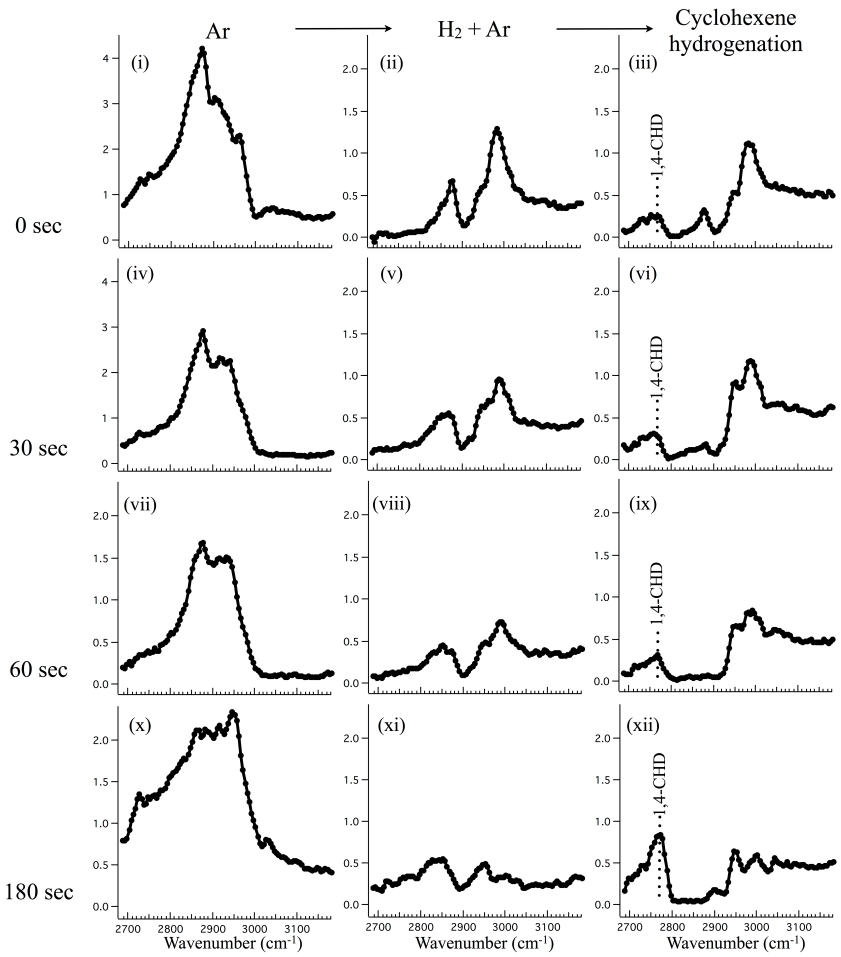

Figure S.3.3A: SFG spectra collected at 295 K after UVO treatments (0 to 180 sec). Each LB film was treated with UVO, then exposed to 760 Torr Ar (left column), then 200 Torr H_2 and 560 Torr Ar (middle column) and finally, 10 Torr cyclohexene, 200 Torr H_2 and 550 Torr Ar (right column). In the right column the only evidence of a cyclohexene hydrogenation intermediate is 1,4-CHD. All other features are attributed to residual PVP.

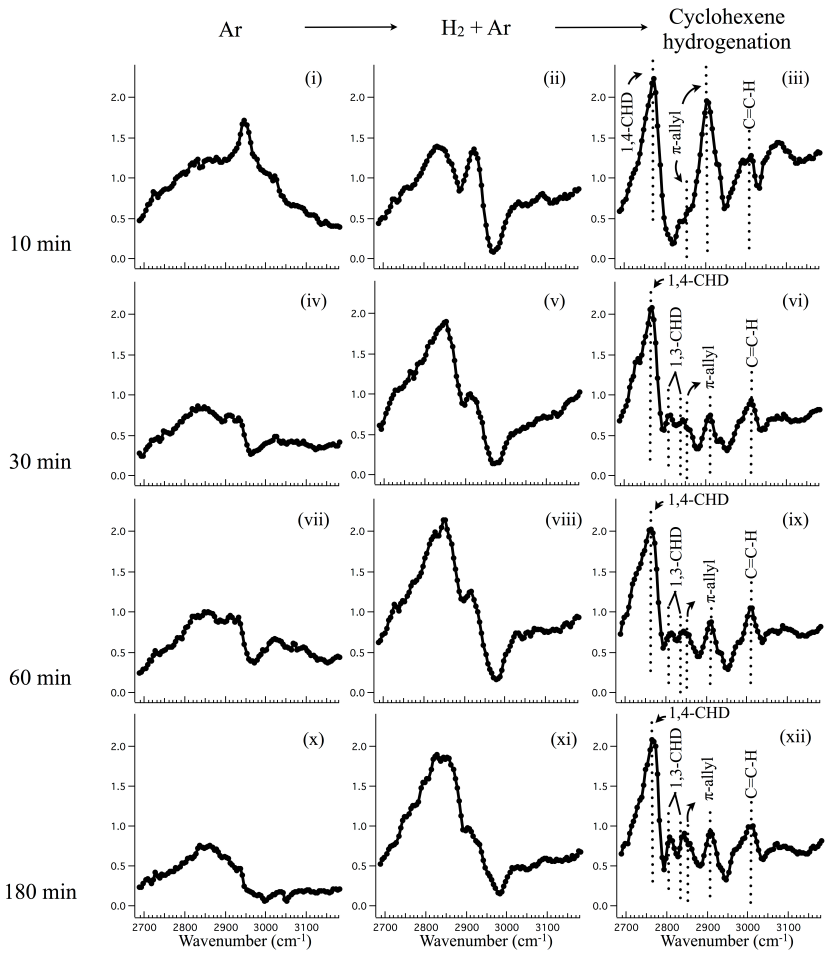

Figure S.3.3B: SFG spectra collected at 295 K after UVO treatments (10 to 180 min). Each LB film was treated with UVO, then exposed to 760 Torr Ar (left column), 200 Torr H_2 and 560 Torr Ar (middle column) and finally, 10 Torr cyclohexene, 200 Torr H_2 and 550 Torr Ar (right column). All features in the right column are attributed to cyclohexene hydrogenation intermediates: 1,4-CHD, 1,3-CHD and the π-allyl. For (v), (viii) and (xi), the growth is due to the hydrogenation of residual C fragments under H_2 atmosphere. A peak at 2950 cm^{-1} (possibly CH_3(a,p)) is observed in (i) and (ii) originating from residual PVP not removed by UV cleaning. Both (i) and (ii) also show a significant non-resonant background. Because of the change in peak shape from (i) to (ii) centered at 2950 cm^{-1}, it is clear the addition of H_2 changes the phase of the CH_3(a,p) resonant peak or the non-resonant background by ~90°. Comparing the H_2 spectra in

Figures S.3.1A and S.3.1B, it is clear that the lowest background occurs when more PVP is present (disordering effect). When almost all PVP is removed (30-180 min), the hydrogenation of residual fragments produce a significant background which may interfere with the identification of reaction intermediates. Nonetheless, the features of the background (reversibly) disappear under cyclohexene hydrogenation conditions (vi, ix, xii).

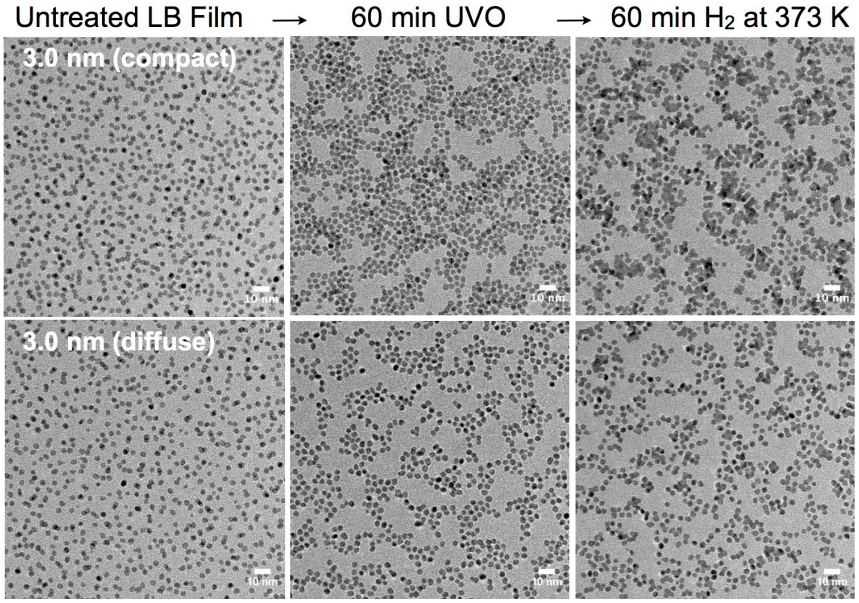

Figure S.3.4: TEM images comparing two different LB film compressions of the same 3.0 nm Pt-PVP nanoparticles. Aggregation is more pronounced at high compression, however, is apparent even when the film is diffuse because Pt nanoparticles can move on the substrate. Even for diffuse films, aggregation is a problem.

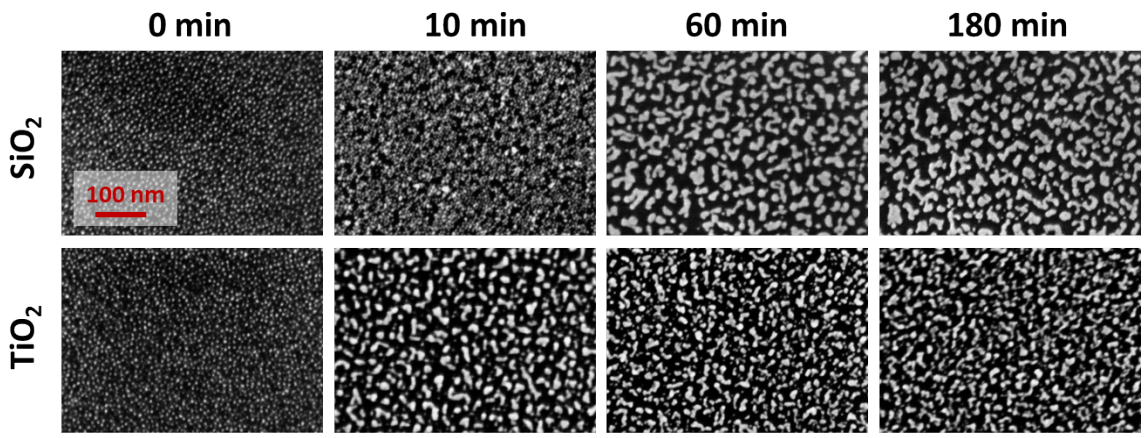

Figure S.3.5: SEM images showing aggregation at different UVO treatment times (0-180 min) following furfural hydrogenation reaction conditions at 120 °C. PVP removal with UV treatment results in the loss of morphological stability of Pt nanoparticles under reaction conditions. These results indicate the loss of PVP, not effects from the substrate (TiO_2 or SiO_2), is primarily responsible for aggregation.

Chapter 4: The Role of an Organic Cap in Nanoparticle Catalysis: Reversible Restructuring of Carbonaceous Material Controls Catalytic Activity of Platinum Nanoparticles for Ethylene Hydrogenation and Methanol Oxidation

4.1 Introduction

Traditional methods for catalyst preparation (i.e., incipient wetness and ion exchange) use the reduction of a metal salt inside of a mesoporous oxide.[1,2] The result is a high surface area catalyst consisting of metal particles with a broad distribution of sizes and morphologies. This type of polydisperse heterogeneous catalyst masks the structure sensitivity inherent in heterogeneous catalysis[3-6] because with this method it is not possible to select nanoparticles of a single size or shape. Recent advances in nanoscience have shown that colloidal synthetic methods can produce monodisperse nanoparticles with well-defined sizes and shapes.[7-11] This advance marked a new era in heterogeneous catalysis where monodisperse nanoparticles serve as model catalysts[12-14] and these catalysts have shown that size and shape control the catalytic activity and selectivity for many reactions.[15-21] These results indicate that colloidal nanoscience is an important tool for the development of new highly selective catalysts necessary to minimize the environmental impact and improve the economic efficiency of numerous commercial chemical processes.

In colloidal synthetic methods, nanoparticles are necessarily encapsulated in anorganic polymer or surfactant. This organic coating lowers the surface energy of the nanoparticle to prevent aggregation of the particles;[11] the cap may also help to control the size and shape of the nanoparticles.[22] This gives rise to an important question regarding the effect of the organic cap on the catalytic properties of the nanoparticles. It is traditionally thought that the cap acts as a site blocking agent and lowers the metal surface area available for catalytic reaction.[23] In this light, it has been assumed that colloidal preparation methods are impractical for commercial

catalytic applications because the presence of the capping agent decreases the apparent metal dispersion. However, this is an incomplete assumption based on a model that considers the cap as a passive coating rather than a dynamic shell that can adjust under reaction conditions.
It has been observed in the case of Pt–dendrimer complexes that the dendrimer structure, which is highly sensitive to gas/liquid conditions, controls access to the Pt surface.[24] Although the dendrimer blocks the Pt surface in air, it adopts an open structure in water that allows ready access of gasses to the Pt surface. Despite the importance of this effect for nanoparticle catalysis, little effort has been made to directly probe the role of a nanoparticle cap to mediate surface adsorption and catalytic activity. In this work we find that Pt nanoparticles capped with either poly(vinylpyrrolidone) (PVP) or oleic acid (OA) are active for both ethylene hydrogenation and methanol oxidation showing that the organic coating does not prevent nanoparticle catalysis. When the organic coating is removed either by UV light or thermal oxidation, the activity for ethylene hydrogenation increases while the activity for methanol oxidation decreases to almost zero. This surprising result shows that the capped nanoparticles are more active for methanol oxidation than their cleaned analogues.

Because of the high surface energy of metals, it is not possible to maintain a clean metal surface, even under conditions of ultra-high vacuum. With this in mind, it is clear that even catalysts prepared by traditional methods also become "capped" with undefined surface species as these catalysts quickly become contaminated in ambient conditions or during reaction.[25] Accordingly, the capping agent on colloidal nanoparticles represents a well-controlled passivation layer which, as shown here, does not prevent catalysis under reaction conditions. The concept of using an organic coating to increase catalytic activity of a nanoparticle is reminiscent of homogeneous

catalysis where ligands are used to tune the activity and selectivity of single metal ions,[26] and several examples have already shown that similar effects are also possible on metal clusters.[27,28]

The present work investigates the role of PVP to mediate the catalytic properties of encapsulated Pt nanoparticles. We probe the molecular structure of the PVP cap by sum frequency generations (SFG) vibrational spectroscopy. Ethylene hydrogenation and methanol oxidation then serve as model reactions to probe the catalytic activity in reducing and oxidizing conditions, respectively. Spectral results show that the PVP cap has a strong SFG signal in O_2 atmosphere but disorders in H_2 atmosphere. However, kinetic measurements for ethylene hydrogenation and methanol oxidation show that this capping layer still allows catalysis regardless of the gas conditions. When the PVP is removed by photodecomposition using UV light, carbonaceous fragments remain on the surface that reversibly restructure in H_2 and O_2. In O_2 atmosphere, these carbonaceous fragments form a tightly closed shell around the nanoparticles that blocks catalytic activity, but this shell opens in H_2. As a result, following UV cleaning the nanoparticles are highly active for ethylene hydrogenation but not for methanol oxidation. Kinetic experiments on thermally-cleaned PVP- and OA-capped nanoparticles show similar results indicating that these findings apply to multiple capping agents and cleaning methods. This work highlights the dominant role of an organic coating to mediate nanoparticle catalysis and provides methanol oxidation as one example where capped nanoparticles are dramatically better catalysts than their cleaned analogues.

4.2 Experimental

4.2.1 Nanoparticle Synthesis. The Pt nanoparticles were synthesized from chloroplatinic acid hexahydrate and PVP in a 1:4 mass ratio. In a small beaker, 110 mg of chloroplatinic acid was dissolved in 10 mL ethylene glycol. In a separate beaker, 440 mg of PVP was dissolved in 10 mL of ethylene glycol. Once in solution, the two mixtures were combined into a 50 mL two-neck round bottom flask. The solution was purged under vacuum for 15 min. The vessel was then heated to 438 K for 1 h with vigorous mixing under a flow of argon. The resulting nanoparticles were precipitated with acetone and washed three times with ethanol and hexanes. The nanoparticles were then suspended in chloroform. Transmission electron microscopy (TEM) showed that the particles were 4.6 ± 2.8 nm.

To investigate the effect of different capping agents and cleaning methods on reaction kinetics, Pt nanoparticles were synthesized using an alternate method where the capping agent is added after synthesis. This allowed us to add different capping agents to identical nanoparticle aliquots to isolate the cap as the sole variable between two nanoparticle samples.[23] In a small beaker, 350 mg of chloroplatinic acid was dissolved in 17.5 mL ethylene glycol. In a separate beaker, 350 mg of NaOH was dissolved in 17.5 mL ethylene glycol. Once in solution, the two mixtures were combined in a 50 mL two-neck flask. The solution was purged under vacuum for 15 min. The vessel was then heated to 433 K for 3 h with vigorous mixing under a flow of argon. Aliquots (2 mL) of the resulting nanoparticles were precipitated with 2 M HCl, and then re-dispersed in 2 mL ethanol containing 10 mg of either PVP or OA. TEM showed that the particles were 1.7 ± 0.8 nm.

4.2.2 Langmuir–Blodgett Deposition. Formation of 2D films of monodisperse nanoparticles to serve as model catalysts is routinely achieved by Langmuir–Blodgett deposition. This technique has been described previously in detail.[12,29] In short, a suspension of nanoparticles in chloroform is dispersed onto a water surface (18 MΩ). Time is given for the chloroform to evaporate, leaving a 2D dispersion of nanoparticles. The film is then compressed with a mobile barrier, and the surface pressure is monitored as a function of decreasing surface area. The surface pressure corresponds to the density of nanoparticles on the water. When the desired surface pressure is reached, a substrate is pulled out from under the surface of the water, and the film of nanoparticles is deposited onto the substrate. The final density of nanoparticles on the substrate can be controlled by controlling the surface pressure during deposition. A surface pressure of 14 mN/m was used for these studies, and films were deposited using a Nima 611 LB trough. Filter paper served as the surface tension probe.

The substrate used to support the nanoparticles was a TiO_2 thin film (50 nm) deposited on a Si(100) wafer with a thermally grown SiO_2 layer (500 nm). The TiO_2 thin film was deposited on the SiO_2/Si wafer by electron beam evaporation from an oxide source without any substrate heating. Following deposition, the TiO_2 thin film was annealed at 773 K in O_2 to increase crystallinity and ensure a fully oxidized stoichiometry. Analogous samples were prepared for sum frequency generation spectroscopic studies. For these samples, an optically transparent substrate was needed. A sapphire window rather than a Si wafer served as the substrate. A TiO_2 thin film (50 nm) was deposited on the sapphire window by electron beam evaporation, again followed by annealing at 773 K in O_2. The LB technique was then used to deposit a monolayer of the Pt nanoparticles onto the TiO_2 thin films. Electron microscopy showed that the area coverage for Pt on the substrate following LB was 30–50 %. In some cases, TiO_2 used as a Pt

support plays an active role in the catalytic chemistry. However, the conclusions reported here are not substrate dependent, and kinetic results have been obtained for identical nanoparticles supported on SiO_2 substrates, and no significant differences were observed.

LB deposition is challenging for OA-capped Pt nanoparticles owing to the high hydrophobicity of the OA. Consequently, for investigating the role of different capping agents, films of the 1.7 nm PVP- and OA-capped nanoparticles were drop cast on a TiO_2 substrate.

4.2.3 Cap Removal. Immediately prior to reaction, the samples were exposed to UV light in air to remove the PVP capping layer. Two low-pressure mercury (Hg) lamps (Lights Sources Inc., GPH357T5VH/4P) were used as the UV source; the lamps emit at 184 and 254 nm. The two lamps were aligned parallel to each other 2.5 cm apart in a clean Al box. The sample sat 1.2 cm below the lamps. By varying the time of UV exposure, it was possible to control the amount of PVP removed from the Pt nanoparticles. This cleaning is the combined effect of direct photodecomposition of the PVP and oxidation of the PVP by ozone produced from the 184 nm Hg line.[30]

X-ray photoelectron spectroscopy (XPS) was used to observe the removal of PVP from the Pt nanoparticles after UV cleaning. Spectra were obtained using a Physical Electronics system (PHI 5400 ESCA/XPS) with an Al anode source. The analyzer was positioned at 50° relative to sample normal. The C 1s, N 1s, and Pt 4f peak areas were normalized by the appropriate sensitivity factors to obtain the surface C:Pt and N:Pt atomic fractions as a function of UV exposure time. Measurements showed that 90% of the C was removed from the Pt following 3 h UV exposure.

Thermal cleaning in air was used as an alternative to UV cleaning for drop cast samples. For thermal cleaning, the samples were placed in a tube furnace and heated to a desired temperature for 16 h. The PVP- and OA-capped samples were treated at 473 and 573 K, respectively to remove the two capping agents that show different thermal stabilities.

4.2.4 Sum Frequency Generation Vibrational Spectroscopy. Sum frequency generation (SFG) is a second order, nonlinear process that probes the $\chi^{(2)}$ tensor. Because $\chi^{(2)}$ is zero for centrosymmetric media, SFG is only sensitive to a break in inversion symmetry which usually occurs at a surface or interface.[31] Consequently, SFG is useful for obtaining vibrational spectra of surfaces. In this study, SFG is used to obtain the vibrational spectrum of the nanoparticle capping layer in H_2 and O_2 atmospheres.

For SFG experiments, an active/passive mode-locked Nd:YAG laser (Leopard D-20, Continuum) produces 20 ps pulses at a 20 Hz repetition rate. The fundamental output at 1,064 nm was passed through an optical parametric generator/amplifier to generate a tunable infrared (IR) beam (2,700–3,600 cm^{-1}) and a second harmonic visible (VIS) beam (532 nm). The IR (100 μJ) and VIS (100 μJ) beams were spatially and temporally overlapped on the surface of a sapphire window containing the Pt nanoparticles. The VIS and IR beams were incident on the sample at 40° and 50° degrees, respectively, relative to surface normal. The generated SFG signal was then collected and sent to a photomultiplier tube. A gated integrator was used to enhance the signal-to-noise. To collect a spectrum, the IR beam was scanned across the spectral range of interest. All experiments were performed in the ppp polarization combination.

The beams were directed onto the sample using a sapphire prism as shown in Figure 4.1(A). A solution of deuterated polystyrene (d_8) in deuterated decalin (d_{18}) served as an index matching

liquid between the prism and substrate that did not interfere with transmission of the IR beam at the C–H stretch frequency. The catalyst surface was pressed into thermal contact with an aluminum heating block to heat the catalyst to the desired temperature. A recess in the heating block allowed for the flow of gasses across the catalyst surface. A metal bellows circulation pump provided gas mixing. A gas tight seal was made between the sapphire window and the heating block using a Kalrez O-ring.

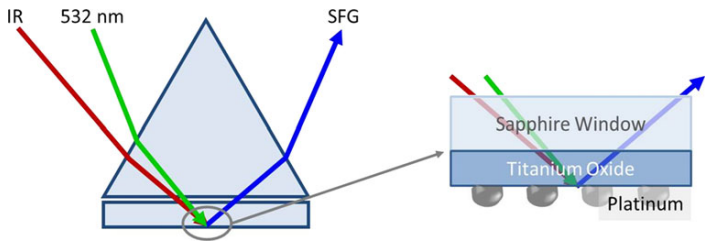

Figure 4.1: Diagram showing how a sapphire prism directed the VIS and IR beams onto the catalyst surface for SFG vibrational spectroscopy. The catalyst was prepared on the back side of a sapphire window and consisted of a thin film of TiO_2 acting as a support for Pt nanoparticles.

4.2.5 Kinetic Measurements. A stainless steel batch mode reactor was used to determine the reaction rates for ethylene hydrogenation and methanol oxidation on the Pt nanoparticle catalysts before and after UV cleaning. The catalyst temperature was controlled with a boron nitride substrate heater. A metal bellows circulation pump provided gas mixing. For ethylene hydrogenation, gas pressures were 10 Torr ethylene, 100 Torr H_2, and 650 Torr He, and the catalyst temperature was 298 K. For methanol oxidation, gas pressures were 10 Torr methanol, 50 Torr O_2, and 700 Torr He, and the catalyst temperature was 333 K. The methanol was purified by freeze-pump-thawing cycles. Each catalyst was tested for 2 h, and reaction products were monitored as a function of time using a gas chromatograph with a thermal conductivity detector.

Rates for ethylene hydrogenation and methanol oxidation were measured on each catalyst before and after cleaning.

4.3 Results and Discussion

Figure 4.2(A) shows the SFG spectra of PVP-capped Pt nanoparticles in sequential gas environments. As the gas environment is initially cycled between H_2 and O_2, the SFG signal is higher in O_2 and decreases in H_2 corresponding to a structural reconfiguration of PVP on the Pt, and this effect has been discussed previously.[32] In summary, because of selection rules, SFG is sensitive not only to the individual molecular susceptibilities, but also to the net susceptibility of the entire ensemble of molecules at an interface. This net susceptibility depends strongly on the relative orientation of molecules at the interface. It is usually assumed that systems showing greater SFG signal intensity have a more highly ordered interface than those showing weaker intensity because a net disorder leads to canceling out of signal from individual molecular oscillators. Accordingly, we assign the loss of signal intensity going from O_2 to H_2 atmosphere as H_2-induced disordering of the PVP. However, after the first H_2/O_2 cycle, the PVP settles into a relatively stable configuration on the Pt, and minimal restructuring occurs as the gas environment continues to change between reducing and oxidizing conditions.

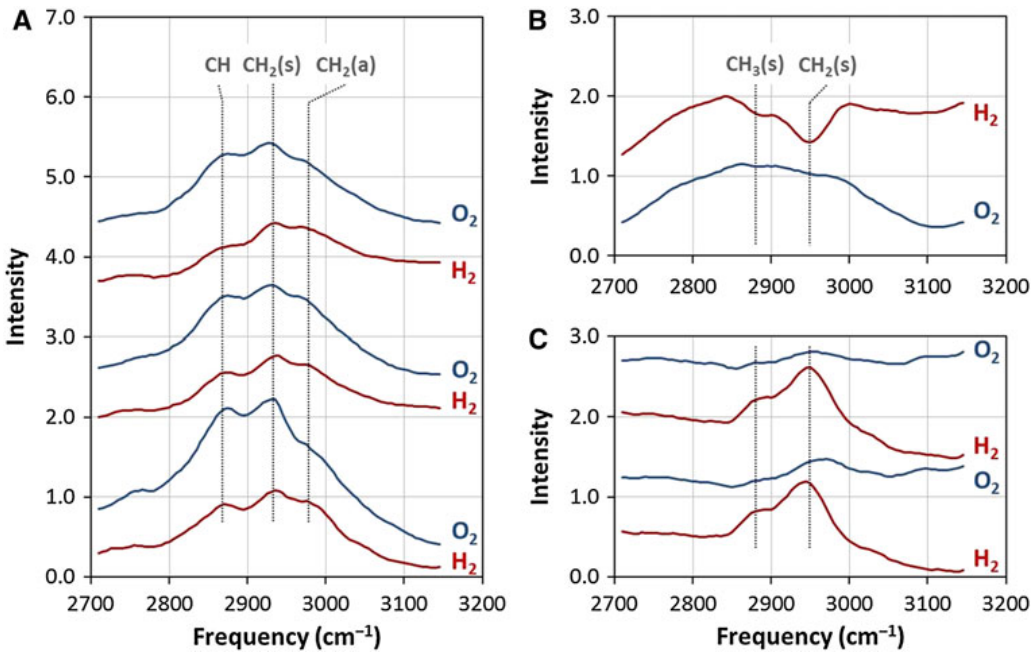

Figure 4.2: SFG spectra of the PVP-capped Pt nanoparticles before UV cleaning (A) and after UV cleaning for 10 min (B and C). Spectra were obtained in 100 Torr of H_2 or O_2 in a background of Ar at 60 °C. A boxcar average over 5 data points improved signal-to-noise. In (A) and (C) the spectra are arbitrarily offset for clarity and were obtained sequentially from bottom to top. (B) Shows the raw spectra with no offset of UV-cleaned nanoparticles first in H_2 then in O_2. The spectrum obtained in H_2 shows a much higher nonresonant intensity with resonant features appearing as dips in the high background. This is a result of the phase mismatch between the resonant and nonresonant contributions of the spectrum. By subtracting the raw spectra from a baseline obtained in Ar, the negative features are inverted to appear positive for clarity (shown in (C)). Analysis of the resonant features in these spectra shows that before UV cleaning the PVP has a conformation that does not significantly change depending on the gas environment. However, following UV cleaning, carbonaceous fragments are found on the surface that are dynamic and reversibly restructure in H_2 and O_2.

This is in strong contrast to spectra shown on identical nanoparticles following UV cleaning to remove PVP from the Pt surface. Figure 4.2(B) shows the raw spectra of UV-cleaned nanoparticles first in H_2 then in O_2. The spectrum obtained in H_2 shows a much higher nonresonant intensity with resonant features appearing as negative peaks against the high background. This effect, which is common in SFG, is a result of the phase mismatch between the resonant and nonresonant contributions of the spectrum. By subtracting the raw spectra from a baseline obtained in Ar, the negative features are inverted to appear positive for clarity (see Figure 4.2(C)). The enhanced nonresonant signal of the UV-cleaned catalyst is a result of H spillover from the Pt resulting in a reduced TiO_2 support, and the effect is completely reversible in O_2. In the PVP-capped sample, the nonresonant contribution to the spectrum is low even in H_2 because the PVP blocks H spillover to the TiO_2.

Figure 4.2(C) shows that after UV cleaning as the atmosphere is cycled between H_2 and O_2, carbonaceous fragments are present on the Pt surface, and these fragments reversibly restructure, adopting a structure that is strongly SFG active in H_2, and a structure which is almost entirely SFG inactive in O_2. It may be tempting to conclude that O_2 reacts with the remaining cap on the Pt surface to catalyze its complete removal. However, this is not the case as can be seen by the reversible appearance of the molecular vibrations when H_2 is re-introduced to the system. This change occurs reversibly over multiple cycles with no sign of signal decrease over time that would suggest eventual removal of the carbonaceous fragments.

It is also evident that the vibrational modes observed following UV cleaning are not the same as those observed from the intact PVP cap. Initially the vibrational modes observed on PVP-capped

Pt (see Figure 4.2(A)) match closely the assignments previously reported by infrared and Raman for PVP–Pt complexes.[32] Following UV cleaning, the peaks observed are attributable to CH_2 and CH_3 symmetric stretching modes outside of a 5-membered ring. It is also important to note that XPS measurements indicate that the surface C has decreased more than 85 % compared to the fully-capped nanoparticles following UV cleaning. It is not definitive whether the carbonaceous fragments observed by SFG after cleaning are photodecomposition products of PVP, or if they represent contamination of the UV-cleaned Pt surface, which would be unavoidable in ambient. However, it is clear that additional UV cleaning does little to remove these species.

Figure 4.3 shows the catalytic activity of the Pt nanoparticles for ethylene hydrogenation and for methanol oxidation before and after UV cleaning. We selected these two reactions because they operate at low temperature (i.e., 298 and 333 K, respectively) and allowed us to observe the effects of the cap structure on the catalytic activity of the nanoparticles in H_2 and O_2 atmospheres. The PVP-capped Pt nanoparticles are active for both reactions as shown in Figures 4.3(A) and 4.3(B). However, following UV cleaning, the activity of the nanoparticles for ethylene hydrogenation and methanol oxidation diverge. Figures 4.3(C) and 4.3(D) show that following UV cleaning, the rate of ethylene hydrogenation increases by a factor of 10 while the rate of methanol oxidation decreases by a factor of 3. This represents a 30-fold divergence on the effect of UV cleaning for these two reactions. We note that formaldehyde is also formed at ~30 % selectivity during methanol oxidation. Formaldehyde production is not shown in Figure 4.3 because it follows the same trend as CO_2.

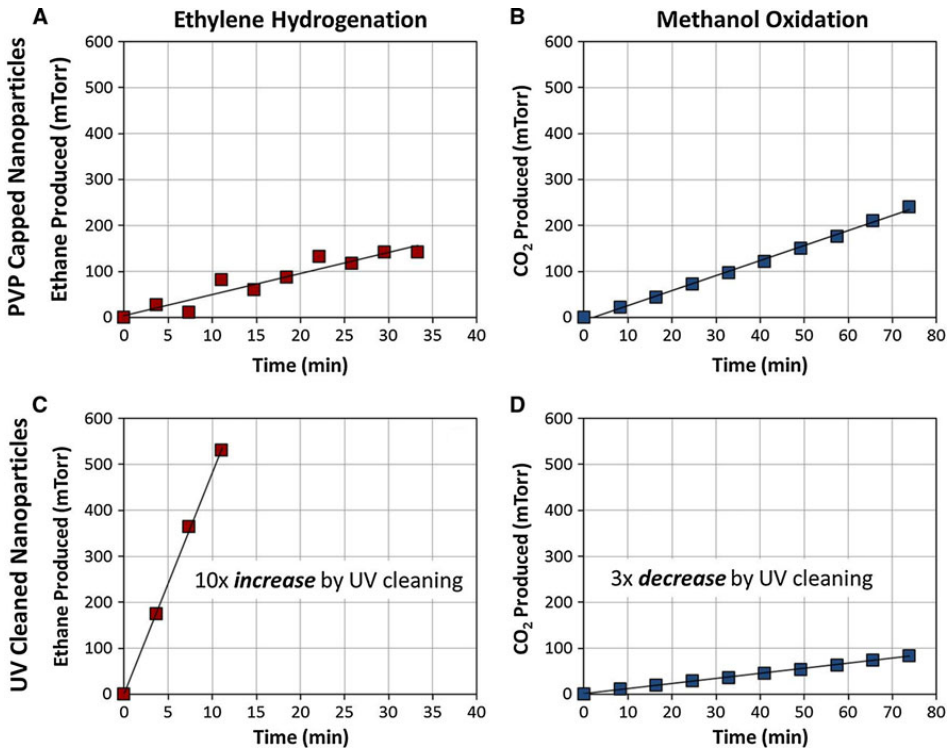

Figure 4.3: Formation of reaction products as a function of time on the Pt nanoparticles for ethylene hydrogenation and methanol oxidation before UV cleaning (A, B) and after UV cleaning for 10 min (C, D). These results show that UV cleaning has a diverging effect on the rates of ethylene hydrogenation which increases by a factor of 10 and methanol oxidation which decreases by a factor of 3. Only CO_2 production is shown for methanol oxidation. However, formaldehyde was also produced as a minor product before and after UV cleaning.

Figure 4.4 shows the activity of the catalyst following UV cleaning where the catalyst is cycled several times between ethylene hydrogenation and methanol oxidation. The rates are normalized to the initial rate for each reaction prior to UV cleaning. It can be seen that the rates for both ethylene hydrogenation and methanol oxidation are reversibly affected by the removal of the PVP cap. It is clear from previous studies that the thermal stability of the nanoparticles decreases following cap removal, so the UV-cleaned nanoparticles agglomerate during reaction.[32]

Nanoparticle agglomeration results in a loss of Pt surface sites which would lead to a decrease in catalyst activity. However, the ethylene hydrogenation kinetics show that the removal of PVP more than compensates for nanoparticle agglomeration resulting in a tenfold net increase in the reaction rate. Consequently, the loss of activity for methanol oxidation following UV cleaning cannot simply be a result of nanoparticle agglomeration which would not be reversible between reactions.

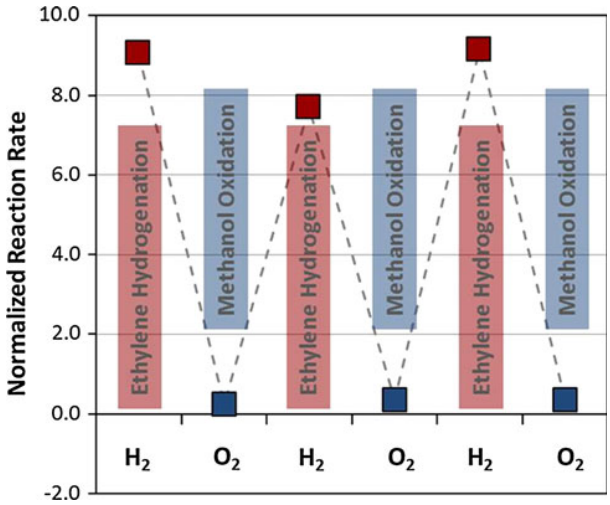

Figure 4.4: The reaction rates for ethylene hydrogenation and methanol oxidation on a single catalyst following UV cleaning for 10 min. The reaction rates are normalized to the initial rate for each reaction before UV cleaning. The results show that the diverging effect of UV cleaning on the two reactions is reversible and appears to correlate with the restructuring of carbonaceous fragments on the Pt surface observed by SFG.

In the case of ethylene hydrogenation, the increase in catalyst activity after cleaning is easily understood based on the increased number of Pt sites available following PVP removal. In the case of methanol oxidation, it is surprising that cap removal would have a negative effect on the catalytic activity. It appears that the structure of the carbonaceous fragments observed on the Pt

following UV cleaning controls the catalytic properties of the uncapped nanoparticles. We suggest that these carbonaceous fragments which do little to prevent access to the Pt in H_2 atmosphere, collapse to a tightly closed shell around the Pt in O_2 atmosphere.

To confirm this model in which carbonaceous fragments form a porous coating around the Pt in H_2 but collapse to a tightly closed shell in O_2, we used cyclohexene to probe the accessibility of reactants to the Pt surface. Cyclohexene forms a 1,4-cyclohexadiene surface intermediate on Pt.[34] This is a dehydrogenation product of the cyclohexene and forms even in the absence of H_2. The 1,4-cyclohexadiene species has a distinct molecular vibration at 2,760 cm^{-1} which is spectrally well resolved from any resonant modes of the capping agent. Consequently, cyclohexene represents a suitable probe molecule. To avoid changes in the nonresonant background with changing H_2 pressure, this experiment was performed using Pt nanoparticles supported directly on an SiO_2 prism. Figure 4.5 shows the results of this experiment. When cyclohexene is introduced in the gas phase to UV-cleaned Pt nanoparticles, no 1,4-cyclohexadiene is observed in the SFG spectrum. Only weak features at 2,840 and 2,910 cm^{-1} appear which we attribute to physisorbed cyclohexene. However, as the H_2 pressure is increased from 0 to 200 Torr, a strong feature at 2,760 cm^{-1} grows in corresponding to 1,4-cyclohexadiene. Because this feature forms on an atomically clean Pt single crystal surface even in the absence of H_2 (ref. 34) we conclude that for the UV-cleaned nanoparticles H_2 is needed to open the carbonaceous shell and allow cyclohexene to access the Pt. It is important to note that in this experiment the nanoparticles were pre-reduced with H_2, so that the oxidation state of Pt is not changing during the experiment.

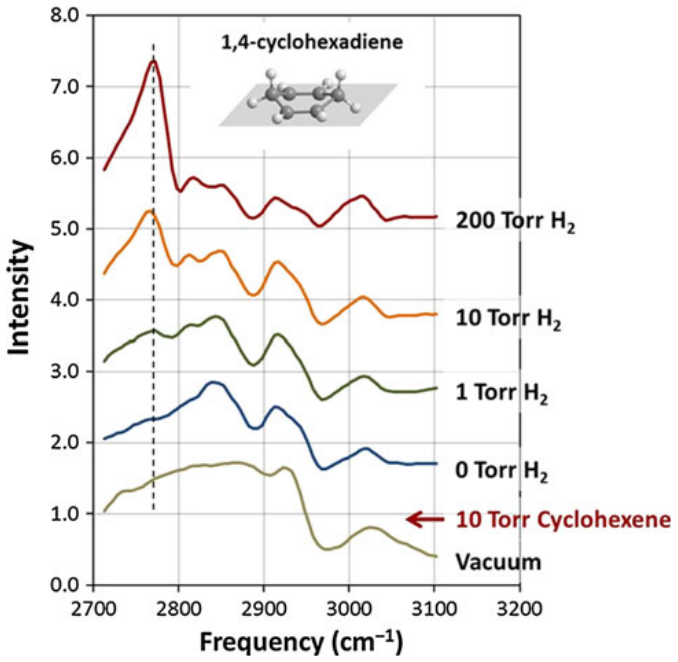

Figure 4.5: SFG spectra of 10 Torr cyclohexene in increasing H_2 pressure on Pt nanoparticles after UV cleaning for 60 min. In this experiment, the nanoparticles are supported directly on a SiO_2 prism. Cyclohexene dehydrogenates on Pt to form a 1,4-cyclohexadiene surface intermediate that is characterized by a strong feature in the SFG spectrum at 2,760 cm^{-1}. This feature is known to form on an atomically clean Pt surface even in the absence of H_2. In this case, the feature is initially absent from the spectrum, but grows in with increasing H_2 pressure. This indicates that H_2 is needed to open the carbonaceous shell on the UV-cleaned Pt nanoparticles and allow cyclohexene to access the Pt.

Figure 4.6(A) shows the effect of UV cleaning time on the activity of the Pt nanoparticles for ethylene hydrogenation and methanol oxidation. The activity for each reaction is normalized to the initial activity of the PVP-capped nanoparticles before UV cleaning. For ethylene hydrogenation the rate increases with increased cleaning time, while for methanol oxidation the rate decreases with increased cleaning time. Following 3 h there is a 200-fold divergence of the

rates for these two reactions. This suggests that with increased cleaning, the carbonaceous shell on the Pt nanoparticles becomes tighter and tighter in O_2; however, it can continue to open in H_2 allowing access to the Pt. In fact, the ethylene hydrogenation rate after UV cleaning is slightly greater than expected based on the geometric surface area of the Pt as determined by TEM. This suggests that the carbonaceous fragments have almost no site blocking effect in H_2.

Figure 4.6(B) shows the corresponding C and N surface concentrations as a function of UV cleaning time measured by XPS. After 30 min, the concentration of N is below the limit of detection by XPS. The C concentration also levels off after 30 min to a steady value representing only 10 % of the initial C. Again it is impossible to distinguish if this C is a decomposition product of the PVP or if it is contamination of the cleaned Pt surface.

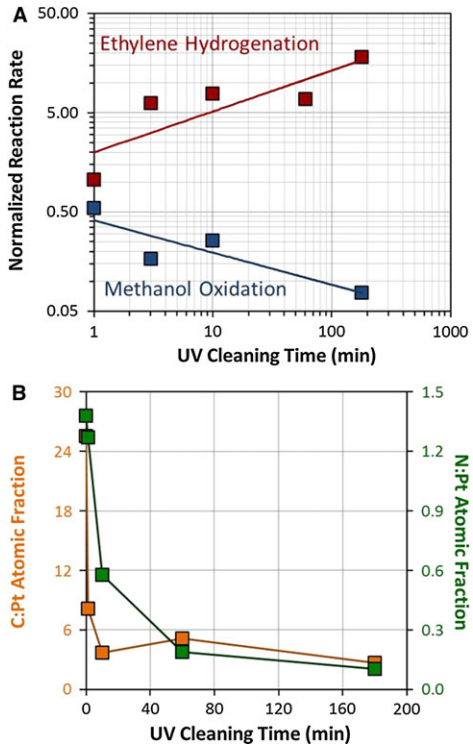

Figure 4.6: (A) Reaction rates as a function of UV cleaning time for ethylene hydrogenation and methanol oxidation. The reaction rates are normalized to the initial rate for each reaction before UV cleaning. The results show that the rates of the two reactions continue to diverge with

increased cleaning time, eventually showing a 200-fold difference in activity. (B) C:Pt and N:Pt atomic fractions measured by XPS as a function of UV cleaning time. The N concentration on the surface drops below the limit of detection after 30 min of UV cleaning. The C concentration on the surface also levels off at a value representing only 10 % of the initial C from the PVP capping layer.

To determine if the formation of this carbonaceous shell is a general phenomenon, we synthesized Pt nanoparticles using an alternate method where the capping agent is added after synthesis. This allowed us to add different capping agents to identical nanoparticle aliquots to isolate the cap as the sole variable between two nanoparticle samples. For this experiment, PVP and OA were used as capping agents in two separate aliquots, and the activity of these catalysts were monitored for ethylene hydrogenation and methanol oxidation before and after cleaning. In this case, thermal oxidation in a tube furnace was used for cap removal rather than UV cleaning. The OA-capped nanoparticles were cleaned at 473 K, and the PVP-capped nanoparticles were cleaned at 573 K. This temperature for PVP removal is consistent with previous work on the thermal degradation of Pt–PVP complexes.[33] Following cleaning the PVP- and OA-capped nanoparticles showed a 100-fold and 30-fold increased activity for ethylene hydrogenation, respectively.

Figure 4.7 shows the effect of cap removal on the activity for methanol oxidation. In this figure, the methanol oxidation rate for each catalyst is represented as a turnover frequency normalized to the number of Pt active sites determined by ethylene hydrogenation.[23] Consequently, each bar shows the methanol oxidation rate relative to the ethylene hydrogenation rate on the same

catalyst. Data is shown for all three types of nanoparticles studied (i.e., UV-cleaned Pt–PVP, thermally-cleaned Pt–PVP, and thermally-cleaned Pt–OA). Noting that this graph is on a log-scale, the Pt activity for methanol oxidation is shown to decrease for each catalyst by a factor of between 50 and 250 following cap removal. Because these values are normalized to the catalyst activity for ethylene hydrogenation, this cannot be the result of nanoparticle agglomeration. It seems clear that for methanol oxidation, the capped nanoparticles are dramatically more active than their cleaned analogues, and this finding applies to multiple capping agents and cleaning methods.

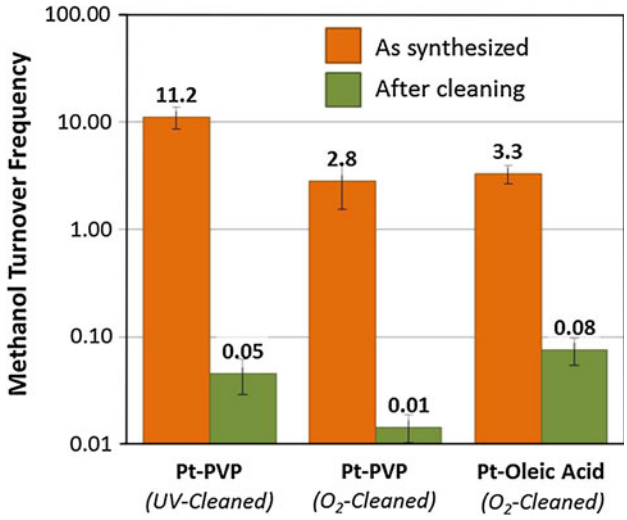

Figure 4.7: Methanol oxidation turnover frequency (TOF) for Pt nanoparticle catalysts before and after cap removal. TOF is given as the number of methanol molecules converted per Pt site per s. The number of platinum sites was determined from the measured rate of ethylene hydrogenation using a known TOF. Consequently, each bar shows the methanol oxidation rate relative to the ethylene hydrogenation rate on the same catalyst. Data is shown for all three types of nanoparticles studied (i.e., UV-cleaned Pt–PVP, thermally-cleaned Pt–PVP, and thermally-

cleaned Pt–OA). Noting that this graph is on a log-scale, the Pt activity for methanol oxidation is shown to decrease for each catalyst by a factor of between 50 and 250 following cap removal.

4.4 Conclusions

We studied the catalytic activity of PVP- and OA-capped Pt nanoparticles for ethylene hydrogenation and methanol oxidation before and after cap removal. We find that the capped nanoparticles are active for both reactions showing that the organic coating does not prevent nanoparticle catalysis. However, the cleaned nanoparticles are only active for ethylene hydrogenation. The rate of ethylene hydrogenation is substantially higher on the cleaned particles relative to the capped particles, but the rate of methanol oxidation decreases to nearly zero following cap removal either by UV light or by thermal oxidation.

SFG shows that, following cleaning treatments, carbonaceous fragments are still present on the nanoparticles. These carbonaceous fragments are dynamic and reversibly restructure in alternating H_2 and O_2 atmospheres. It appears that a carbonaceous shell forms on the uncapped Pt nanoparticles that is tightly closed in O_2 but becomes permeable in H_2. Using cyclohexene as a probe molecule, we show that following UV cleaning, reactant molecules can only access the Pt when H_2 is present to open the carbonaceous shell.

These results demonstrate the important role of an organic cap to mediate the catalytic properties of nanoparticles. We find that the presence of an organic cap does not prevent catalysis. In fact, for methanol oxidation the capped nanoparticles are more than 10 times more active than their cleaned analogues. Accordingly, the capping agent on colloidal nanoparticles represents a well-controlled passivation layer which does not prevent catalysis under reaction conditions. That this coating may improve catalytic performance for certain reactions argues that the capping agent is

a dynamic component of the active catalyst which consists of both a metal nanoparticle and an organic coating.

4.5 References

1. Ertl G, Knozinger H, Weitkamp J (eds) (1999) Preparation of solid catalysts. Wiley, Weinheim
2. Tsoncheva T, Dal Santo V, Gallo A, Scotti N, Dimitrov M, Kovacheva D (2011) Appl Catal A Gen 406:13
3. Strongin DR, Carrazza J, Bare SR, Somorjai GA (1987) J Catal 103:213
4. McCrea KR, Parker JS, Somorjai GA (2002) J Phys Chem B 106:10854
5. Andersson MP, Abild-Pedersen E, Remediakis IN, Bligaard T, Jones G, Engbwk J, Lytken O, Horch S, Nielsen JH, Sehested J, Rostrup-Nielsen JR, Norskov JK, Chorkendorff I (2008) J Catal 255:6
6. Kliewer CJ, Bieri M, Somorjai GA (2009) J Am Chem Soc 131:9958
7. Ahmadi TS, Wang ZL, Green TC, Henglein A, El-Sayed MA (1924) Science 1996:272
8. Peng X, Wickham J, Alivisatos AP (1998) J Am Chem Soc 120:5343
9. Puntes VF, Krishnan KM, Alivisatos AP (2001) Science 291:2115
10. Oh M, Mirkin CA (2005) Nature 438:651
11. Yin Y, Alivisatos AP (2005) Nature 437:664
12. Song H, Kim F, Connor S, Somorjai GA, Yang P (2004) J Phys Chem B 109:188
13. Rioux RM, Song H, Hoefelmeyer JD, Yang P, Somorjai GA (2004) J Phys Chem B 109:2192
14. Song H, Rioux RM, Hoefelmeyer JD, Komor R, Niesz K, Grass M, Yang P, Somorjai GA (2006) J Am Chem Soc 128:3027
15. Bratlie KM, Lee H, Komvopoulos K, Yang P, Somorjai GA (2007) Nano Lett 7:3097
16. Kuhn JN, Huang W, Tsung C-K, Zhang Y, Somorjai GA (2008) J Am Chem Soc 130:14026
17. Grass M, Rioux R, Somorjai G (2009) Catal Lett 128:1
18. Grass ME, Joo SH, Zhang Y, Somorjai GA (2009) J Phys Chem C 113:8616
19. Kliewer CJ, Aliaga C, Bieri M, Huang W, Tsung C-K, Wood JB, Komvopoulos K, Somorjai GA (2010) J Am Chem Soc 132:13088
20. Witham CA, Huang W, Tsung C-K, Kuhn JN, Somorjai GA, Toste FD (2010) Nat Chem 2:36
21. Alayoglu S, Aliaga C, Sprung C, Somorjai G (2011) Catal Lett 141:914
22. Zhang Y, Grass ME, Kuhn JN, Tao F, Habas SE, Huang W, Yang P, Somorjai GA (2008) J Am Chem Soc 130:5868
23. Kuhn JN, Tsung C-K, Huang W, Somorjai GA (2009) J Catal 265:209
24. Albiter MA, Crooks RM, Zaera F (2009) J Phys Chem Lett 1:38
25. Lu J, Fu B, Kung MC, Xiao G, Elam JW, Kung HH, Stair PC (2012) Science 335:1205
26. Gorin DJ, Sherry BD, Toste FD (2008) Chem Rev 108:3351
27. Li Y, Liu JH-C, Witham CA, Huang W, Marcus MA, Fakra SC, Alayoglu P, Zhu Z, Thompson CM, Arjun A, Lee K, Gross E, Toste FD, Somorjai GA (2011) J Am Chem Soc 133:13527

28. Mitsudome T, Mikami Y, Matoba M, Mizugaki T, Jitsukawa K, Kaneda K (2012) Angew Chem Int Ed 51:136
29. Bratlie KM, Komvopoulos K, Somorjai GA (2008) J Phys Chem C 112:11865
30. Aliaga C, Park JY, Yamada Y, Lee HS, Tsung C-K, Yang P, Somorjai GA (2009) J Phys Chem C 113:6150
31. Shen YR (2003) The principles of nonlinear optics. Wiley-Interscience, Hoboken
32. Krier JM, Michalak WD, Baker LR, An K, Komvopoulos K, Somorjai GA (2012) J Phys Chem C 116:17540
33. Borodko Y, Habas SE, Koebel M, Yang P, Frei H, Somorjai GA (2006) J Phys Chem B 110:23052
34. Yang M, Chou KC, Somorjai GA (2003) J Phys Chem B 107:5267

Chapter 5: Structure Sensitivity in Pt Nanoparticle Catalysts for Hydrogenation of 1,3-Butadiene: *In Situ* Study of Reaction Intermediates Using SFG Vibrational Spectroscopy

5.1 Introduction

Catalysts that promote selective hydrogenation of unsaturated hydrocarbons to mono-olefins, while inhibiting full hydrogenation, are important to the chemical industry. Active hydrogenation catalysts like Pt, however, convert 1,3-butadiene (1,3-BD, a prototype diene) into four primary products: three partial hydrogenation products (1-butene, trans-2-butene, and cis-2-butene) and one full hydrogenation product (n-butane). Partial hydrogenation products are produced at 65–90% with the remainder being n-butane.[1-4] Experimental studies using metallic single crystals,[1, 2, 4, 5] metal particles supported on metal oxides,[3, 6] and DFT-based theoretical approaches[7-9] have been used to understand the factors that control the product distribution. One interpretation of the behavior is ascribed to the different adsorption energies of 1,3-BD and the butenes.[9] In this case, butenes readsorb and participate in secondary reactions to form n-butane. An alternative interpretation that is based on theoretical work suggests that a metallocycle reaction intermediate is responsible for this behavior.[8] The DFT results suggest that the full hydrogenation product observed on Pt can be attributed to a particular C_4H_8 metallocycle intermediate, which is relatively stable and evolves into n-butane. The activation barrier for the formation of the metallocycle intermediate on Pt was comparable to the activation barriers that lead to the formation of the butene products. Thus, n-butane is believed to form simultaneously with the butenes. The results presented in this paper show that Pt nanoparticles catalyze the formation of n-butane and the partial hydrogenation products simultaneously through parallel pathways that initiate with different radical intermediates.

Studies using single crystals have shown that the crystal face affects adsorbate stability and transition state geometries on the surface.[10] For example, different distributions of benzene and cyclohexane are produced from cyclohexene hydrogenation at constant temperature on Pt(100) and Pt(111) surfaces because of the differences in stability of 1,3-cyclohexadiene and 1,4-cyclohexadiene reaction intermediates.[11] Product distribution is also affected by the size of metal nanoparticle catalysts, which produce different geometric and electronic effects.[5, 12-16] Geometric effects include the distribution of kinks, steps, and terrace sites exposed on the catalyst surface, whereas electronic effects include variations in the d-band center and width and the electronic screening effects that the adsorbate experiences as the ratio of surface atoms to bulk atoms approaches one. Studies using colloidally prepared Pt metal nanoparticles have demonstrated that the product distribution can vary significantly in the 1–10 nm size range where the electronic and geometric factors play a role (e.g., refs 17−19).

The objective of this study was to examine the size effect of Pt nanoparticle catalysts on the product distribution during hydrogenation of 1,3-BD. We show that monodisperse ensembles of polyhedral Pt nanoparticle catalysts with 0.9 and 1.8 nm average diameter exhibit changes in selectivity for n-butane and 1-butene as compared to Pt nanoparticles of 4.6 or 6.7 nm average diameter. Molecular-level studies were performed with the system under reaction conditions with *in situ* sum frequency generation (SFG) vibrational spectroscopy, which exclusively probes adsorbed intermediates. We perform SFG on nanoparticle catalysts with ligand capping agents intact so that sintering is avoided and the particle size is maintained.

5.2 Experimental Section

Materials. Hexachloroplatinic acid ($H_2PtCl_6 \cdot 6H_2O$, 99%), poly(vinylpyrrolidone) (PVP, MW = 29 000 amu), ethylene glycol (reagent grade), HCl (2 M), 1,3-butadiene (99%), and NaOH (99.9%) were manufactured by Sigma-Aldrich. Hydrogen (5.0 UHP), helium (5.0 UHP), and Ar (5.0 UHP) were purchased from Praxair. Polished silicon (100) wafers were purchased from Addison Engineering.

Nanoparticle Synthesis. Polyhedral platinum nanoparticles of average diameter in the range of 0.9–7 nm were prepared using polyol methods described in the literature,[19] with PVP capping ligands to prevent aggregation. Details of the syntheses are given in the Supporting Information. The nanoparticles were separated from the postsynthesis colloidal suspension by precipitation with acetone and centrifugation at 4000 rpm (VWR, Clinical 50) for 5 min. Further washing with ethanol and hexane was performed up to seven times to remove residual molecular fragments from the particle surface. The nanoparticles were stored in ethanol under refrigeration until their use in kinetic and spectroscopic studies.

Langmuir–Blodgett Film Deposition. For both kinetic and spectroscopic studies, the nanoparticles were supported on a silica surface because it is an inert, low acidity surface that guarantees negligible activity. The use of a two-dimensional support differs from common catalytic studies that use high surface area materials (e.g., silica, alumina, or carbon) as catalyst supports. We cannot use the high surface area three-dimensional supports because SFG spectroscopy requires that incoming and outgoing photons are in direct line-of-sight with molecules adsorbed on the surface of the catalyst and photodetector, respectively. Pt

nanoparticles were deposited onto a silicon wafer (Si(100)) that was prepared with 5000 Å thick thermal oxide layer (kinetic studies) or a fused silica prism (spectroscopic studies) using a Langmuir–Blodgett (LB) trough (Kibron, MTX). Before nanoparticle deposition, the silica surfaces were exposed to strong oxidizers (e.g., piranha or NoChromix) to remove organic residues and make them hydrophilic (oxidizers hydroxylate the silica). Nanoparticles were dispersed in chloroform and deposited onto an ultrapure water subphase (18.2 MΩ·cm). Following the evaporation of chloroform and equilibration of particles (30–60 min), the two-dimensional layer of particles was compressed at a rate of 10 mm/min to create a close-packed monolayer. When the monolayer of particles was compressed to a surface pressure in the range of 30–35 mN/m, the substrates were withdrawn at a rate of 2 mm/min while at constant pressure. Surface tension was monitored using a Wilhelmy probe made of a PtIr wire.

Materials Characterization. Nanoparticle morphology and size were examined using a transmission electron microscope (TEM, JEOL 200CX) operated at 120 kV. The images shown in Figure 5.1 demonstrate the morphology and size of nanoparticles with an average diameter of 0.94 ± 0.26, 1.80 ± 0.34, 4.63 ± 1.12, and 6.67 ± 1.20 nm. The monodispersity of the nanoparticles is demonstrated by the nanoparticle size distributions shown in Figure 5.1e, which were obtained with >300 particles using ImageJ software.

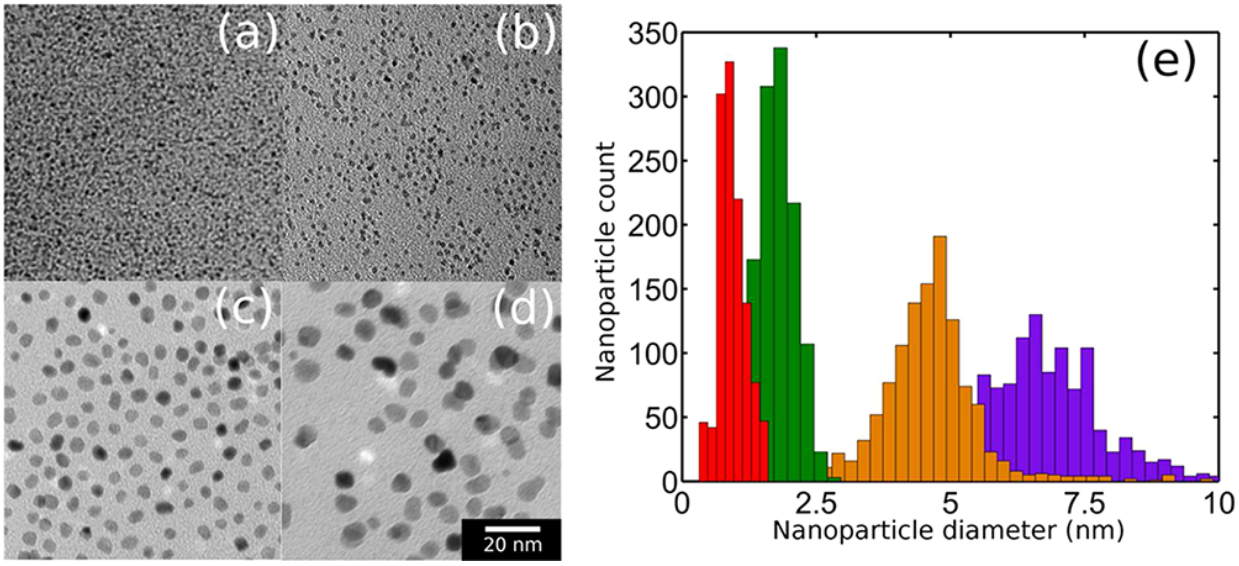

Figure 5.1: Transmission electron microscopy images of polyhedral Pt nanoparticles. Panels a, b, c, and d show nanoparticles with an average diameter and standard deviation of 0.94 ± 0.26, 1.80 ± 0.34, 4.63 ± 1.12, and 6.67 ± 1.20 nm, respectively. Panel e shows particle size distributions for the four particle sizes. The 20 nm scale bar in panel d reflects the scale for all images.

Kinetic Measurements. Hydrogenation reactions were performed in a 1 L stainless steel chamber equipped with a capacitance manometer pressure gauge (MKS Baratron), a metal bellows recirculating pump (Senior Aerospace MB-21), a turbomolecular pump (Pfeiffer), and a mechanical rotary pump. Conflat flanges with Cu gaskets were used to seal the reaction chamber. The temperature of the sample was maintained by resistively heating a boronitride ceramic plate (Momentive) and monitored using a type K thermocouple. The conversion of 1,3-butadiene to 1-butene, cis-2-butene, trans-2-butene, and n-butane was monitored using a gas chromatograph (Shimadzu GC-17A, Agilent Plot Alumina "S" capillary column (0.2 mm × 30 m)) equipped with a flame ionization detector. Prior to each reaction, the chamber was evacuated using the

turbomolecular pump. The gate valve to the pumps was closed prior to introducing the reactant species. Selectivities were calculated by comparing the rate of accumulation for each species at a conversion of 1,3-BD of <10%. Blank experiments in the absence of Pt nanoparticles indicated negligible background activity.

Sum Frequency Generation Vibrational Spectroscopy. Details regarding the theory of SFG can be found elsewhere.[20-22] Briefly, SFG vibrational spectroscopy relies on a nonlinear optical phenomenon that occurs when two pulsed laser beams—with visible and infrared frequencies—overlap. The selection rules for SFG activity maintain that the excited molecular resonance is in an asymmetric environment (i.e., an interface), and the molecules have a net polar orientation. The first requirement indicates that the SFG process can only occur in a medium without centrosymmetry (i.e., an interface). Thus, neither the Pt nanoparticle bulk nor the gas phase mixture will yield spectroscopic signatures and only the z-component of molecules at an interface will produce a SFG signal. The second requirement indicates that no photon emission is detected from species arranged in an equal number of opposite orientations on a surface or from a completely disordered surface structure.[22] Therefore, the SFG intensity is a function of both the concentration of interfacial species and their orientation.

SFG vibrational spectroscopy was performed with a mode-locked Nd:YAG dye laser (Continuum D-20) with 1064 nm fundamental output, 20 Hz repetition rate, and 20 ps pulse width. A frequency-doubling crystal was used to generate a visible (532 nm) beam from the fundamental beam. An optical parametric generator/amplifier produced tunable infrared in the 2680–3180 cm^{-1} range, corresponding to the stretching modes of aliphatic and aromatic groups.

Visible and infrared beams of 130 μJ power were spatially and temporally overlapped at the base of a polished fused silica equilateral (60°) prism (ISP Optics) at angles of 63° and 48°, respectively, from the surface normal to achieve total internal reflection. All of the experiments were performed in ppp polarization combination. SFG photons were detected by a photomultiplier tube with a gated boxcar integrator.

In situ SFG spectroscopy experiments were performed by mounting the optical prism onto a batch reactor as described previously.[23] Nanoparticles directly deposited onto the prism using the LB trough were simultaneously exposed to the gas phase mixture and the visible and IR evanescent waves, which were produced by total internal reflection. We ensured a closed environment by sealing the prism/reactor interface with a Kalrez O-ring. The reaction temperature and gas pressures were identical to the kinetic studies with the exception that the inert gas was Ar instead of He.

Quantitative analysis of the relative peak intensities in SFG spectroscopy requires an understanding of the IR and Raman transitions of the molecules on the surface and the interferences between the nonresonant and resonant contributions. The SFG intensity, I_{SFG}, can be described by

$$I_{\mathrm{SFG}} \propto \left| \chi_{\mathrm{NR}}^{(2)} \mathrm{e}^{i\varphi_{\mathrm{NR}}} + \sum_{\nu} \left(\frac{A_\nu \mathrm{e}^{i\delta_\nu}}{\omega_\nu - \omega_{\mathrm{IR}} + i\Gamma_\nu} \right) \right|^2 I_{\mathrm{vis}} I_{\mathrm{IR}} \qquad (1)$$

where I_{vis} and I_{IR} are the intensities of the incident visible and infrared photons, respectively, and $\chi_{NR}^{(2)}$ and φ_{NR} are the magnitude and phase change (relative to the incident beam) of the nonresonant susceptibility, respectively. The term in eq 1 with the summation equals the

resonant susceptibility ($\chi_R^{(2)}$) corresponding to the vth vibrational mode; A_v, ω_v, δ_v, and Γ_{v-1} are the magnitude, frequency, phase change, and the relaxation time of the vibrationally excited state involved in vibrational resonance, respectively.[22] For analysis of the SFG spectra as a function of nanoparticle size, the SFG spectra were decomposed according to eq 1, and the quantity used for the evaluation of the intensity, I_v, is given by

$$I_v = \int_{-\infty}^{\infty} \left| \frac{A_v}{\omega_v - \omega_{\mathrm{IR}} + i\Gamma_v} \right|^2 \mathrm{d}\omega_{\mathrm{IR}} = \frac{{A_v}^2}{\Gamma_v} \tag{2}$$

as performed in a previous study.[24] Because the net intensity of the SFG spectra varies on different nanoparticles, we normalize by the sum of all measured intensities ($\hat{I}_v = I_v \sum_i I_{v_i}$) when comparing spectra from Pt nanoparticles of different sizes.

Curve fitting was performed with Matlab using a constrained sequential quadratic programming optimization algorithm (fmincon)[25] in conjunction with a multistart framework to find the global minimum (globalsearch).[26] Prior to performing the fitting routine, I_{SFG} was normalized by a factor equal to the average over the IR intensities entering the prism and leaving the prism (as a function of ω_{IR}). During the fitting routine, the phase terms, φ_{NR} and δ_v, were constrained to values between $-\pi$ and π, while the remaining terms in eq 1 were constrained to positive values.

Detecting Reaction Intermediates in the Presence of PVP Capping via H_2-Induced Disordering. Catalysts prepared by colloidal synthesis techniques use organic ligand molecules to "cap" the nanoparticles. The capping agent prevents agglomeration during synthesis and under reaction conditions when the nanoparticles are exposed to high temperatures.[27] Separating the signal of the reaction intermediates from the signal of the capping agent can be challenging.

However, we recently demonstrated that for PVP-capped Pt nanoparticles the presence of gas-phase H_2 disorders PVP and reduces its signal intensity.[28] An example of SFG spectra demonstrating this behavior is shown in Figure S.5.1 (Supporting Information). With the SFG signal from PVP significantly reduced, the signal from the reaction intermediates during 1,3-BD hydrogenation was detected without interference from the capping material.

5.3 Results

Hydrogenation of 1,3-butadiene (1,3-BD) was performed on ensembles of Pt nanoparticle catalysts with average diameters equal to 0.94, 1.80, 4.63, and 6.67 nm. The reaction was performed at a constant temperature of 75 °C using a reactant gas mixture composed of 10 Torr of 1,3-BD, 100 Torr of H_2, and 650 Torr of inert gas (He and Ar for kinetic and spectroscopic studies, respectively). Reaction intermediates were measured under reaction conditions using SFG spectroscopy. We correlate the kinetic and spectroscopic results with the theoretical results obtained by Sautet and co-workers.[7-9] Following is a brief description of their predicted reaction intermediates.

Predicted Reaction Intermediates of 1,3-Butadiene Hydrogenation. Hydrogenation of 1,3-BD (C_4H_6) is a chemical reaction that includes the formation of a C_4H_7, C_4H_8, C_4H_9, and C_4H_{10} species through the stepwise addition of H atoms (Figure 5.2). According to DFT-based computational studies of Sautet and co-workers,[7-9] there are six stable reaction intermediates for 1,3-BD on Pt(111). The most stable chemisorbed structure of 1,3-BD on Pt is a tetra-σ binding geometry. Addition of the first H atom to a terminal carbon (C_1 or C_4) of a tetra-σ intermediate produces the 2-buten-1-yl radical (2B1R) and H-addition to an internal carbon (C_2 or C_3)

produces the 1-buten-4-yl radical (1B4R). The nomenclature used here follows the IUPAC conventions for gas-phase radicals as practiced by Valcarcel et al.:[8] the first number accounts for the position of the "remaining" double bond, and the second number(s) accounts for the position of the radical C atom(s). The intermediates discussed here are not actually radicals but are strongly bound closed-shell complexes; the terminology is used only for classification purposes. The 1B4R has three σ-bonds at the C_1, C_2, and C_4 atoms. The 2B1R is a methylallyl that has one σ-bond with Pt at the C_1 atom and one π-bond with a Pt atom shared across the C_2 and C_3 atoms.

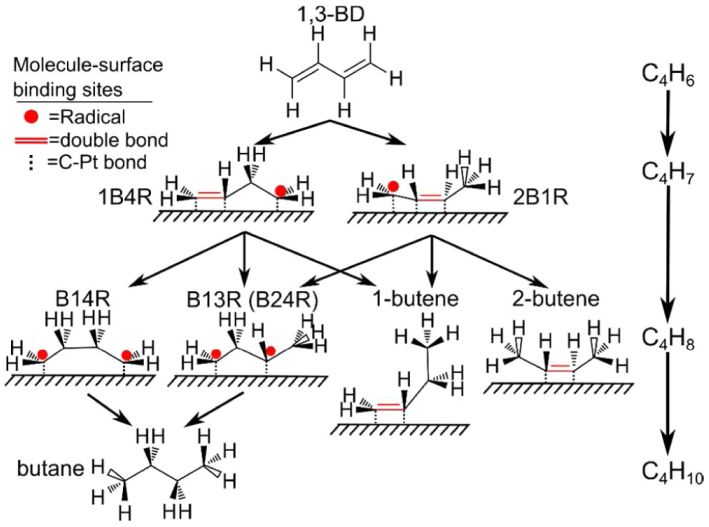

Figure 5.2: Schematic of reaction pathways for 1,3-butadiene (1,3-BD) hydrogenation, DFT-predicted stable intermediates during hydrogenation, and observed products. Addition of the first H atom leads to 1-buten-4-yl radical (1B4R) or 2-buten-1-yl radical (2B1R); addition of a second H atom leads to butan-1,4-diyl radical (B14R), butan-1,3-diyl radical (B13R) or butan-2,4-diyl (B24R) intermediates, or 1-butene (1B) and 2-butene (2B) products. The nomenclature corresponds to IUPAC gas-phase radicals, in which an "R" designates a radical. Carbon radicals and double bonds that are highlighted in red designate their locations in the gas phase, which correspond to the locations of C–Pt bonds that are shown by dotted lines. The reaction intermediates shown are based on the DFT predictions of Valcarcel et al.[8]

For each C_6H_7 species, there are three possibilities to add a second H atom. H-addition to 1B4R at the C_1 atom produces a butan-2,4-diyl radical (B24R), the C_2 atom produces a butan-1,4-diyl radical (B14R), and the C_4 atom produces 1-butene. H-addition to 2B1R at the C_1 atom produces 2-butene, the C_2 atom produces a butan-1,3-diyl radical (B13R), and the C_3 atom produces 1-butene. The B13R and B24R are equivalent species even though they are obtained through different pathways. Only the B14R or B13R (or B24R) species can directly lead to n-butane from 1,3-BD via addition of two additional H atoms. The stable gas-phase products include three C_4H_8 species (1-butene, cis-2-butene, and trans-2-butene) and one C_4H_{10} species (n-butane).

Role of Nanoparticle Size for 1,3-Butadiene Hydrogenation. Figure 5.3 shows the number of molecules of 1,3-BD converted over the Pt catalysts and the number of produced molecules of n-butane, 1-butene, trans-2-butene, and cis-2-butene produced versus total 1,3-BD conversion for different nanoparticle sizes. All four species were produced, and no C–C coupling or C–C scission products were observed regardless of nanoparticle size. The formation rates of n-butane and 1-butene are nearly equal at low conversion for both 0.9 and 1.8 nm Pt nanoparticles; however, the larger size nanoparticles (4.6 and 6.7 nm) exhibit the preferential formation of 1-butene. When 1,3-BD reaches 75% conversion, the concentration of 1-butene in the batch reactor stops increasing and then decreases due to a secondary reaction to n-butane for all size nanoparticles. This behavior indicates that in the presence of excess 1,3-BD the 1-butene or 2-butene does not competitively readsorb. In all cases, trans-2-butene and cis-2-butene are minor products and are formed at a rate that is independent of 1,3-BD concentration.

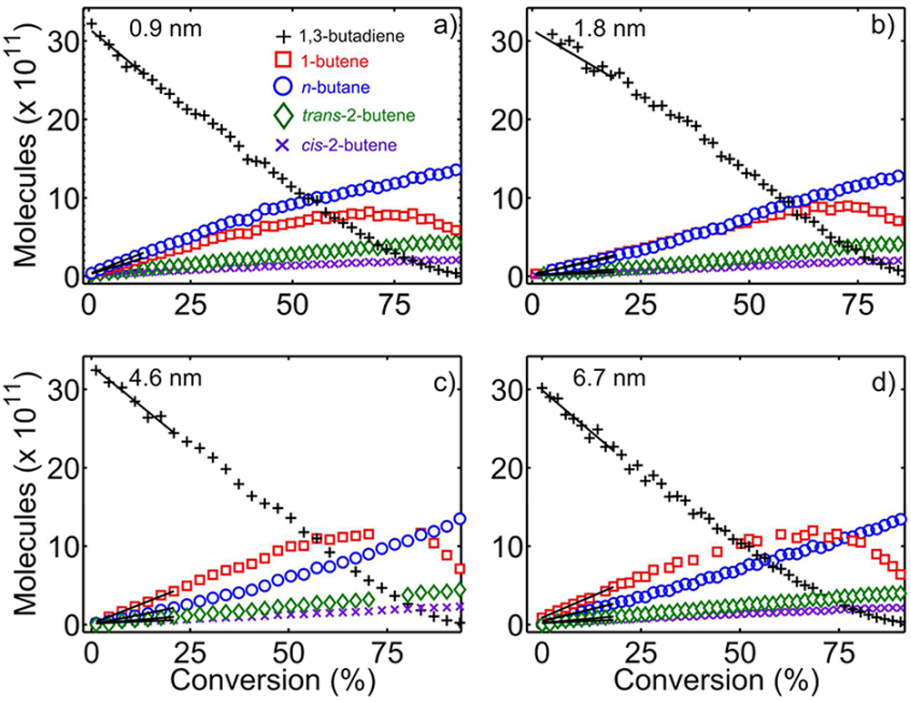

Figure 5.3: Number of molecules versus percent conversion for (+) 1,3-butadiene hydrogenation (T = 75 °C, 10 Torr of 1,3-BD, 100 Torr of H_2, 650 Torr of He) over ensembles of Pt nanoparticles with average diameters of (a) 0.9, (b) 1.8, (c) 4.6, and (d) 6.7 nm. The products include 1-butene, n-butane, trans-2-butene, and cis-2-butene. Black lines indicate the linear regions that are used to calculate the selectivity.

Product selectivity to the four products was calculated using the ratio of formation rates at conversion below 10% (black lines in Figure 5.3). Figure 5.4 shows the product selectivity distributions with ensembles of Pt nanoparticle catalysts of different sizes. The dashed lines are used to indicate trends. Pt nanoparticle catalysts with an average diameter of 6.7 nm yielded 80% butenes (partial hydrogenation) and 20% n-butane (full hydrogenation). The distribution of butenes was also split 80:20 for 1-butene versus 2-butene with trans- and cis-2-butene contributing 15% and 5% to the total. The product distribution observed for the 6.7 nm particles

was similar to that observed on bulk Pt single crystals ((111) and (100)) and foils in the temperature range 25–125 °C.[2, 4] In these former studies, the butenes were produced with 60–87% selectivity and a distribution of 1-butene and 2-butenes in ratios of 70–80% and 30–20%, respectively. Pt nanoparticle catalysts with an average particle diameter of 4.6 nm yield a partial to full hydrogenation product ratio that remains similar to the 6.7 nm particles (80:20). Pt nanoparticles with an average particle size of 1.8 and 0.9 nm yield a partial to full hydrogenation product ratio of 40:60 and 47:53, respectively. This corresponds to a net decrease of 30% for the butenes from 6.7 to 0.9 nm nanoparticle ensembles. As the particle size decreases, the ratio of 2-butene gives a slight preference to trans-2-butene, yet the change is insignificant. Thus, the increase in n-butane production with decreasing nanoparticle size occurred at the expense of 1-butene.

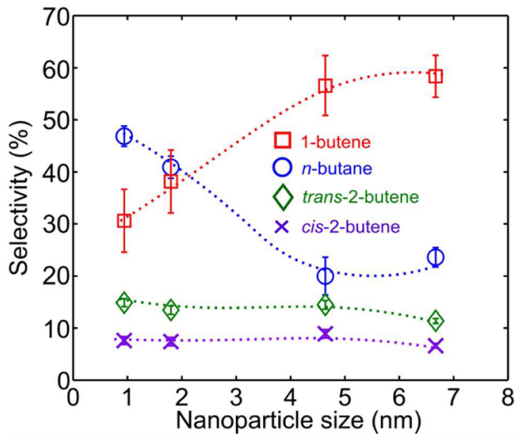

Figure 5.4: Product selectivity for 1-butene, n-butane, trans-2-butene, and cis-2-butene from the conversion of 1,3 butadiene (1,3-BD) hydrogenation (T = 75 °C with 10 Torr of 1,3-BD, 100 Torr of H_2, and 650 Torr of He) as a function of nanoparticle size.

The similar selectivity of the 6.7 nm particles with those of the bulk measurements suggests that the capping agent (PVP) does not play a role in the catalytic process. To further confirm the

negligible role of PVP, we performed UV-treatment of the nanoparticles under ambient atmosphere for 1 h. This treatment has been shown to effectively degrade PVP.[23, 28] The product distribution of the treated particles to n-butane, 1-butene, trans-2-butene, and cis-2-butene was 23%, 58%, 11%, and 6%, respectively. The similar selectivity between the treated and untreated 6.7 nm nanoparticles (only the latter are shown in 5.4) confirms that PVP ligands do not participate in the catalytic reaction.

Kinetic results for the hydrogenation of 1,3-BD on Pt nanoparticles confirm that the product selectivity is indeed structure sensitive, that is, nanoparticle size dependent. The general trend was an increased selectivity to full hydrogenation products as the size of nanoparticle ensembles decreased, accompanied by a slight increase in trans-2-butene production. The kinetic selectivity trend suggests that there is an inherent difference in the reaction pathways for 1,3-BD hydrogenation on Pt nanoparticles of various sizes. To elucidate the observed selectivity differences, we use *in situ* SFG vibrational spectroscopy to monitor the stable reaction intermediates with different size nanoparticles.

***In Situ* Detection of the Reaction Intermediates in 1,3-Butadiene Hydrogenation by SFG Vibrational Spectroscopy.** SFG vibrational spectroscopy is a surface specific technique that exclusively probes molecules at interfaces. The interface specificity provides a means to probe the most stable, or long-lived, intermediate(s) adsorbed on a catalyst's surface under reaction conditions without interference from gas phase molecules. We used *in situ* SFG during 1,3-BD hydrogenation at a constant temperature of 75 °C and a reactant gas mixture composed of 10 Torr of 1,3-BD, 100 Torr of H_2, and 650 Torr of Ar. To determine whether the changes in

reaction selectivity on Pt nanoparticle catalysts correspond to alternate reaction pathways, we measured the aliphatic region of the vibrational spectrum to probe the methyl, methylene, methylidyne, and vinylic groups of stable reaction intermediates. The aliphatic region of the vibrational spectrum for linear hydrocarbons is complicated by the variety of conformers and reaction pathways that exist due to the rotational degrees of freedom accompanying the C–C bond. Moreover, all unsaturated and partially saturated intermediates present on the Pt surface during 1,3-BD hydrogenation comprise methyl, methylene, methylidyne, or vinylic groups. Therefore, an understanding of the possible reaction intermediates, associated reaction pathways, and the vibrational resonances that are expected from those intermediates is essential to the interpretation of the SFG results. In addition, correctly assessing the *in situ* SFG results requires an understanding that intermediates with the longest lifetime dominate the SFG signal regardless of whether they are spectator species or reactive intermediates. To determine whether the SFG signal arises from spectator or reactive species, the SFG signal was collected upon exposing the surface to the reaction mixture followed by evacuation of the reaction chamber and reintroduction of H_2. If the signal rapidly returned to the baseline spectra observed initially, the *in situ* SFG signal was attributed to reactive species.

Previous SFG studies regarding the adsorption structures of ethylene,[29, 30] propylene,[31] isobutene,[32] n-hexane, 2-methylpentane, 3-methylpentane, and 1-hexene on Pt(111)[21] and Pt(100),[33] methylfuran and dimethylfuran on Pt nanoparticles,[23] reflection–absorption infrared spectroscopy (RAIRS) studies on a series of n-alkanes (n = 3–10),[34, 35] and in particular C_4 hydrocarbons[36] provide a reference for band assignments of the aliphatic vibrations. SFG and RAIRS are complementary because both techniques follow the metal surface selection rule that

requires the transition dipole vector of a vibrational mode to have components normal to the surface to be active. Note that SFG also requires that a vibrational mode induces a change in the polarizability of a molecule (Raman-active), and therefore, RAIRS and SFG are not identical. Depending on the particular adsorbate configuration, methyl, methylene, and methylidyne groups will have unique SFG-active vibrational resonances. Methyl or methylene groups that are oriented away from the surface exhibit modes similar to the condensed phase stretches: symmetric methylene (CH_2(s)) and methyl (CH_3(s)) bands appear at about 2850 and 2875 cm^{-1}; asymmetric methylene (CH_2(a)) and methyl (CH_3(a)) bands appear at about 2935 and 2970 cm^{-1}; symmetric and asymmetric vinylic methylene bands (=CH_2(s) and =CH_2(a)) appear at about 2990 and 3085 cm^{-1}, respectively; and the tertiary methylidyne C–H band appears at 2910 cm^{-1}. When methylene or methyl groups are in the proximity of a metal surface (e.g., flat-lying adsorbate), their vibrational modes are perturbed as a consequence of charge transfer from the metal surface. The perturbation results in a red-shift and a band broadening from the condensed phase values.[36] Furthermore, the H–metal surface interaction is believed to force the vibrational modes of the atoms pointing toward the surface (down) and pointing away from the surface (up) to decouple. On Pt(111), perturbed (p) methylene bands, with H pointing toward (CH_2(p,down)) and away (CH_2(p,up)) from the surface appear at about 2670–2700 and 2900 cm^{-1}, respectively; perturbed methyl bands with H down (CH_3(p,down)) and pointing up (CH_3(p,up)) appear at about 2800–2820 and 2930–2945 cm^{-1}, respectively.[34]

The *in situ* SFG vibrational spectra of the stable reaction intermediates present during 1,3-BD hydrogenation are shown in Figure 5.5. Blue circles and dashed red lines are the average and standard deviation over nine SFG spectra, while solid black lines represent the best-fit model

spectra. Comparison of the SFG spectra shown in Figure 5.5 suggests that the stable intermediates on the 0.9 and 1.8 nm particles (designated as small) are similar under reaction conditions, whereas, the spectra of the 4.6 and 6.7 nm particles (designated as large) are similar but differ from those of the small particles. The small particles exhibit at least four visually apparent bands, whereas the large particles exhibit only one. The overall shape of the SFG spectra is dependent, in part, on the magnitude of each band and their phase relations. Unlike Raman and infrared vibrational spectroscopies, the magnitude of a peak is not linearly correlated with the concentration of the vibrationally active species. The nonlinear interaction between the resonant susceptibilities of each band, as well as with the nonresonant susceptibility, can give rise to constructive and destructive interference, which can augment and diminish bands. These factors can make the experimental SFG spectrum visually deceptive. We address the contributions of each band to the SFG spectra using eq 1 as a model and by optimizing over the set of parameters to provide an accurate description of the surface chemistry.

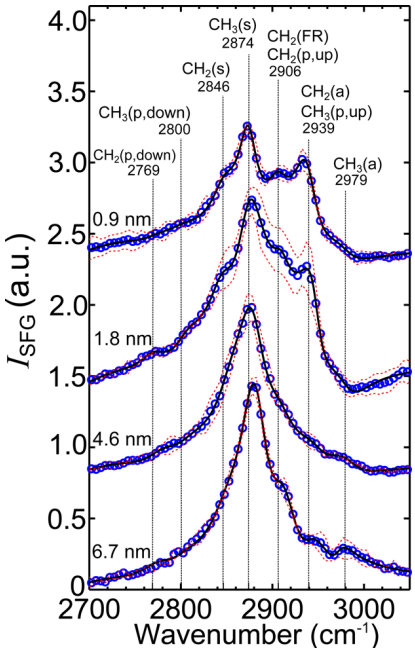

Figure 5.5: *In situ* SFG vibrational spectra of reaction intermediates produced on 0.9, 1.8, 4.6, and 6.7 nm Pt nanoparticle catalysts during 1,3-BD hydrogenation (T = 75 °C with 10 Torr of 1,3-BD, 100 Torr of H_2, and 650 Torr of Ar). Blue dots and red dashed lines represent averages and standard deviations of nine SFG spectra, respectively, while black lines represent optimized model SFG spectra using eq 1. Assignments of vibrational bands are based on model spectra (more than one mode is assigned in the case of resonances with similar peak locations). CH_2(s) and CH_2(a) modes appear at 2846 and 2939 cm^{-1}, while CH_3(s) and CH_3(a) modes appear at 2874 and 2979 cm^{-1}, respectively. Perturbed modes (p), reflecting C–H···Pt interactions appear for methyl and methylene groups. Perturbation causes a decoupling of the H atoms near the surface (down) and the H atoms pointing away from the surface (up). CH_2(p,up) and CH_2(p,down) appear at 2939 and 2769 cm^{-1}, while CH_3(p,up) and CH_3(p,down) appear at 2939 and 2800 cm^{-1}, respectively. Vibrational resonances below 2850 and above 2940 cm^{-1} are not visually apparent but are required to fit the spectra. In particular, an out-of-phase CH_3(a) mode is required to fit the

wavenumber region above 2940 cm^{-1}. Best-fit parameters for each model are given in Table S.5.1 (Supporting Information).

SFG Vibrational Spectra of 1,3-Butadiene Reaction Intermediates Observed on 0.9 and 1.8 nm Pt Nanoparticle Catalysts. The top two SFG spectra in Figure 5.5 correspond to the stable reaction intermediates of 1,3-BD hydrogenation over ensembles of small (0.9 and 1.8 nm) Pt nanoparticles. The vibrational band with the largest visually apparent magnitude at 2874 cm^{-1} is assigned to a CH_3(s) stretch. This band indicates that one or more of the stable reaction intermediates is bound in a standing-up, or partially standing, geometry. For example, butylidyne adsorbs with one C–Pt bond in a completely standing-up geometry, whereas 1-butene adsorbs in a partially standing geometry with di-σ bonds on the C_1 and C_2 atoms and the C_3–C_4 bond normal to the surface.[36] The other band with a clearly defined peak at 2939 cm^{-1} can be assigned to either a CH_2(a) on a C_2 (or C_3) internal atom or a CH_3(p,up) resonance on a C_1 (or C_4) terminal atom.[21, 34, 36] The CH_2(a) resonance originates from a C_2 or C_3 atom of a flat-lying intermediate such as a metallocycle, which is formed after a C atom detaches from the Pt surface following β-hydrogenation. We do not assign the CH_2(a) resonance to the C_3 atom of an adsorbed 1-butene because this methylene is equatorial, and the transition dipole vector is expected to have a negligible z-component. Internal methylene groups oriented in a standing geometry are also unlikely because one tenet of SFG activity is that the susceptibility tensor vanishes if C–H groups are arranged centrosymmetrically. This occurs, for example, when internal CH_2 groups of a hydrocarbon chain are arranged in an all-trans conformation, which is the stable conformation of a standing chain.[24] Given these reasons, the CH_2(a) originates from either the 1B4R, B14R, or B13R metallocycle intermediates.

The CH_3(p,up) stretch is also indicative of a semiflat-lying adsorbate that has a terminal methyl group.[34] In these configurations, the terminal methyl has H-stretches with parallel and perpendicular vector components with respect to the surface. An adsorbate with a di-σ binding geometry, in which the C_2–C_3 atoms are attached to Pt (i.e., adsorbed 2-butene), or a π-allyl binding geometry that has a C_1–Pt σ-bond and C_2–C_3–Pt π-bond, will exhibit this resonance. These configurations are representative of the B13R and 2B1R adsorbed intermediates, respectively. Because each scenario is possible, we assign the band at 2939 cm^{-1} to a combination of CH_2(a) and CH_3(p,up) modes. We did not include two unique feature designations because there was insufficient spectral resolution to accurately assign peak locations with confidence.

Two other bands are visually apparent in the SFG spectra of the catalysts with 0.9 and 1.8 nm Pt nanoparticle catalysts. The shoulder at 2846 cm^{-1} at wavenumbers below the CH_3(s) is assigned to a CH_2(s) stretching mode. This resonance originates from an interior methylene (C_2 or C_3) group of a flat-lying intermediate, as described for the CH_2(a) stretch. The presence of the CH_2(s) mode, in contrast to a perturbed mode, suggests that at least one stable reaction intermediate has H atoms oriented away from the surface. The feature located between the CH_3(s) and CH_2(a)/CH_3(p,up) at 2906 cm^{-1} can be assigned to three possible modes or a combination thereof: a Fermi resonance (FR) that arises from the first overtone of the C–H bend of a methylene group and a fundamental methylene stretching mode (CH_2(FR)), a perturbed methylene stretch for the atom pointing away from the surface (CH_2(p,up)), or a tertiary C–H stretching mode.[21, 34] We discount the possible influence of a tertiary C–H stretch because this

stretch is likely equatorial. The negligible SFG activity of the tertiary C–H was demonstrated by Cremer et al., who compared the SFG vibrational signature of propylene and partially deuterated propylene (CD_3CHCH_2) adsorbed on Pt(111).[31] No peaks above 2900 cm^{-1} were observed using the deuterated species. However, both CH_2(FR) and CH_2(p,up) modes were identified in the RAIRS and SFG spectra of linear alkanes adsorbed on Pt(111).[21, 34, 37]

The four bands at 2846, 2874, 2906, and 2939 cm^{-1} constitute the primary, visually identifiable, spectral features of the SFG spectra for the ensembles of small nanoparticle catalysts. These are the primary bands used to correlate the observed reaction intermediates with nanoparticle size. Each band and their assigned origins are summarized in Table 5.1. The optimized best-fit A_v, ω_v, δ_v, and Γ_v parameters, for each of these bands, are shown in Table S.5.1 (Supporting Information). With only these four modes, we were unable to develop a model that yielded a satisfactory fit to the experimental SFG spectra. The primary discrepancy between the model—using only these four bands—and the experimental data was the representation of the leading and tailing regions from 2700–2850 and 2940–3100 cm^{-1}. The line shape of $\chi_{R,q}^{(2)}$ is comparable to a Lorenztian.[22] A Lorentzian profile features leading and tailing edges that exhibit convex shapes, whereas the SFG spectral profiles shown for the ensembles of small nanoparticle catalysts do not. This suggests that the experimental data must have contributing resonant or nonresonant terms that exhibit constructive or destructive interference in the leading and tailing regions. Because the conclusions from this study are not based on these additional features, their presentation is given in the Supporting Information. In summary, we predict additional features at 2680, 2769, 2800, and 2979 cm^{-1} (the feature at 2680 cm–1 is not shown in Figure 5.5). We

assign the two features at 2680 and 2769 cm^{-1} to CH_2(p,down) modes and the features at 2800 and 2979 cm^{-1} to CH_3(p,down) and CH_3(a) modes, respectively.

location (cm^{-1})	band assignment	location (cm^{-1})	band assignment
2680	CH_2(p,down)[21,33,34,36]	2874	CH_3(s)[11,21,24,28.29−36]
2769	CH_2(p,down)[21,33,34,36]	2906	CH_2(FR)/CH_2(p,up)[21,34,37]
2800	CH_3(p,down)[21,33,34,36]	2939	CH_2(a)/CH_3(p,up)[21,34,36]
2846	CH_2(s)[11,21,24,28,29−36]	2979	CH_3(a)[11,21,24,28,29−36]

Table 5.1: Summary of band wssignments for the *in situ* SFG performed in the presence of 10 Torr of 1,3-Butadiene, 100 Torr of H_2, and 650 Torr of Ar at 75 °C.

SFG Vibrational Spectra of 1,3-Butadiene Reaction Intermediates Observed on 4.6 and 6.7 nm Pt Nanoparticle Catalysts. The bottom two SFG spectra in Figure 5.5 correspond to the stable intermediates of 1,3-BD hydrogenation on the ensembles of large (4.6 and 6.7 nm) Pt nanoparticle catalysts. These spectra exhibit a single dominant feature at 2878 cm^{-1} (shifted 4 cm–1 in comparison to the spectra for the small nanoparticle catalysts). We assign this feature to a CH_3(s) as specified with the small particles. However, unlike the SFG spectra for the small particles, there are no other well-resolved features in the spectra. While shoulders at 2910, 2939, and 2979 cm^{-1} are present in the spectrum for the 6.7 nm particles, the spectra for the 4.6 nm particles appears as a single broad profile. A broad spectrum can be attributed to inhomogeneous broadening that is a consequence of many local environments of the adsorbate, temperature-induced broadening, and similar resonances that come from different adsorbed intermediates.[21, 33, 34] However, if we use a single feature to model the SFG spectra shown for the 4.6 and 6.7 nm particles, the full width half-maximum ($2\Gamma_v$) approximately equals 120 cm^{-1}, or a value of Γ_v = 60 cm^{-1}. Fundamental vibrations and perturbed modes have values in the ranges 10–20 and 25–40 cm^{-1}, respectively.[21, 24] Therefore, a single CH_3(s) feature is physically unreasonable. To fit the SFG spectra for the 4.6 and 6.7 nm Pt nanoparticle catalysts, we constrained $\omega_v \pm 10$ cm^{-1}

from the optimal values of the 1.8 nm SFG spectra and allowed A_v, δ_v, and Γ_v to vary with the same bounds used previously. The best-fit model spectra for the 4.6 and 6.7 nm Pt nanoparticles comprise the same features as the best-fit model spectra for the 0.9 and 1.8 nm Pt nanoparticles. On the basis of the models, we predict that the next most influential features in the SFG spectra after the dominant feature at 2878 cm^{-1} are located at 2906 and 2979 cm^{-1}, corresponding to the CH_2(FR)/CH_2(p,up) and CH_3(a) resonances, respectively.

5.4 Discussion

The combination of kinetic selectivity measurements and *in situ* vibrational spectroscopy provides a unique perspective into the reaction pathways of 1,3-BD hydrogenation on monodisperse ensembles of Pt nanoparticle catalysts. Because of the nature of the SFG selection rules, the vibrational resonances that we observed are entirely due to the intermediates on the surface. The vibrational resonances can directly be correlated to the reactive intermediates and not spectrator species. We confirmed this by evacuating the reaction chamber and changing the reactor gas mixture to H_2/Ar immediately following the *in situ* measurement. The SFG signal completely reversed to the baseline measurement prior to performing the 1,3-BD hydrogenation reaction (not shown). We also confirmed that the SFG signal under reaction conditions was not related to the 1,3-BD-induced reordering of the PVP by exposing the catalysts to deuterated 1,3-BD and D_2 (not shown). After confirming that D_2 disorders the PVP in the same manner as H_2, deuterated 1,3-BD exposed to the Pt nanoparticle catalysts showed negligible change in SFG signal. This is expected because methyl and methylene stretches of deuterated species are red-shifted to the range of 1900–2200 cm^{-1}.

Clear trends emerge from the kinetic selectivity and spectroscopy results. The ensembles of small nanoparticle catalysts produce more n-butane and trans-2-butene at the expense of total butenes and cis-2-butene, respectively, and the SFG signal originating from CH_2 resonances dramatically increases while the CH_3 resonances decrease. Figure 5.6 shows the correspondence between the methyl (CH_3) and methylene (CH_2) vibrational bands and the likely adsorbed intermediates. Three of the proposed intermediates (1B4R, B13R, and B14R) will exhibit SFG-active CH_2 resonances, while four of the proposed intermediates (2B1R, B13R, 1-butene, and 2-butene) will exhibit SFG-active CH_3 resonances. SFG-active CH_3 resonances can also arise from a butan-2-yl or butan-1-yl species (a butan-2-yl is produced by H-addition to the C_1 atom of 1-butene, 2-butene, or B13R; a butan-1-yl radical is produced by H-addition to the C_2 atom of 1-butene or B13R); both of these intermediates are bound by a single σ-bond and are not expected to have a long lifetime on the surface of Pt in the presence of 1,3-BD.

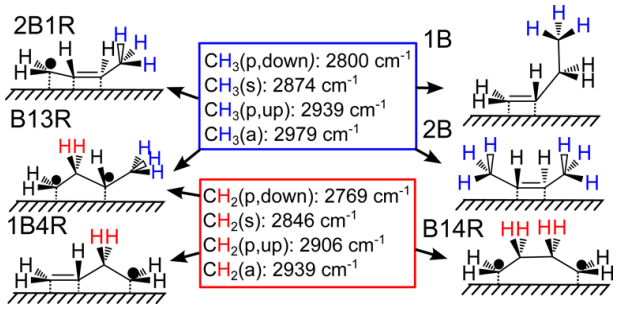

Figure 5.6: Six reaction intermediates produce SFG active methylene (red H) and methyl (blue H) vibrational stretches. Intermediates are designated using the IUPAC nomenclature with an "R" indicating a radical: 2-buten-1-yl (2B1R), butan-1,3-diyl (B13R), 1-butene (1B), and 2-butene (2B) produce bands associated with methyl resonances; B13R, 1-buten-4-yl (1B4R), and butan-1,4-diyl (B14R) produce bands associated with methylene resonances. The C–Pt bonds are located at the radical (•) and double bonded carbons. The methyl and methylene vibrations are designated with an s, a, p, up and down for symmetric, asymmetric, perturbed, away from the

surface, and toward the surface, respectively. Note that n-butane can only originate from the B13R, 1B4R, or B14R intermediates (i.e., species with CH_2 vibrations).

The changes in the normalized SFG intensity ($\hat{I}_v$, eq 2) of CH_2(a)/CH_3(p,up) and CH_3(s) resonances at 2939 and 2874 cm^{-1}, respectively, versus Pt nanoparticle size are shown in Figure 5.7a. The SFG spectra on the 0.9 and 1.8 nm nanoparticles exhibit a large proportion of signal originating from the CH_2(a)/CH_3(p,up) vibrational bands. The 4.3 and 6.7 nm particles; however, have little signal originating from the CH_2(a)/CH_3(p,up) band. SFG intensities for the remaining resonances are given in Table S.5.2 (Supporting Information). The reduced integral area of the CH_3(s) feature in Figure 5.7a for the small nanoparticles, despite the feature's apparent peak height in the SFG spectra, can be rationalized by the increased integral area of the two features located on either side of the CH_3(s) feature. SFG intensity is not simply a superposition of areas; instead, constructive interference of bands magnifies the combination of features by additional nonlinear terms. In contrast, the CH_2(a)/CH_3(p,up) feature is on the edge of the spectral profile. Note that $\hat{I}_v$ is a function of orientation/order and concentration. Therefore, we cannot directly correlate these vibrational signatures to a quantitative assessment of the reaction intermediates. This qualitative assessment can, however, correlate the likely reaction intermediates and reaction pathways with nanoparticle size.

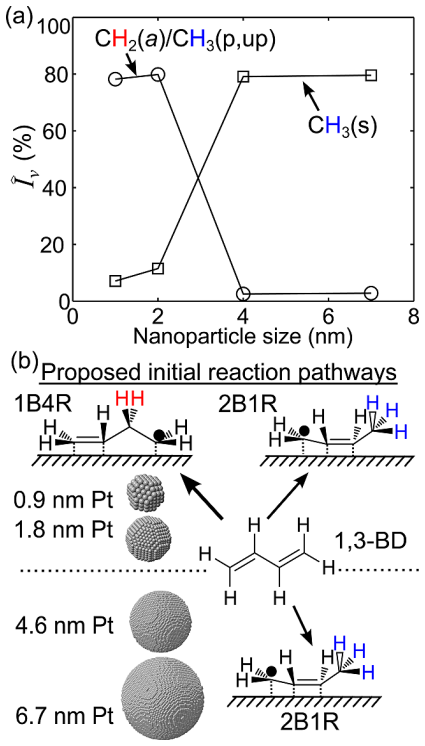

Figure 5.7: Normalized SFG intensity ($\hat{I}_v$, eq 2) for the CH_2(a)/CH_3(p,up) (o) and CH_3(s) (□) vibrational modes as a function of nanoparticle size. $\hat{I}_v$ is a function of orientation/order and concentration. Small nanoparticles have an increased contribution to the SFG signal from the CH_2(a)/CH_3(p,up) modes, whereas large particles are dominated by the CH_3(s) mode. The proposed initial reaction pathways for the 0.9 and 1.8 nm Pt nanoparticles (above dotted line) and 4.6 and 6.7 nm Pt nanoparticles (below dotted line) are shown below. The methylene and methyl groups that exhibit SFG signal are highlighted in red and blue. The small nanoparticles exhibit methylene (CH_2) stretches that indicate the presence of the 1B4R intermediate. This pathway leads to n-butane. The pathway starting with 2B1R leads predominately to butenes.

In view of Figure 5.7a and the DFT predictions[7-9] discussed previously, we infer from the magnitude of the CH_3(s) band that 1,3-BD hydrogenation on the large particles favors the 2B1R pathway. Even though the activation barrier from 1,3-BD to 2B1R and 1,3-BD to 1B4R was

proposed to be nearly equal, 2B1R is more thermodynamically stable on Pt(111) by 17 kJ/mol.[8] Moreover, the reaction pathway through the π-bonded intermediate is considered to be orders of magnitude more rapid than on the di-σ bonded counterpart during ethylene and propylene hydrogenation[14, 29, 31] and H-addition to a terminal carbon was shown to be three times more favorable than an internal carbon.[38] Therefore, we attribute the CH_3(s) mode at 2874 cm^{-1} to the 2B1R intermediate. The 2B1R intermediate will also produce a CH_3(a) mode and perturbed variations (as discussed in the Supporting Information) but will not yield any CH_2 activity. We assign the CH_2 resonance activity at 2846, 2906, and 2939 cm^{-1} (determined via the model) to the 1B4R and/or B13R intermediate(s). Both of these intermediates are along the pathway to n-butane. From a thermodynamic perspective of the adsorbates on a Pt(111) surface, the active CH_2 modes could be attributed to the 1B4R intermediate, which is predicted to be 6 kJ/mol more stable than the B13R;[8] however, from a kinetic perspective, the second hydrogenation step from the 2B1R to B13R is more favorable than the pathway from 1B4R to B13R. Thus, the n-butane formed on the large particles (and Pt bulk surfaces) corresponds to the pathway through the B13R intermediate. The low CH_2 band intensity observed on the large particles correlates with the low selectivity to n-butane. The low intensity may also suggest that the B13R intermediate does not have a long lifetime on the surface. In contrast to the large nanoparticles, we cannot use the Pt(111)-based DFT energetics to argue plausible reaction intermediates for the small nanoparticle catalysts. However, we rationalize the 30% increase in n-butane selectivity based on the same set of reaction intermediates.

The increase in CH_2 resonances (i.e., bands at 2846, 2906, and 2939 cm^{-1}) confirms that the ensembles of small nanoparticle catalysts provide favorable pathways to n-butane. The decline in

the production of 1-butene is not due to further hydrogenation of 1-butene on the surface, since the reaction was performed under excess 1,3-BD, as discussed previously. Instead, plausible explanations arise from changes in the potential energy pathways on the surface, which comprise of a destabilized 2B1R intermediate, a stabilized 1B4R intermediate, a stabilized B13R intermediate, a destabilized transition state between the 1B4R and B13R intermediates, or a destabilized transition state between the 2B1R and B13R intermediates (cf. 5. 1). The decrease in CH_3 vibrational bands (Figure 5.7a) and the fact that selectivity toward 2-butenes changes only slightly indicates that the change is not due to a destabilized 2B1R intermediate. A decreased surface lifetime of the 2B1R species at the expense of a stabilized B13R intermediate (change in quasi-equilibrium) would not necessarily change the concentration of CH_3 vibrational modes but simply provide additional CH_2 modes, which is not consistent with trends shown in Figure 5.7a. It is well-known that small nanoparticles exhibit an increase in edge/step and corner sites at the expense of terrace sites.[10, 39] Reduced atomic coordination results in an improved molecule–particle chemical interaction via shifts in the d-band center toward the Fermi level, which increases the number of empty antibonding states. Moreover, a higher d-band center makes the surface more reactive by lowering the transition state energies.[13, 16, 40, 41] The presence of low-coordination sites will alter the stability of metallocycle binding geometries (like 1B4R and B13R) and transition states by reducing strain of the geometric configuration that would not be stable on a terrace.[39, 42] This would suggest that the presence of low-coordination sites promotes the pathway proceeding via H-insertion at the internal carbon, which leads to the metallocycle 1B4R. Thus, we believe that the observed CH_2 signal originates from the 1B4R species.

5.5 Conclusion

Understanding how to control the reaction pathways that lead to different product distributions is critical to rational design of heterogeneous catalysts. We have shown using colloidally synthesized monodisperse nanoparticle distributions that the size of Pt nanoparticle catalysts impacts the product distribution in 1,3-butadiene hydrogenation. Two parallel reaction pathways lead to the full and partial hydrogenation products and the nanoparticle size impacts the kinetic preference toward each pathway. Ensembles of Pt nanoparticle catalysts of 0.9 and 1.8 nm promote a 30 and 20% increase in the full hydrogenation (n-butane) of 1,3-butadiene, respectively, in comparison to 4.6 and 6.7 nm Pt catalysts. Formation of n-butane occurs at the expense of 1-butene rather than 2-butene products. *In situ* SFG vibrational spectroscopy was used to monitor the adsorbed reaction intermediates on Pt nanoparticles with the capping ligand intact, under working conditions identical to those of the kinetic experiments. The results indicate that the 0.9 and 1.8 nm Pt catalysts provide adsorption sites (e.g., low coordination sites) that facilitate H-insertion at an internal carbon (1B4R), in addition to H-insertion at the terminal carbon (2B1R), whereas the 4.6 and 6.7 nm Pt catalysts favor H-insertion at the terminal carbon as observed on Pt bulk materials.

5.6 References

(1) Oudar, J.; Pinol, S.; Pradier, C. M.; Berthier, Y. *J. Catal.* **1987**, *107*, 445.
(2) Pradier, C. M.; Margot, E.; Berthier, Y.; Oudar, *J. Appl. Catal.* **1988**, *43*, 177.
(3) Primet, M.; Elazhar, M.; Guenin, M. *Appl. Catal.* **1990**, *58*, 241.
(4) Yoon, C. H.; Yang, M. X.; Somorjai, G. A. *Catal. Lett.* **1997**, *46*, 37.
(5) Massardier, J.; Bertolini, J. C.; Ruiz, P.; Delichere, P. *J. Catal.* **1988**, *112*, 21.
(6) Sarkany, A.; Stefler, G.; Hightower, J. W. *Appl. Catal., A* **1995**, *127*, 77.
(7) Delbecq, F.; Loffreda, D.; Sautet, P. *J. Phys. Chem. Lett.* **2010**, *1*, 323.
(8) Valcarcel, A.; Clotet, A.; Ricart, J. M.; Delbecq, F.; Sautet, P. *J. Phys. Chem. B* **2005**, *109*, 14175.
(9) Vigne, F.; Haubrich, J.; Loffreda, D.; Sautet, P.; Delbecq, F. *J. Catal.* **2010**, *275*, 129.
(10) Somorjai, G. A. *Introduction to Surface Chemistry and Catalysis*, 2nd ed.; Wiley: Hoboken, NJ, 2010.

(11) McCrea, K. R.; Somorjai, G. A. *J. Mol. Catal A: Chem.* **2000**, *163*, 43.
(12) Hammer, B.; Nielsen, O. H.; Norskov, J. K. *Catal. Lett.* **1997**, *46*, 31.
(13) Norskov, J. K.; Abild-Pedersen, F.; Studt, F.; Bligaard, T. *Proc. Natl. Acad. Sci. U. S. A.* **2011**, *108*, 937.
(14) Zaera, F. *Appl. Catal., A* **2002**, *229*, 75.
(15) Singh, U. K.; Vannice, M. A. *Appl. Catal., A* **2001**, *213*, 1.
(16) Kleis, J.; Greeley, J.; Romero, N. A.; Morozov, V. A.; Falsig, H.; Larsen, A. H.; Lu, J.; Mortensen, J. J.; Dulak, M.; Thygesen, K. S.; Norskov, J. K.; Jacobsen, K. W. *Catal. Lett.* **2011**, *141*, 1067.
(17) Alayoglu, S.; Aliaga, C.; Sprung, C.; Somorjai, G. A. *Catal. Lett.* **2011**, *141*, 914.
(18) Pushkarev, V.; Musselwhite, N.; An, K.; Alayoglu, S.; Somorjai, G. A. *Nano Lett.* **2012**, *12*, 5196.
(19) Rioux, R. M.; Song, H.; Hoefelmeyer, J. D.; Yang, P.; Somorjai, G. A. *J. Phys. Chem. B* **2005**, *109*, 2192.
(20) Shen, Y. R. *The Principles of Nonlinear Optics*; Wiley: New York, 1984.
(21) Yang, M. C.; Chou, K. C.; Somorjai, G. A. *J. Phys. Chem. B* **2004**, *108*, 14766.
(22) Lambert, A. G.; Davies, P. B.; Neivandt, D. *J. Appl. Spectrosc. Rev.* **2005**, *40*, 103.
(23) Aliaga, C.; Tsung, C. K.; Alayoglu, S.; Komvopoulos, K.; Yang, P. D.; Somorjai, G. A. *J. Phys. Chem. C* **2011**, *115*, 8104.
(25) Fletcher, R.; Powell, M. J. D. *Comput. J.* **1963**, *6*, 163.
(26) Ugray, Z.; Lasdon, L.; Plummer, J.; Glover, F.; Kelly, J.; Marti, R. *Informs J Comput* **2007**, *19*, 328.
(27) Somorjai, G. A.; Park, J. Y. *Angew. Chem., Int. Ed.* **2008**, *47*, 9212.
(28) Krier, J. M.; Michalak, W. D.; Baker, L. R.; An, K.; Komvopoulos, K.; Somorjai, G. A. *J. Phys. Chem. C* **2012**, *116*, 17540.
(29) Cremer, P.; Stanners, C.; Niemantsverdriet, J. W.; Shen, Y. R.; Somorjai, G. *Surf. Sci.* **1995**, *328*, 111.
(30) Cremer, P. S.; Su, X. C.; Shen, Y. R.; Somorjai, G. A. *J. Am. Chem. Soc.* **1996**, *118*, 2942.
(31) Cremer, P. S.; Su, X. C.; Shen, Y. R.; Somorjai, G. A. *J. Phys. Chem.* **1996**, *100*, 16302.
(32) Cremer, P. S.; Su, X. C.; Shen, Y. R.; Somorjai, G. *J. Chem. Soc., Faraday Trans.* **1996**, *92*, 4717.
(33) Bratlie, K. M.; Somorjai, G. A. J. Phys. Chem. C 2007, 111, 6837.
(34) Manner, W. L.; Bishop, A. R.; Girolami, G. S.; Nuzzo, R. G. *J. Phys. Chem. B* **1998**, *102*, 8816.
(35) Chesters, M. A.; Gardner, P.; Mccash, E. M. *Surf. Sci.* **1989**, *209*, 89.
(36) Lee, K.; Zaera, F. *J. Phys. Chem. B* **2005**, *109*, 2745.
(37) Wang, H. F.; Gan, W.; Lu, R.; Rao, Y.; Wu, B. H. *Int. Rev. Phys. Chem.* **2005**, *24*, 191.
(38) Klein, R.; Scheer, M. D.; Waller, J. G. *J. Phys. Chem.* **1960**, *64*, 1247.
(39) Coq, B.; Figueras, F. Coord. Chem. Rev. 1998, 178, 1753. (40) Kitchin, J. R.; Norskov, J. K.; Barteau, M. A.; Chen, J. G. *Phys. Rev. Lett.* **2004**, *93*, 046101.
(41) Schnur, S.; Gross, A. *Phys. Rev. B* **2010**, *81*, 033402.
(42) Hammer, B.; Norskov, J. K. *Adv. Catal.* **2000**, *45*, 71.
(43) Fosser, K. A.; Kang, J. H.; Nuzzo, R. G.; Woll, C. *J. Chem. Phys.* **2007**, *126*, 194707.
(44) Yamamoto, M.; Sakurai, Y.; Hosoi, Y.; Ishii, H.; Ito, E.; Kajikawa, K.; Ouchi, Y.; Seki, K. *Surf. Sci.* **1999**, *427−28*, 388.

Supplement to Chapter 5

Experimental Information

0.9 nm Pt nanoparticle synthesis

The 0.9 nm particles were prepared by heating 5 mL of a 0.5 M solution of NaOH (0.1 g) at 160 °C n a 50 mL round bottom flask until dissolved. A solution of 80 mg of $H_2PtCl_6 \cdot 6H_2O$ (1.95×10^{-4} mols) in 5 mL of ethylene glycol was added to the flask. The flask was sealed with septa and the residual air atmosphere was evacuated by three cycles of vacuum pumping followed by an Ar purge. The synthesis was conducted at 160 °C with vigorous stirring for 2 hrs. After the colloid returned to room temperature, 2 mL of 2 M HCl was added with stirring until the solution was neutralized. The particles were precipitated in a centrifuge (VWR Clinical 50, 4000 rpm) for 10 min. After adding 0.1 g of PVP and 40 mL of acetone, the PVP-capped particles were centrifuged and redispersed in 20 mL ethanol. The nanoparticles are stable in the ethylene glycol reaction solution for many months.

1.8 nm Pt nanoparticle synthesis

The 1.8 nm particles were prepared by combining 10 mL of ethylene glycol, 100 mg of $H_2PtCl_6 \cdot 6H_2O$ (1.9 × 10–4 mols) and 5 mL of a 0.5 M NaOH solution (0.1 g) in a 25 mL three-neck round bottom flask. The flask was sealed with septa and the residual air atmosphere was evacuated by three cycles of vacuum pumping followed by an Ar purge. The synthesis was conducted at 160 °C with vigorous stirring in Ar flow for 3 hrs. After the colloid returned to room temperature, 20.3 mg of PVP (0.18 mols) was added followed by vigorous stirring for 20 min. Finally, 100 mL of acetone was added to the solution and the particles were precipitated by

centrifugation (VWR Clinical 50, 4000 rpm) for ~10 min.

4.6 nm Pt nanoparticle synthesis

The 4.6 nm particles were prepared by combining 20 mL of ethylene glycol, 100 mg of $H_2PtCl_6 \cdot 6H_2O$ (1.9×10^{-4} mols) and 440 mg of PVP (4×10^{-3} mols) in a 50 mL three-neck round bottom flask. The flask was sealed with septa and the residual air atmosphere was evacuated by three cycles of vacuum pumping followed by an Ar purge. The synthesis was conducted at 165 °C with vigorous stirring in Ar flow for 25 min. Continuing the reaction for longer times does not change the size of the particles. When the solution returned to room temperature, 100 mL of acetone was added to the solution and the particles were precipitated by centrifugation (VWR Clinical 50, 4000 rpm) for ~10 min. The particles (black precipitate) were then redispersed in ethanol.

7 nm Pt nanoparticle synthesis

The 7 nm particles were prepared by heating 2.5 mL of ethylene glycol in a three neck round-bottom flask equipped with a reflux condenser at 200 °C. Sequential additions of ~0.2 mL of a 0.062 M solution of $H_2PtCl_6 \cdot 6H_2O$ (1.9×10^{-4} mols) in ethylene glycol and 0.375 mL of a 0.33 M solution of PVP in ethylene glycol were added alternately every 30 s over the course of 16 min using syringes (total 97 mg of $H_2PtCl_6 \cdot 6\ H_2O$ and 222.3 mg of PVP). The solution was allowed to ripen for an additional 10 min. When the solution returned to room temperature, 100 mL of acetone was added to the solution and the particles were precipitated by centrifugation (VWR Clinical 50, 4000 rpm) for ~10 min. The particles (black precipitate) were then redispersed in ethanol.

Nanoparticle washing

Nanoparticles were subjected to 'cleaning' steps following synthesis. The cleaning procedure comprised of repeated precipitation, dispersion, and sonication. Particles were precipitated by the addition of hexane at a hexane to ethanol volume ratio of 5:1 and centrifugation for 5 min. The black precipitate was redispersed in ethanol under sonication. Sonication was continued for at least 5 min following redispersion. This procedure was repeated seven times.

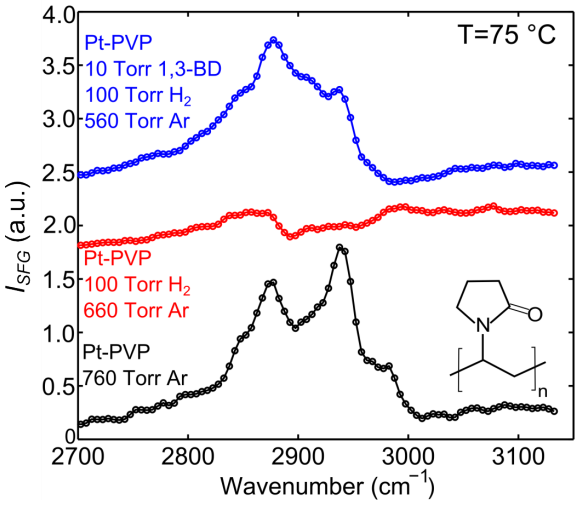

Figure S.5.1: SFG spectra of an ensemble of 2 nm Pt nanoparticles capped with PVP exposed to different atmospheres at 75 °C. The three spectra correspond to Pt nanoparticles exposed to 760 Torr of Ar (black), 100 Torr H_2 and 660 Torr Ar (red), and 10 Torr 1,3-butadiene (1,3-BD), 100 Torr H_2, and 550 Torr Ar (blue).

Table S.5.1: Fitting Parameters for SFG spectra shown in Figure 5.

Peak		Average nanoparticle diameter (nm)			
		0.9	1.8	4.6	6.7
Non-resonant contribution	χ_{NR}	0.36	0.54	0.33	0.22
	φ_{NR}	2.43	2.07	2.82	2.42
CH_2(p,down)	A	4.47	5.06	5.00	5.00
	ω	2680.07	2680.00	2680.50	2680.50
	Γ	27.66	27.04	24.98	24.98
	δ	0.70	0.01	0.55	0.55
CH_2(p,down)	A	0.52	1.38	2.06	2.06
	ω	2769.41	2768.86	2771.14	2771.14
	Γ	18.31	16.89	22.20	22.20
	δ	2.40	3.25	2.59	2.59
CH_3(p,down)	A	0.65	2.27	1.03	1.03
	ω	2800.19	2802.59	2803.38	2803.38
	Γ	19.97	19.78	19.72	19.72
	δ	3.53	2.50	2.17	2.17
CH_2(s)	A	3.24	4.17	2.85	2.85
	ω	2846.50	2845.18	2850.73	2850.73
	Γ	17.10	18.24	20.00	20.00
	δ	4.15	3.78	3.59	3.59
CH_3(s)	A	4.95	9.60	10.60	16.45
	ω	2873.97	2873.78	2878.98	2882.17
	Γ	12.07	18.52	18.74	19.00
	δ	4.85	3.61	5.01	4.07
CH_2(FR)/CH_2(p,up)	A	2.35	1.59	2.88	8.26
	ω	2906.45	2909.98	2910.00	2910.00
	Γ	12.95	12.15	18.40	19.00
	δ	5.46	4.72	5.36	3.65
CH_2(a)/CH_3(p,up)	A	18.19	20.22	2.54	3.61
	ω	2939.85	2946.69	2949.63	2939.56
	Γ	14.80	12.84	19.00	16.99
	δ	0.92	0.71	0.31	2.85
CH_3(a)	A	7.09	7.47	3.82	1.53
	ω	2979.39	2981.53	2983.71	2971.67
	Γ	21.00	21.00	20.28	11.46
	δ	5.20	5.58	6.24	2.78

Table S.5.2: Normalized Intensities for SFG bands from the spectra shown in Figure 5.

Peak	$I_v / \sum_i I_{v_i}$			
	Average nanoparticle diameter (nm)			
	0.9	1.8	4.6	6.7
CH_2(p,down)	0.025	0.005	0.031	0.005
CH_2(p,down)	0.001	0.001	0.010	0.003
CH_3(p,down)	0.001	0.003	0.002	0.001
CH_2(s)	0.022	0.017	0.029	0.011
CH_3(s)	0.071	0.115	0.791	0.796
CH_2(FR)/CH_2(p,up)	0.015	0.004	0.036	0.147
CH_2(a)/CH_3(p,up)	0.782	0.799	0.025	0.028
CH_3(a)	0.084	0.056	0.075	0.009

Discussion of peak fitting for features in SFG spectra at 2680, 2769, 2800, and 2979 cm^{-1}

In the tailing region above 2950 cm^{-1} of the SFG spectra shown in Figure 5.5, a shoulder extends from the CH_2(a)/CH_3(p,up) feature with a distinct kink followed by a baseline that increases in intensity as the wavenumber increases. Even though the positive slope at high wavenumbers can be attributed to a contribution from the non-resonant background, we presume that the shoulder originates from a unique vibrational band. To represent these spectral features in the SFG model, we included a resonance feature located at 2979 cm^{-1} that is out of phase with the CH_2(a)/CH_3(p,up) feature. The feature at 2979 cm^{-1} can be assigned to two possible modes: a CH_3(a) mode that is oriented away from the surface or a perturbed symmetric stretch of a vinylic

methylene group (=CH_2(s,p)) that is bound to the Pt surface. The latter is less likely because the C-H stretches would be equatorial, and therefore, have a very weak SFG signal.[1–3] The CH_3(a) mode is expected for di-σ (1-butene, 2-butene, B13R) or π-allyl (2B1R) binding geometries with a methyl group that has perpendicular vector components with respect to the surface. The location of this CH_3(a) mode is about 20 cm^{-1} higher than typically observed; however, this assignment is consistent with the asymmetric methyl stretch of reaction intermediates observed during *in situ* SFG spectroscopy of methylfuran and dimethylfuran hydrogenation on Pt.[2]

To accurately model the concave shape of the leading edge of the SFG spectra at wavenumbers below 2850 cm^{-1}, we included three additional features located at 2680, 2769 and 2800 cm^{-1}. Vibrational resonances in this low wavenumber region have been reported in a number of adsorbate-metal systems for 'softened' modes that exhibit large red-shifts.[4–7] We attribute the bands at 2680 and 2769 cm^{-1} to CH_2(p,down) resonances of different absorbed intermediates and the band at 2800 cm^{-1} to a CH_3(p,down) resonance. Two CH_2(p,down) resonances were also reported by Manner *et al.*[5] The center of the band at 2680 cm^{-1} is outside of the experimental range and is not shown in Figure 5.2; however, the tailing region of this feature extending above 2700 cm^{-1} contributes to the spectra. While these band assignments may be ambiguous because the spectral region (2700–2830 cm^{-1}) is not well-defined, the locations of the peaks are consistent with adsorbed linear hydrocarbons on Pt(111) observed with RAIRS.[5]

References

(1) Cremer, P. S.; Su, X. C.; Shen, Y. R.; Somorjai, G. A. *J Phys Chem* **1996,** *100,* 16302.
(2) Aliaga, C.; Tsung, C. K.; Alayoglu, S.; Komvopoulos, K.; Yang, P. D.; Somorjai, G. A. *Journal of Physical Chemistry C* **2011,** *115,* 8104.
(3) Yang, M. C.; Chou, K. C.; Somorjai, G. A. *Journal of Physical Chemistry B* **2004,** *108,* 14766.
(4) Fosser, K. A.; Kang, J. H.; Nuzzo, R. G.; Woll, C. *Journal of Chemical Physics* **2007,** *126.*
(5) Manner, W. L.; Bishop, A. R.; Girolami, G. S.; Nuzzo, R. G. *Journal of Physical Chemistry B* **1998,** *102,* 8816.
(6) Yamamoto, M.; Sakurai, Y.; Hosoi, Y.; Ishii, H.; Ito, E.; Kajikawa, K.; Ouchi, Y.; Seki, K. *Surface Science* **1999,** *427-28,* 388.
(7) Himmelhaus, M.; Eisert, F.; Buck, M.; Grunze, M. *Journal of Physical Chemistry B* **2000,** *104,* 576.

Chapter 6: CO Oxidation on PtSn Nanoparticle Catalysts Occurs at the Interface of Pt and Sn-oxide Domains Formed Under Reaction Conditions

6.1 Introduction

CO poisons Pt surfaces and prevents formation of CO_2 by inhibiting O_2 adsorption. While pure Sn becomes readily oxidized in the presence of O_2 and does not react with CO, the rate of CO oxidation can be improved by incorporating Sn into Pt catalysts [1-6]. The barrier to understanding the mechanism of CO oxidation on PtSn, and even pure Pt catalysts, is knowledge of the structure and chemical environment of the surface and the nature of the catalytic active phase. The key in determining the true active phase of the catalyst is monitoring the atomic- and molecular-level details of surface atoms and reactants on the surface of the catalyst as the reaction proceeds. Nanoparticle catalysts can undergo significant structural and compositional changes that depend on the temperature and gas atmosphere during pre-treatment, reaction, and post-treatment [7-9]. Often, pre-natal and post-mortem spectroscopic characterization studies are used to understand the nature of the catalytic active phase. This approach often leads to diverse conclusions because the catalyst surface changes with different treatments and when samples are transferred from reactor to characterization tool. In order to make definitive conclusions about the catalyst's active phase using spectroscopic tools the catalyst must be studied under reaction conditions.

Catalysts that are used industrially and commonly for laboratory kinetic reaction studies present challenges for atomic-level spectroscopic investigations because the porous supports attenuate signal and the active catalyst is polydisperse in size and composition. In order to observe changes of catalyst surfaces under reaction conditions, nanoparticle catalysts should not be embedded

deep within pores of the support material. An effective method that allows for both reaction studies and spectroscopic observation under reaction conditions is deposition of colloidally-prepared nanoparticles onto two-dimensional supports like Si wafers [10, 11]. Understanding how structure and composition of catalysts correlate with catalytic activity and selectivity requires ensembles of nanoparticles that have monodisperse size, shape, and composition distributions. Achieving monodispersity in size and composition is challenging when creating nanoparticles with incipient impregnation methods used in industry (i.e., reducing the metal precursors directly onto a mesoporous or microporous supports like silica or alumina) due to uncontrolled mixing of the precursors at the liquid-solid interface, or from sequential reduction of multiple elements. However, an alternative synthesis approach that provides control over nanoparticle size and composition is inorganic colloidal synthesis [12, 13].

In this work, we use Ambient Pressure X-ray Photoelectron Spectroscopy (APXPS) [14, 15] to monitor the chemical composition and electronic environment of well-defined, colloidally-prepared PtSn nanoparticle catalysts under various gas atmospheres. PtSn catalysts exhibit dynamic segregation with an intermixed Pt-Sn phase under reducing conditions and separated metallic Pt and oxidic Sn domains under CO oxidation reaction atmospheres. By intentionally poisoning the Pt surface sites with CO, we show that the enhanced activity displayed by PtSn catalysts is due to the presence of Sn, which allows for O_2 adsorption and dissociation and a Pt/Sn-oxide interface where SnO is reduced by CO. An alternative and more facile reaction mechanism at the interface is confirmed by measurements of the effective activation barriers and reaction rate dependencies with respect to O_2 and CO.

6.2 Experimental methods and materials

6.2.1 Materials. Hexachloroplatinic acid ($H_2PtCl_6 \cdot 6H_2O$, 99%), tin chloride ($SnCl_2$, 98%), tin(II) acetate ($Sn(C_2H_3O_2)_2$, 99%), poly(vinylpyrrolidone) (PVP, MW = 29,000/55,000 amu), ethylene glycol (reagent grade), hydrochloric acid (HCl, 2 M), sodium hydroxide (NaOH, 99.9 %), sodium borohydride ($NaBH_4$, 99.9 %), acetone (99 %), tetraorthosilicate (99.9%), and ammonium hydroxide (99.9%) were manufactured by Sigma Aldrich. 1,5-pentanediol (95%), ethanol (100 %), and hexane (99.9 %) were manufactured by Fluka, KOPTEC, and BDH, respectively. Oxygen (5.0 UHP), carbon monoxide (5.0 UHP), and helium were purchased from Praxair. Polished Si(100) wafers were purchased from Addison Engineering. To minimize Fe or Ni carbonyls in the reactant gases, CO was stored in an Al cylinder and was passed through Cu tubing heated to 300 ˚C immediately before the reactor inlet.

6.2.2 Nanoparticle synthesis. Pt, PtSn, and Sn nanoparticles were prepared using inorganic colloidal methods as described previously with a PVP capping ligand [10, 16, 17]. The syntheses can be conducted using different initial amounts of precursors as long as the relative ratios remain constant. Polyhedral platinum nanoparticles of 2 nm average diameter were prepared by mixing 10 mL of ethylene glycol, 100 mg of $H_2PtCl_6 \cdot 6H_2O$ (1.9×10^{-4} mol) and 5 mL of a 0.5 M NaOH solution (0.1 g) in a 25 mL three-neck round bottom flask. The flask was sealed with septa and the residual air atmosphere was evacuated by three cycles of vacuum pumping followed by an Ar purge. The synthesis was conducted at 160 ˚C with vigorous stirring in Ar flow for 2 h. After the colloid returned to room temperature, 20.3 mg of PVP (0.18 mol) was added followed by vigorous stirring for 20 min. Finally, 100 mL of acetone was added to the solution and the particles were precipitated by centrifugation at 4000 rpm (VWR Clinical 50) for

~10 min. Further washing with ethanol and hexane was performed three times to remove residual molecular fragments from the particle surface. These nanoparticles, as well as the PtSn and Sn nanopoarticles were stored in ethanol under refrigeration before their use in kinetic and spectroscopic studies.

Polyhedral PtSn nanoparticles of 2.2 nm average diameter were prepared by mixing 10 mL of ethylene glycol, 28 mg of $H_2PtCl_6 \cdot 6H_2O$ (7×10^{-5} mol), 13 mg of $SnCl_2$ (7×10^{-5} mol), and 111 mg of PVP (1×10^{-3} mol) in a 25 mL three-neck round bottom flask. The synthesis was conducted at 160 ˚C with vigorous stirring in Ar flow for 2 h. After the colloid returned to room temperature, 40 mL of acetone was added to the solution and the particles were precipitated by centrifugation and washed with the same procedure used for the Pt nanoparticles.

To synthesize polyhedral Sn nanoparticles of 6 nm average diameter, 0.14 g of $Sn(OAc)_2$ (6×10^{-4} mol) and 1.7 g of PVP (1.5×10^{-2} mol) were loaded into a 100 mL three-neck round bottom flask in a glove box. After adding 20 mL of dried 1,5-pentanediol into the precursor solution, the flask was evacuated by vacuum pumping followed by an Ar purge and heating to 100 ˚C with vigorous stirring. A reducing agent, which was prepared by dissolving 0.23 g of $NaBH_4$ in 60 mL of dried 1,5-pentanediol, was quickly injected into the precursor solution and the reaction was maintained at 100 ˚C for 15 min. After cooling to room temperature, acetone was added to the solution and the nanoparticle solids were precipitated by centrifugation and washed with the same procedure used for the Pt nanoparticles.

Preparation of silica encapsulated Pt and PtSn nanoparticles for reaction studies. For the reaction studies, the Pt and PtSn nanoparticle catalysts were encapsulated in a porous silica shell to eliminate sintering during the long-term high-temperature experiments [18]. The nanoparticles were encapsulated in a SiO_2 shell using a modified sonication-assisted Stöber method with PVP as a pore structuring agent [19, 20]. To prepare the shell surrounding the nanoparticles, a 50 μL aliquot of the as-prepared colloid was mixed by sonication (Branson, 3510) with 15 mL of ethanol in a 20 mL scintillation vial. While the mixture remained in the sonication bath, 2 ± 1 μL of TEOS was added (the total amount varied depending on the concentration of the nanoparticle solution). Following ~ 30 s of continued sonication, 2.25 mL of NH_3OH was added drop wise over a period of 5 min. The solution was left in the sonication bath for 2 h. The ~21 mL solution of core-shell nanoparticles was washed with 21 mL of a 50:50 mixture of acetone and hexane and was precipitated by centrifugation for 10 min.

6.2.3 Catalyst sample preparation (Langmuir-Blodgett film deposition). For kinetic and spectroscopic studies, nanoparticles were supported on two-dimensional surfaces. The use of a two-dimensional support differs from common catalytic studies that use high surface area materials (e.g. silica, alumina, or carbon) as catalyst supports. Surface-sensitive X-ray spectroscopy only probes the particles at the exterior of the high surface area three-dimensional supports. For kinetic studies, SiO_2 encapsulated Pt or PtSn nanoparticles were deposited onto a Si(100) wafer using a Langmuir-Blodgett trough (Kibron, MTX). For spectroscopic studies, the Pt or PtSn nanoparticles were supported on Au-coated Si wafers. Both supports exhibited negligible activity for CO oxidation. Before the Langmuir-Blodgett deposition, the Si surfaces were exposed to strong oxidizers (e.g., piranha or NoChromix) to remove organic residues and

make them hydrophilic (oxidizers hydroxylate the silica). Nanoparticles were dispersed in a 50:50 chloroform:ethanol mixture and deposited onto an ultrapure water subphase (18.2 MΩ·cm). Following the evaporation of the solvent and equilibration of particles (30 – 60 min), the two-dimensional layer of particles was compressed at a rate of 5 mm/min to create a close-packed monolayer. When the monolayer of particles was compressed to a surface pressure in the range of 30-35 mN/m, the substrates were withdrawn at a rate of 2 mm/min while maintaining a constant pressure. Surface tension was monitored using Wilhelmy probe made of a PtIr wire. Following deposition, the core-shell nanoparticles supported on the wafers were calcined in a tube furnace (Lindberg Blue M) at 350 ˚C in ambient conditions to remove the PVP capping agent and create pores in the silica shell [18]. The samples were stored in ambient atmosphere before use.

6.2.4 Morphological characterization. Nanoparticle morphology and size were examined using a Transmission Electron Microscopy (TEM, JEOL 2100) operated at 200 kV. The nanoparticle size was measured using ImageJ v. 1.45s software (NIH). Particle size distributions were obtained with > 300 particles. Nanoparticles were reclaimed from the silica wafers after heat treatments and reactions by rinsing the Si wafer surface in ethanol and collecting the rinsing agent. The dissolved nanoparticles were then precipitated by centrifugation, redispersed in ethanol, and dropcast onto TEM grids for imaging.

Pt and PtSn catalysts had an average diameter of 2.1 ± 0.4 and 2.2 ± 0.4 nm, respectively. For the CO oxidation reaction studies, the catalysts were encapsulated within inorganic porous silica shells to provide sintering resistance during long-term high temperature studies. We did not

encapsulate the catalysts for the spectroscopic studies, which were performed over relatively shorter periods of time. The encapsulation is important to maintain catalyst morphology when catalysts are supported on two-dimensional, flat, supports like Si (or silica) wafers. The nature of the smooth support coupled with the size-dependent melting point depression of nanometer size metals [21, 22] increases the rate of agglomeration. However, catalysts that are coated with porous silica shells have thermal stability up to 700 ˚C [18]. We were able to obtain porous shells that encapsulate multiple nanoparticles as shown in the Supplementary Information Figure S.6.1. The encapsulated nanoparticles shown demonstrate the particle morphology and size (monodispersity of the nanoparticles is displayed by nanoparticle size distributions shown in the insets). Negligible changes in nanoparticle morphology were observed after multiple treatment/reaction cycles at temperatures up to 350 ˚C. PtSn catalysts that were reclaimed after many cycles of treatment and reaction cycles are shown in Figure S.6.1. The average particle size of a sample of PtSn cores after performing reaction studies was 2.3 ± 0.5 nm.

6.2.5 Chemical Characterization. Chemical characterization of the catalysts was performed using lab-based and synchrotron-based XPS systems and Energy Dispersive Spectroscopy (EDS). Lab-based PHI 5400 XPS system was used under ultra-high vacuum conditions with an Al anode operated at 350 W. Samples were maintained at room temperature and 5 x 10^{-9} Torr vacuum during characterization. The synchrotron-based APXPS system at beamline 9.3.2 at the Advanced Light Source was operated under ultrahigh vacuum (1 x 10^{-9} Torr), 100 mTorr H_2 reducing conditions, and a reaction gas mixture of 100 mTorr CO and 40 mTorr O_2. The sample was heated to temperatures between 100 and 375 ˚C using a resistive heating element positioned in contact with the sample [23]. To maintain similar penetration depths for Pt and Sn, we kept

the kinetic energy constant for the Sn and Pt signals using photon energies of 320 and 740 eV, respectively (unless otherwise noted).

Curve fitting of the Sn $3d_{5/2}$, Pt 4f, and O 1s XPS spectra was performed using CasaXPS v.2.3.15 software. The binding energies in the spectra were calibrated using the Au $4f_{7/2}$ feature at a binding energy of 84 eV [24]. The intensity of the Sn $3d_{5/2}$, Pt 4f, and O 1s spectra were normalized by the Au $4f_{7/2}$ peak intensity at the constant photon energy to account for signal attenuation due to X-ray absorption by ambient gases. During fitting, the position and full width at half maximum (FWHM) of the Sn $3d_{5/2}$, Pt 4f and O 1s features were held constant across different gas environments with a unique FWHM value for each chemical state (c.f. Table 6.1); only the area was unconstrained. The Pt 4f orbitals were described by two features for each hybrid state. We used a constant spin-orbit splitting value of 3.3 eV and a branching ratio of 0.75 for 5/2:7/2 states. The Sn $3d_{5/2}$ spectral features were fit using an asymmetric Lorentzian distribution (LA(1.1, 1.7, 35)) and the Pt 4f and O 1s spectral features were fit using a sum of Gaussian and Lorentzian distributions (SGL(35)) as performed by Jugnet *et al.*[4]. The spectra were fit using a Shirley background. Relative sensitivity factors of 5.575, 4.725, and 0.71 were used for the Pt 4f, Sn $3d_{5/2}$, and O 1s spectra [25].

EDS measurements of ensembles of atoms were performed with an electron source operated at 120 kV on a Cu TEM grid (EDAX Si(Li) detector, Ametek, Inc).

Table 6.1: Peak assignments and full width half maximum for Sn $3d_{5/2}$, Pt 4f, and O 1s X-ray photoelectron spectroscopy features.

Sn 3d $_{5/2}$	Location (eV)	FWHM		Pt 4f	Location (eV)	FWHM		O 1s	Location (eV)	FWHM
Sn^0	485.2	0.8		Pt^0	70.8-71.1	0.9		SnO_x	530.4	1.4
Sn(Pt)	485.7	0.9		Pt(Sn)	71.4	0.9				
Sn^{2+}	486.4	0.9		Pt-CO/O	72.5	1.6				
Sn^{4+}	487.3	1.3								

6.2.6 Kinetic measurements. CO oxidation was performed in a 1 L stainless steel chamber that was sealed with Conflat flanges and Cu or Viton gaskets. A mechanical rotary pump was used to remove ambient gases before introducing the reactant gases. The pressure of the reactant gases was monitored with a capacitance manometer pressure gauge (MKS Baratron). A metal bellows recirculating pump (Senior Aerospace MB-21) was used to mix the gases within the chamber to eliminate mass transfer issues. A pervasive problem encountered with studies of CO oxidation is the local exotherms caused by the -284 kJ/mol thermodynamic energy difference between CO and CO_2. The effects of temperature drift were minimized using a water-cooled heating manifold in conjunction with the resistively-heated boronitride plate (Momentive) to support and heat the catalyst sample. In addition, gas-phase dilution of the reactant gases with He provided efficient conductive heat transfer away from the sample. The temperature of the sample was monitored using a type-K thermocouple. The conversion of CO to CO_2 was monitored using a differentially-pumped quadrupole mass spectrometer (QMS, Stanford Research Systems, RGA 200) with a turbomolecular pump to maintain vacuum pressures (Pfeiffer, TMU-260). The reaction chamber was connected to the QMS via a 10 μm ID by 1 m length silica capillary (Restek), which yielded a pressure of 2×10^{-6} Torr in the QMS chamber with 760 Torr gas pressure in the reactor. Activity measurements were performed under differential conditions, in which conversion was < 10%.

6.3 Results

6.3.1 CO oxidation reaction studies with Pt and PtSn nanoparticle catalysts

The kinetic behaviors for CO oxidation on Pt and PtSn nanoparticle catalysts were studied by measuring the net effective activation barrier (ΔE_{eff}) and O_2 and CO reaction orders. In the presence of gaseous CO at temperatures < 300 ˚C, Pt surfaces (and modified Pt surfaces) are highly populated by chemisorbed CO. High CO occupancy inhibits dissociative adsorption of O_2 at Pt sites [6, 26-28]. To determine the effects of Sn in the PtSn catalyst, we chose to intentionally poison the Pt active sites using CO-rich reaction conditions (100 Torr CO and 40 Torr O_2). With a high population of CO adsorbed on the surface, we correlate any changes observed in the reaction mechanisms (determined from ΔE_{eff} and O_2 reaction orders) to the presence of Sn alone.

6.3.2 Effective activation barriers for CO oxidation

To compare the CO oxidation activity on the Pt and PtSn catalysts we use measurements of ΔE_{eff} rather than turnover frequencies (TOF). We do not provide TOF values because we have not identified an appropriate method to count active sites on the PtSn catalysts, which we show to be different than on pure Pt catalysts. To determine ΔE_{eff} values on Pt and PtSn catalysts, the rates of CO_2 formation (r) were measured as a function of temperature in the range of 200 to 300 ˚C and a gas mixture of 100 Torr CO, 40 Torr O_2, and 630 Torr He. Arrhenius plots (ln(r) versus T^{-1}) for the Pt (red) and PtSn (blue) nanoparticle catalysts are shown in Figure 6.1(a). A straight line indicates that mass-transfer limitations are negligible. The difference in slopes indicates different ΔE_{eff} values for the Pt and PtSn catalysts and different reaction mechanisms. The

steeper slope observed with the Pt catalysts corresponds to an $\Delta E_{eff,\mathrm{Pt}} = 133 \pm 25$ kJ/mol. This value is in general agreement with the $\Delta E_{eff,\mathrm{Pt}}$ values previously reported for vapor-deposited Pt catalysts on SiO_2 supports (110 kJ/mol) [29], nanoparticle catalysts encapsulated in SiO_2 (115 kJ/mol),[18] and Pt single crystals (140 kJ/mol) [30]. In comparison, PtSn catalysts promote the CO oxidation reaction with an $\Delta E_{eff,\mathrm{PtSn}} = 35.7 \pm 4$ kJ/mol. This value is consistent with $\Delta E_{eff,\mathrm{PtSn}}$ observed from thermal induced desorption on a $Pt_3Sn(111)$-(2x2) single crystal (30.4 kJ/mol) [2] and ~3.8 nm Pt_3Sn nanoparticle catalysts supported on Al_2O_3 (31 kJ/mol) [31]. The difference in activation barriers correlates with the increased activity observed previously with PtSn catalysts [1, 2, 6, 32-35].

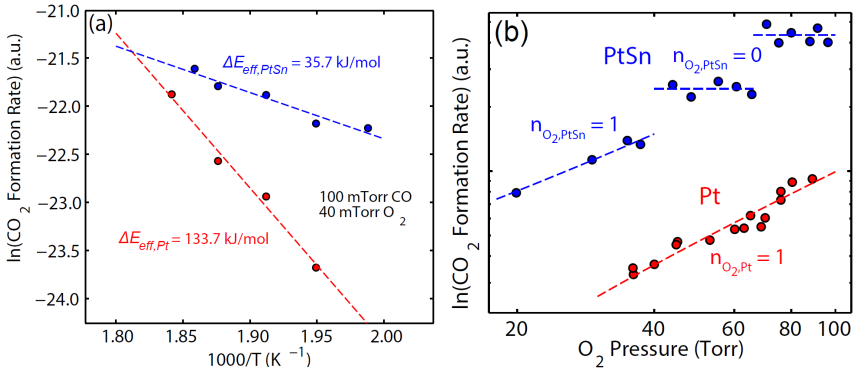

Figure 6.1: (a) Arrhenius plot for CO_2 formation on 2 nm Pt (red) and 2 nm PtSn (blue) nanoparticle catalysts. The reaction rates were determined between 200 and 300 ˚C. (b) Plot of the ln(CO_2 formation rate) versus ln(P_{O_2}) yields the reaction order in O_2 for 2 nm Pt (red) and 2 nm PtSn (blue) catalysts.

6.3.3 Kinetic reaction orders for O_2 and CO for CO_2 production

The kinetic reaction orders for CO and O_2 with respect to the rate of CO_2 formation were determined at 260 ˚C. The kinetic reaction order for O_2 on the Pt ($n_{O_2,\mathrm{Pt}}$) and PtSn ($n_{O_2,\mathrm{PtSn}}$)

catalysts were obtained in 100 Torr CO, partial pressures of O_2 (P_{O_2}) in the range of $20 \leq P_{O_2} \leq 100$ Torr, and 660 Torr of He. During these experiments the total pressure increased above 1 atm; however, we found that the reaction is zero-order in total pressure, which is in agreement with Berlowitz *et al*.[36]. The values of $n_{O_2,Pt}$ and $n_{O_2,PtSn}$ were determined from the slopes given by a $\ln(r)$-$\ln(P_{O_2})$ relationship as shown in Figure 6.1(b) for the Pt (red) and PtSn (blue) catalysts. The relative rates for each catalyst shown in the figure are dependent on the number of catalytic active sites. Since, the number of active sites was not measured as discussed above, the rates should not be compared directly. The Pt catalysts exhibit a $n_{O_2,Pt} = 1.06 \pm 0.18$, which is consistent with previous reports [29, 31, 36-38]. A first-order dependence in O_2 is consistent with a reaction mechanism that is controlled by O_2 adsorption before dissociation or molecular O_2 adsorption. Dissociation is not the rate-limiting step because two sites are required and n_{O_2} would be equal to 0.5.

On the PtSn nanoparticle catalysts we observed a variation in $n_{O_2,PtSn}$ as a function of P_{O_2}. When $P_{O_2} < 40$ Torr, $n_{O_2,PtSn} = 1.04 \pm 0.08$; which is consistent with the behavior observed with the Pt catalysts. When $P_{O_2} > 40$ Torr, $n_{O_2,PtSn}$ transitions to a value of zero. The reaction exhibits zero-order dependence in O_2 with increasing P_{O_2}. We also observed a discontinuous increase in the rate at $P_{O_2} = 70$ Torr as the pressure was increased. This repeatable phenomenon may be related to a change in the surface structure of the catalyst; however, we did not pursue further investigations. The transition from first- to zero-order dependence suggests that the rate-limiting step is not O_2 adsorption, but instead a chemical process that occurs on the catalyst since adsorption processes are rarely zero-order. The behavior can occur when the concentration of a given species starts low and becomes sufficiently large that it remains unchanged as the reaction

proceeds. Thus, in contrast to the pure Pt catalysts that are rate-limited by O_2 adsorption when it is poisoned by CO, the zero-order dependence on the PtSn catalyst is consistent with a reaction mechanism that is not inhibited by CO. In other words, Sn is a likely active center for O_2 adsorption and dissociation. A system consisting of Pt catalysts deposited onto a SnO_2 support was also found to have zero-order dependence in O_2 [39].

The kinetic reaction order for CO on Pt ($n_{CO,Pt}$) and PtSn ($n_{CO,PtSn}$) catalysts were also obtained (c.f. Figure S.6.2, Supporting information). Both catalysts exhibited nearly identical behaviors, which confirm that CO is interacting primarily with Pt active sites and Sn does not alter CO adsorption significantly.

Chemical states and composition of 2 nm PtSn nanoparticles under reaction conditions

To determine the chemical states and composition of the PtSn catalyst surface during reducing pre- and post-treatments and the active state on the catalyst surface during CO oxidation we used *in situ* APXPS studies. The structure and surface composition of a catalyst often changes when exposed to different gas atmospheres during pre- and post-treatments and reaction conditions [7-9, 40, 41]. A mutable catalyst surface can positively affect a reaction by providing a new and more facile reaction pathway or negatively affect a reaction by forming a core-shell structure that encapsulates one element in a binary nanoparticle. In some catalytic systems, surface structures existing after pre-treatment procedures degrade under reaction conditions [42]. In other cases, the phase of a catalyst that provides superior catalytic activity forms only under reaction conditions. In this work, we found that the active phase of 2 nm PtSn nanoparticle catalysts was formed under reaction conditions. When exposed to a fully reducing atmosphere, the surface exhibited a

Pt-Sn intermixed phase. However, during reaction conditions, the surface was comprised of metallic Pt and Sn-oxide domains that shared an interface at the surface of the nanoparticle. The chemical states of Pt and Sn in the PtSn nanoparticle catalysts supported on a Si wafer were monitored during heat treatment in vacuum, pre-treatment reduction in H_2, CO and O_2 reaction conditions, and post-treatment reduction in H_2. The chemical environment of the Sn in the PtSn nanoparticle catalysts was determined by monitoring photoemission of Sn $3d_{5/2}$ core-level electrons using a photon energy, $h\nu$ = 740 eV, which provides a kinetic energy for the photoelectrons of ~250 eV and an inelastic mean free path of 7 Å in a pure Sn environment [43]. The chemical environment of Pt was identified by monitoring photoemission of Pt 4f core-level electrons using $h\nu$ = 320 eV (to match the kinetic energy and probing depth used for the Sn). We also measured the chemical environment of O by monitoring photoemission of O 1s core-level electrons using $h\nu$ = 740 eV.

Following a heat-treatment to 356 ˚C in vacuum and a reducing pre-treatment at 370 ˚C in 100 mTorr of H_2, the 2 nm PtSn nanoparticle surface was comprised of both Pt and Sn atoms. The Sn $3d_{5/2}$ (variations of blue) and Pt 4f doublet spectra (variations of green) measured during the reducing pre-treatment are shown in Figure 6.2(a). The near surface composition of Pt and Sn in the PtSn nanoparticles determined from these spectra was 54 % Pt and 46 % Sn. These values are in agreement with the EDS results.

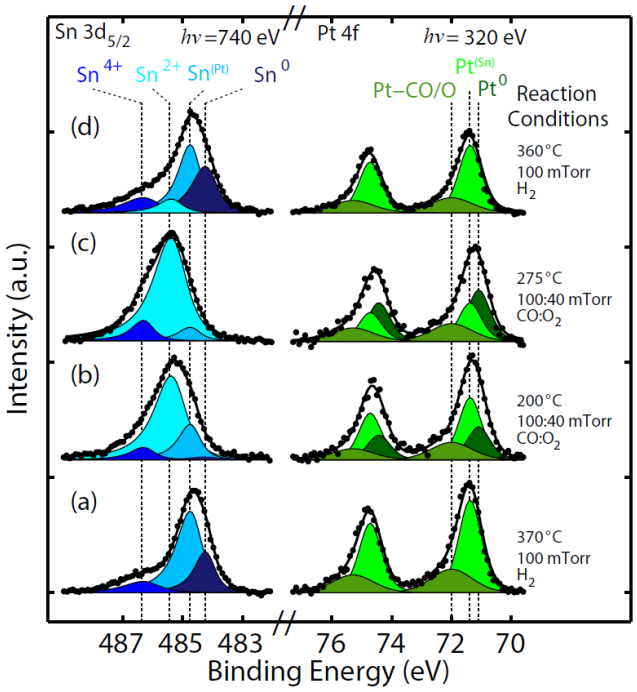

Figure 6.2: *In situ* Sn $3d_{5/2}$ (variations of blue) and Pt 4f (variations of green) ambient pressure X-ray photoelectron spectra for 2 nm PtSn nanoparticle catalysts during (a) pre-treatment reduction in 100 mTorr H_2 at 370 ˚C, (b) reaction conditions with 100 mTorr CO and 40 mTorr O_2 at 200 ˚C, (c) reaction conditions with 100 mTorr CO and 40 mTorr O_2 at 275 ˚C, and (d) post-treatment in 100 mTorr H_2 at 360 ˚C. The Sn $3d_{5/2}$ spectra are deconvoluted into peaks assigned to metallic Sn (Sn^0), Sn in a Pt environment ($Sn^{(Pt)}$), Sn^{2+}, and a Sn^{4+} oxide state at 485.2, 485.8, 486.4 and 487.3 eV, respectively. The Pt 4f spectra are deconvoluted into peaks assigned to metallic Pt (Pt^0), Pt in a Sn environment ($Pt^{(Sn)}$), and a feature that possibly includes Pt bound to chemisorbed CO, O, and Pt-carbonyl from the capping agent (Pt-CO/O) at 70.8, 71.4, and 72.5 eV. The spectra indicate that PtSn catalysts segregate into Sn^{2+} and Pt^0 domains under reaction conditions from an intermixed Pt and Sn domain under H_2 reducing conditions.

The Sn core-level spectrum under reducing pre-treatment conditions (Figure 6.2(a)) exhibits three distinct chemical states. The spectrum is deconvoluted into features assigned to metallic Sn (Sn^0), Sn in a Pt environment ($Sn^{(Pt)}$), and a Sn^{4+} oxide state at 485.2, 485.8, and 487.3 eV, respectively. The peak locations and FWHM of all core-level features described herein are presented in Table 6.1. The two metallic features reside within the previously reported range of binding energies of 484.7 – 485.8 eV [1, 4, 44-47]. The positive core-level shift of the $Sn^{(Pt)}$ feature with respect to the location of Sn^0 is consistent with electron exchange between the Pt and Sn atoms in an alloy environment [1, 5, 45, 48]. Regions of alloyed Sn with Pt and isolated domains of the elements are possible with colloidally-synthesized binary metal nanoparticles, which grow inhomogeneously due to different redox potentials of the elements and the statistically random nature of atomic attachment to the metal seed during the growth stage [49]. The Sn^{4+} core-level shift exceeds previous reports for bulk SnO_2 by 0.6 eV [1, 50]. The binding energy shift is likely a property of the nanoparticle's dimensions [24, 51, 52]. A Sn^{2+} state, which has a photoemission feature at 486.4 eV, is not present under these reducing conditions. However, prior to pretreatment, the PtSn nanoparticles exhibited Sn^0, $Sn^{(Pt)}$, Sn^{4+} and Sn^{2+} chemical states. XPS spectra of the Sn $3d_{5/2}$ core-level electrons over the course of an hour and temperatures of 200 – 370 ˚C in vacuum – prior to exposure to the H_2 atmosphere – and the progression of the Sn^0, $Sn^{(Pt)}$, Sn^{2+}, and Sn^{4+} states during the treatment are shown in Figure S.6.4 and S.6.5 in the Supporting Information, respectively. As the PtSn nanoparticles were heated in vacuum to 356 ˚C, the concentration of oxide features diminished at the benefit of the Sn^0 and $Sn^{(Pt)}$ components. While Sn^{4+} remained following treatment, the Sn^{2+} was completely reduced. The Pt $4f_{7/2}$ orbital spectra is deconvoluted into two features for each hybrid state: Pt in a Sn environment ($Pt^{(Sn)}$) located at 71.4 eV, which complements the $Sn^{(Pt)}$ feature and a relatively

broad feature at 72.5 eV that possibly includes Pt bound to chemisorbed CO, O, and Pt-carbonyl from the polyvinylpyrrolidone (PVP) capping agent (Pt-CO/O) [4, 26]. A shift of the Pt core-level electrons in X-ray absorption studies (i.e., whiteline position) has also been observed in the presence of Sn for Pt_xSn alloy nanoparticle catalysts [53]. The combination feature at 72.5 eV does not include Pt oxides, which exhibit a $Pt_{7/2}$ core-level feature that appears above 73 eV [6, 26, 53, 54]. Matching Pt $4f_{5/2}$ hybrid orbital features are shown with a spacing of 3.3 eV above the Pt $4f_{7/2}$ orbital.

The chemical states of O during reducing and reaction environments are shown by photoemission of O 1s core-level electrons in the XPS spectra in Figure S.6.6 of the Supporting Information. The O 1s spectrum shows no indication of O in Sn-oxide during reducing pre-treatments.

As a reference for the different chemical states of Pt, Sn, and O, we characterized nanoparticles of pure Pt, pure Sn, and PtSn *ex-situ* under vacuum conditions using a lab-based XPS system. A comparison of the Pt 4f, Sn $3d_{5/2}$ and O1s spectra for the three nanoparticles after a reduction treatment at 350 ˚C in 1 atm of H_2 and transfer through ambient conditions to the analysis chamber are shown in Figure S.6.2 of the Supporting Information.

The active phase of the PtSn catalysts under a reaction atmosphere of 100 mTorr CO and 40 mTorr O_2 at 200 ˚C is shown in Figure 6.2(b). The gas phase ratio used in the APXPS studies matches the gas ratio used in the kinetic studies with excess CO to poison the Pt sites. Two changes occurred in the Sn and Pt XPS spectra with respect to the chemical states during

reducing atmospheres: (1) a Sn^{2+} feature located at 486.4 eV appeared at the expense of $Sn^{(Pt)}$ and Sn^0 and (2) a feature at 70.8 eV corresponding to Pt^0 that is not near Sn atoms increased at the expense of $Pt^{(Sn)}$ and Pt-CO/O. The Pt^0 feature is located 0.6 eV lower than the Pt(Sn) feature and is consistent with the binding energy of bulk metallic Pt [26]. Continuing with a gaseous atmosphere of 100 mTorr CO and 40 mTorr O_2 at a higher temperature of 275 ˚C, the proportion of Sn^{2+} and Pt^0 increased further. The formation of Sn^{2+} and Pt^0 at the expense of the $Sn^{(Pt)}$ and $Pt^{(Sn)}$ intermixed domain indicates atomic segregation in the $CO:O_2$ reaction environment to form an active phase composed of Sn-oxide and metallic Pt islands. The O 1s spectrum shown in the Supporting Information also exhibits an XPS feature that is consistent with oxidized Sn (Figure S.6.6).

The formation of separate Pt^0 and Sn-oxide domains was found to be reversible. The Sn $3d_{5/2}$ and Pt 4f spectra during post-treatment in 100 mTorr H_2 at 360 ˚C is shown in Figure 6.2(d). Again, the dominant features in the Sn $3d_{5/2}$ spectra comprise Sn^0, $Sn^{(Pt)}$, and Sn^{4+}, while the dominant features in the Pt 4f spectra comprise $Pt^{(Sn)}$ and Pt-CO/O. Comparison of the Sn $3d_{5/2}$ and Pt 4f spectra during pre-treatment and post-treatment indicates that re-reducing the catalyst following the reaction prompted the Pt and Sn atoms to return to the physically-mixed, metallic state that was measured prior to performing the reaction. A minority amount of Sn^{2+} remained on the surface during the post-treatment reduction; however, the trends observed of the course of the post-treatment suggest that the Sn^{2+} will diminish completely. The XPS spectra over the course of the post-treatment and the progression of the Sn^0, $Sn^{(Pt)}$, Sn^{2+}, and Sn^{4+} states are shown in Figure S.6.7 and S.6.8 of the Supporting Information, respectively.

The progression of Sn^0, $Sn^{(Pt)}$, and Sn^{2+} and Pt^0 and $Pt^{(Sn)}$ from pre-treatment, reaction, and post-treatment conditions is shown in Figure 6.3(a) and (b) for the Sn and Pt species, respectively. Neither Sn^{4+} nor Pt-CO/O compositions are shown in the figures because the chemical states exhibit negligible change when switching atmospheres. The two panels display a correlation between the $Sn^{(Pt)}$, Sn^0, and $Pt^{(Sn)}$ states and a correlation between the Sn^{2+} and Pt^0 states. That is, the concentration of the intermixed domains decreases under reaction conditions and metallic Pt and Sn-oxide domains increase. Under reaction conditions at 275 ˚C, the concentration of Sn^{2+} reached ~82% with negligible Sn^0 while the $Sn^{(Pt)}$ state endured. The presence of the intermixed features indicates the existence of an interface between the Pt and Sn. The presence of the $Pt^{(Sn)}$ also indicates that an interface is present. The reemergence of $Pt^{(Sn)}$ and $Sn^{(Pt)}$ states during post-treatment also suggests that there is an interface present between two domains. $Sn^{(Pt)}$ and $Pt^{(Sn)}$ likely originate from Sn^{2+} that is reduced at the interface with Pt; whereas, Sn^0 is formed from the Sn^{2+} atoms that are located in the interior of the domains or in the subsurface/bulk of the nanoparticle.

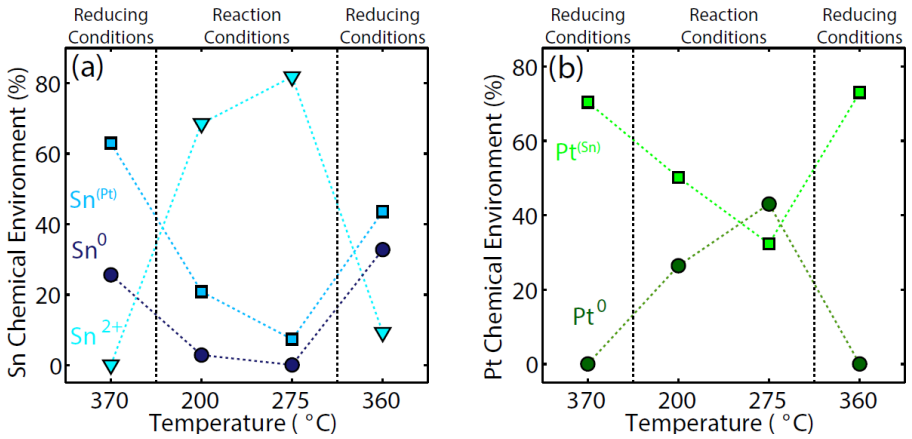

Figure 6.3: Progression of the different chemical environments of (a) Sn and (b) Pt in the 2 nm PtSn nanoparticle catalysts when transitioning from pre-treatment, reaction, and post-treatment conditions. The trends for Sn^0, Sn(Pt), Sn^{2+}, Pt^0 and Pt(Sn) correspond to features in the ambient

pressure X-ray photoelectron spectra in Figure 6.2. Under H_2 reducing conditions, Sn^0, Sn(Pt), and Pt(Sn) are the dominant chemical states. During CO oxidation, the dominant chemical states are Sn^{2+} and Pt^0. The dynamic behavior suggests that the elements migrate to form distinguishable domains and the reaction occurs at a Pt/Sn-oxide interface.

Following the first pre-treatment, Sn^{4+} was observed with a composition of ~15% relative to all Sn species regardless of the gas atmosphere and temperature. The fact that Sn^{4+} does not increase in content (not shown) suggests that nanoparticles remain as in a single composite matrix rather than separate into isolated nanoparticles as was shown by Uemera *et al.*[53]. While the seemingly obvious location of the active Sn phase is located at the catalyst surface, there have been suggestions that Sn^{2+} (i.e., SnO) is located in the subsurface, while Sn^{4+} (i.e., SnO_2 populates the surface) [1]. This is consistent with SnO_2 phases having a lower surface free energy than the partially and fully reduced components [55]. To assess the location of the different Sn phases, we adjusted the kinetic energy of the synchrotron radiation to vary the probing depth. Figure 6.4 shows the Sn $3d_{5/2}$ spectra following the post-treatment in H_2 with $h\nu$ = 560 and 740 eV. The kinetic energy gives an effective probing depth of 4 versus 7 Å for Sn atoms in a pure Sn environment. Comparison of the intensities of the Sn^{2+} and Sn^{4+} in the two spectra indicates that the top surface layer is predominately composed of Sn^{4+} even after reduction treatment and the subsurface contains the Sn^{2+}, Sn^0 and $Sn^{(Pt)}$ phases.

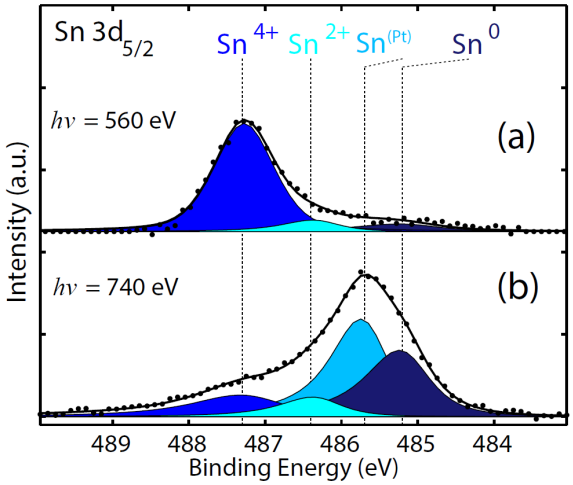

Figure 6.4: *In situ* Sn $3d_{5/2}$ ambient pressure X-ray photoelectron spectra of PtSn nanoparticle catalysts during the post-reduction treatment at different photon kinetic energies. (a) The top surface layer is probed exclusively with a photon energy of 560 eV, whereas (b) the surface and subsurface are probed with a photon energy of 740 eV. The spectra indicate that the top surface layer is dominated by a Sn^{4+} state and the subsurface atomic layers are composed of Sn^{0} and $Sn^{(Pt)}$ states, which are likely converted to Sn^{2+} under reaction conditions

6.4 Discussion

The catalytic benefits of Sn when added to Pt catalysts for CO oxidation have been described by changes in the binding of CO and O to the catalyst surface. Both spectroscopic measurements and theoretical predications on $Pt_3Sn(111)$ alloy single crystal surfaces have indicated that Sn shifts the d-band of Pt away from the Fermi level, and thus reduces the adsorption strength of CO on Pt (i.e., electronic ligand effects) [5, 48, 56]. Reducing the binding strength of CO promotes desorption at lower temperatures and allows for O_2 adsorption; that is, the alloy reduces the effects of CO inhibition over the net oxidation rate. PtSn hollow adsorption sites on $Pt_3Sn(111)$ alloy single crystal surfaces were also proposed to be influential in the reaction. The hollow sites were proposed to have a lower activation barrier for O_2 adsorption and dissociation in the

presence of CO (i.e., ensemble effects) [4]. Enhanced CO oxidation at the interface between Pt (with adsorbed CO) and Sn (with adsorbed O) has also been proposed using Pt supported on Sn-oxide and inverse catalysts of Sn-oxides supported on Pt single crystals [1, 3, 39, 57, 58]. Our results using real PtSn nanoparticle catalysts also indicate that a reaction at a metal/metal-oxide interface is responsible for the high activity.

The spectroscopic results presented herein confirm that Pt and Sn are mobile within the nanoparticle and diffuse to form separate domains on the nanoparticle surface. The facile formation of isolated and intermixed domains suggests that Pt and Sn do not completely phase separate to form isolated nanoparticles. This behavior, which yields SnO_2, has been shown to occur under oxidizing conditions at temperatures above 350 ˚C [53]. As we determined when measuring the reference spectra, pure Sn is not readily reduced back to the lower oxidation states of Sn. Therefore, the reversible nature suggests that the atoms remain together intact within a single nanoparticle composite. Under reducing conditions, the Pt and Sn atoms diffuse together to form a mixed phase, which was identified by the positive core-level shift in the XPS spectra. During CO oxidation, the spectroscopic signatures of intermixed Sn and Pt atoms disappeared at the expense of metallic Pt and oxidic Sn. In this picture, adsorbed CO resides on Pt domains, while O resides on or in the bulk of Sn domains. An illustration of the physical changes at the surface of 2 nm PtSn nanoparticle catalysts is shown in Figure 6.5 with gray and orange atoms representing the Pt and Sn^{x+}, respectively, in (a) reducing and (b) reaction conditions. The illustration does not distinguish between different oxidation states of Sn.

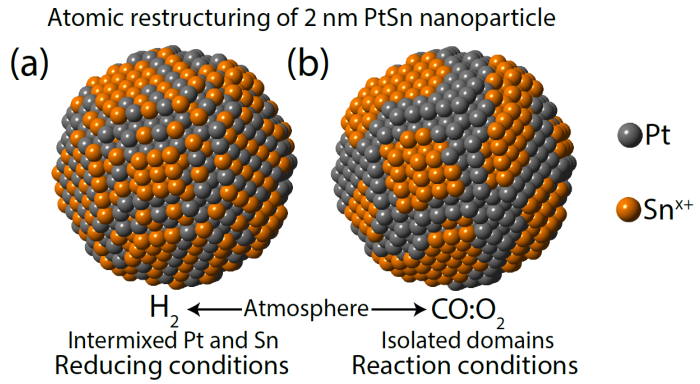

Figure 6.5: Illustration of the segregation behavior between (a) intermixed Pt and Sn domains (reducing conditions) and (b) Pt and Sn-oxide domains (reaction conditions) for a 2 nm PtSn nanoparticle. Pt and Sn atoms are grey and orange, respectively. The illustration does not distinguish between different chemical states of Pt and Sn.

The kinetic results corroborate the concept of different CO and O adsorption sites. In contrast to the first-order dependence observed for O_2 on the Pt catalysts, a zero-order dependence in O_2 was observed for the PtSn catalyst. Pure Sn single crystals readily dissociate O at room temperature to form chemisorbed surface Sn oxide with negligible activation barrier [59, 60]. O also diffuses into the subsurface and bulk of Sn with low activation barriers (< 30 kJ/mol) [45, 59-61]. Thus, the zero-order dependence in O_2 for CO_2 formation on the PtSn nanoparticle catalyst is related to the high concentration of O adsorbed on/within the Sn domains of the nanoparticle.

The active Sn-oxide phase or the Sn species being reduced remain under debate. Some reports argue that SnO_2 is the active state of the catalyst given the high concentration of the Sn^{4+} oxidation state observed during *ex-situ* studies [3, 33]. We have also shown that the topmost

surface is composed of predominately Sn^{4+} species during the post-treatment reduction treatment. Others have argued that SnO is the active phase, including a recent study on a $Pt_3Sn(111)$ single crystal that monitored the surface chemistry using APXPS [1, 4]. The predominance of Sn^{2+} observed under reaction conditions in our study confirms that Sn^{2+} must be the active phase of Sn on PtSn nanoparticle catalysts. Under reaction conditions, the dominant Sn^{2+} species was accompanied by a small amount of Sn^{4+} (~15%) that remained relatively constant at the two temperatures and with the post-treatment reduction. By varying the penetration depth of the synchrotron radiation, we determined that Sn^{4+} was located on the top surface layer and the subsurface/near-surface region and Pt/Sn interface was composed of the remaining three Sn phases, which were converted completely to Sn^{2+} under reaction conditions.

Our results suggest a distinct reaction mechanism for CO oxidation occurs at the Pt/Sn interface on the PtSn catalysts as illustrated in Figure 6.6. In the depiction, a Pt-Sn interface is already formed. CO adsorbs only on the Pt domains and hinders O occupation; and thus, O adsorbs only on Sn domains. When the catalyst is exposed to reducing atmospheres (e.g., CO) the Sn domains have metallic Sn located in the subsurface/bulk with a Sn^{4+} topmost layer (Figure 6.6(a)). When the catalyst is exposed to CO and O_2 (Figure 6.6(b)), O_2 dissociates on the surface of the Sn domains and transports into the bulk of the domain to form Sn^{2+} chemical states (e.g., SnO) [45]. Formation of subsurface and bulk Sn-oxides has been shown previously on PtSn alloy and Sn single crystal surfaces [45, 59, 60]. The likely mechanism for CO oxidation involves a redox shuttle at the interface of Pt and Sn with concerted renewal of O (Figure 6.6(c) and (d)). There are two possible Sn redox couples: Sn^{4+}-Sn^{2+} or Sn^{2+}-Sn^0. Previous reports have shown that CO will not reduce SnO_2 [1, 6, 53, 56, 62] or a surface composed of 1 ML of SnO_2 deposited onto a

Pt(111) single crystal [1]. Moreover, our observation that SnO_2 will not completely reduce under a H_2 environment, even though H_2 has much higher reduction potential than CO. This indicates that a Sn^{4+}-Sn^{2+} redox couple is unlikely. Rather, CO reduces SnO (Sn^{2+}-Sn^0 redox couple) that is located at the Pt/Sn interface with concerted renewal of O from a Sn^{2+} subsurface reservoir (Figure 6.6(d)).

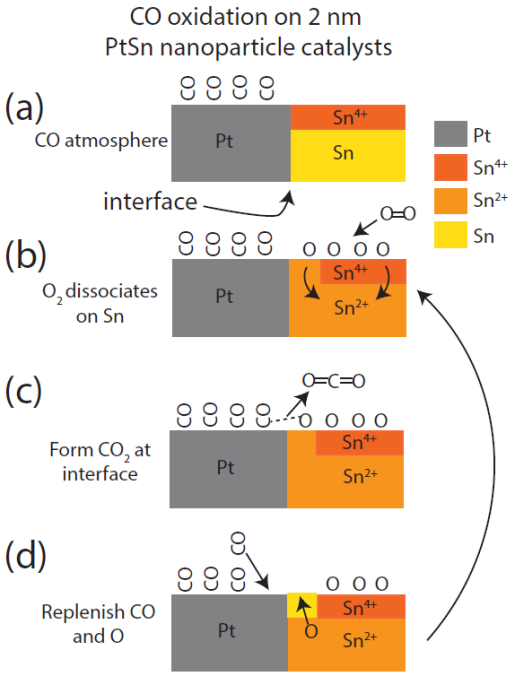

Figure 6.6: Proposed mechanistic scheme for CO oxidation on 2 nm PtSn nanoparticles. Pt and Sn domains form an interface that exists at the nanoparticle surface under reaction conditions. CO is adsorbed only on Pt domains (a). The Sn domain is covered by a Sn^{4+} layer. When O_2 is added to the gas mixture, Sn^0/Sn(Pt) in the subsurface converts to Sn^{2+} (b). CO_2 is formed at the interface of Sn-oxide and Pt domains whereby CO from Pt reduces a Sn^{2+}-Sn^0 redox couple (c) and the Sn site is replenished by O from the subsurface reservoir (d).

6.5 Conclusions

PtSn catalysts provide an alternative and more facile reaction pathway for CO oxidation in comparison to pure Pt catalysts. We show that the kinetic mechanism of CO oxidation on PtSn catalysts is not limited by O_2 adsorption as observed on pure Pt catalysts. Instead, the PtSn catalyst is highly populated by O on the surface and subsurface regions of Sn. Ambient-pressure X-ray photoelectron spectroscopy measurements of monodisperse PtSn nanoparticle catalysts showed that Pt and Sn atoms are mobile. The PtSn nanoparticles transform from intermixed Pt and Sn domains to metallic Pt and oxidic Sn domains during CO oxidation. While pure Pt catalysts displayed a reaction mechanism with an activation barrier of 133 kJ/mol, the PtSn catalysts displayed a reaction mechanism with an activation barrier of 35 kJ/mol. By intentionally poisoning the Pt sites with CO, we revealed that the low activation barrier was due to a redox reaction (Sn^{2+}-Sn^{0} redox couple) that occurred at the interface of Pt and Sn-oxide domains. We determined that the dominant chemical species of Sn was the partially oxidized Sn^{2+} rather than the fully oxidized Sn^{4+}. However, by adjusting the kinetic energy of the synchrotron radiation, we showed that the surface of the Sn domains is covered by a layer of Sn^{4+}. The high mobility of Pt and Sn in the nanoparticles and the reversibility of the chemical state with changing atmospheres make this catalytic system difficult to study using *ex-situ* methods. The key to understanding the active phase of a catalyst is measuring the atomic level properties under reaction conditions.

6.6 References

[1] S. Axnanda, W.P. Zhou, M.G. White, CO oxidation on nanostructured SnO_x/Pt(111) surfaces: unique properties of reduced SnO_x, Phys Chem Chem Phys, 14 (2012) 10207-10214.
[2] C. Dupont, Y. Jugnet, F. Delbecq, D. Loffreda, Mediatory role of tin in the catalytic performance of tailored platinum-tin alloy surfaces for carbon monoxide oxidation, J Catal, 273 (2010) 211-220.
[3] N.D. Gangal, N.M. Gupta, R.M. Iyer, Microcalorimetric Study of the Interaction of CO, O_2 and CO + O_2 with Pt/SnO_2 and SnO_2 Catalysts, J Catal, 126 (1990) 13-25.
[4] Y. Jugnet, D. Loffreda, C. Dupont, F. Delbecq, E. Ehret, F.J.C.S. Aires, B.S. Mun, F.A. Akgul, Z. Liu, Promoter Effect of Early Stage Grown Surface Oxides: A Near-Ambient-Pressure XPS Study of CO Oxidation on PtSn Bimetallics, J Phys Chem Lett, 3 (2012) 3707-3714.
[5] P.N. Ross, Trends in the Bonding of CO to the Surfaces of Pt_3M Alloys (M=Ti, Co, and Sn), J Vac Sci Technol A, 10 (1992) 2546-2550.
[6] J. Singh, R.C. Nelson, B.C. Vicente, S.L. Scott, J.A. van Bokhoven, Electronic structure of alumina-supported monometallic Pt and bimetallic PtSn catalysts under hydrogen and carbon monoxide environment, Phys Chem Chem Phys, 12 (2010) 5668-5677.
[7] J.R. Renzas, W.Y. Huang, Y.W. Zhang, M.E. Grass, D.T. Hoang, S. Alayoglu, D.R. Butcher, F. Tao, Z. Liu, G.A. Somorjai, $Rh_{1-x}Pd_x$ nanoparticle composition dependence in CO oxidation by oxygen: catalytic activity enhancement in bimetallic systems, Phys Chem Chem Phys, 13 (2011) 2556-2562.
[8] F. Tao, M.E. Grass, Y.W. Zhang, D.R. Butcher, F. Aksoy, S. Aloni, V. Altoe, S. Alayoglu, J.R. Renzas, C.K. Tsung, Z.W. Zhu, Z. Liu, M. Salmeron, G.A. Somorjai, Evolution of Structure and Chemistry of Bimetallic Nanoparticle Catalysts under Reaction Conditions, J Am Chem Soc, 132 (2010) 8697-8703.
[9] F. Zheng, S. Alayoglu, V.V. Pushkarev, S.K. Beaumont, C. Specht, F. Aksoy, Z. Liu, J.H. Guo, G.A. Somorjai, In situ study of oxidation states and structure of 4 nm CoPt bimetallic nanoparticles during CO oxidation using X-ray spectroscopies in comparison with reaction turnover frequency, Catal Today, 182 (2012) 54-59.
[10] W.D. Michalak, J.M. Krier, K. Komvopoulos, G.A. Somorjai, Structure Sensitivity in Pt Nanoparticle Catalysts for Hydrogenation of 1,3-Butadiene: In Situ Study of Reaction Intermediates Using SFG Vibrational Spectroscopy, J Phys Chem C, 117 (2013) 1809-1817.
[11] S. Alayoglu, J. Krier, W.D. Michalak, Z. Zhu, E. Gross, G.A. Somorjai, In-situ Surface and Reaction Probe Studies with Model Nanoparticle Catalysts, Acs Catal, 2 (2012) 2250-2258.
[12] Y.N. Xia, Y.J. Xiong, B. Lim, S.E. Skrabalak, Shape-Controlled Synthesis of Metal Nanocrystals: Simple Chemistry Meets Complex Physics?, Angew Chem Int Edit, 48 (2009) 60-103.
[13] K. An, G.A. Somorjai, Size and Shape Control of Metal Nanoparticles for Reaction Selectivity in Catalysis, Chemcatchem, 4 (2012) 1512-1524.
[14] M. Salmeron, R. Schlogl, Ambient pressure photoelectron spectroscopy: A new tool for surface science and nanotechnology, Surface Science Reports, 63 (2008) 169-199.
[15] D.E. Starr, Z. Liu, M. Havecker, A. Knop-Gericke, H. Bluhm, Investigation of solid/vapor interfaces using ambient pressure X-ray photoelectron spectroscopy, Chem Soc Rev, 42 (2013) 5833-5857.

[16] X.D. Wang, J. Stover, V. Zielasek, L. Altmann, K. Thiel, K. Al-Shamery, M. Baumer, H. Borchert, J. Parisi, J. Kolny-Olesiak, Colloidal Synthesis and Structural Control of PtSn Bimetallic Nanoparticles, Langmuir, 27 (2011) 11052-11061.
[17] Y.H. Jo, I. Jung, C.S. Choi, I. Kim, H.M. Lee, Synthesis and characterization of low temperature Sn nanoparticles for the fabrication of highly conductive ink, Nanotechnology, 22 (2011).
[18] S.H. Joo, J.Y. Park, C.K. Tsung, Y. Yamada, P.D. Yang, G.A. Somorjai, Thermally stable Pt/mesoporous silica core-shell nanocatalysts for high-temperature reactions, Nat Mater, 8 (2009) 126-131.
[19] W. Stober, A. Fink, E. Bohn, Controlled Growth of Monodisperse Silica Spheres in Micron Size Range, J Colloid Interf Sci, 26 (1968) 62-66.
[20] S. Ikeda, S. Ishino, T. Harada, N. Okamoto, T. Sakata, H. Mori, S. Kuwabata, T. Torimoto, M. Matsumura, Ligand-free platinum nanoparticles encapsulated in a hollow porous carbon shell as a highly active heterogeneous hydrogenation catalyst, Angew Chem Int Edit, 45 (2006) 7063-7066.
[21] Z. Zhang, J.C. Li, Q. Jiang, Modelling for size-dependent and dimension-dependent melting of nanocrystals, J. Phys. D-Appl. Phys., 33 (2000) 2653-2656.
[22] Y.F. Zhu, J.S. Lian, Q. Jiang, Modeling of the Melting Point, Debye Temperature, Thermal Expansion Coefficient, and the Specific Heat of Nanostructured Materials (vol, 113C, pg 16898, 2009), Journal of Physical Chemistry C, 113 (2009) 19748-19748.
[23] M.E. Grass, P.G. Karlsson, F. Aksoy, M. Lundqvist, B. Wannberg, B.S. Mun, Z. Hussain, Z. Liu, New ambient pressure photoemission endstation at Advanced Light Source beamline 9.3.2, Review of Scientific Instruments, 81 (2010).
[24] H.G. Boyen, A. Ethirajan, G. Kastle, F. Weigl, P. Ziemann, G. Schmid, M.G. Garnier, M. Buttner, P. Oelhafen, Alloy formation of supported gold nanoparticles at their transition from clusters to solids: Does size matter?, Phys Rev Lett, 94 (2005).
[25] C.D. Wagner, L.E. Davis, M.V. Zeller, J.A. Taylor, R.H. Raymond, L.H. Gale, Empirical Atomic Sensitivity Factors for Quantitative-Analysis by Electron-Spectroscopy for Chemical-Analysis, Surf Interface Anal, 3 (1981) 211-225.
[26] D.R. Butcher, M.E. Grass, Z.H. Zeng, F. Aksoy, H. Bluhm, W.X. Li, B.S. Mun, G.A. Somorjai, Z. Liu, In Situ Oxidation Study of Pt(110) and Its Interaction with CO, J Am Chem Soc, 133 (2011) 20319-20325.
[27] A.K. Santra, D.W. Goodman, Catalytic oxidation of CO by platinum group metals: from ultrahigh vacuum to elevated pressures, Electrochim Acta, 47 (2002) 3595-3609.
[28] H. Steininger, S. Lehwald, H. Ibach, On the Adsorption of Co on Pt(111), Surf Sci, 123 (1982) 264-282.
[29] S.M. McClure, M. Lundwall, Z. Zhou, F. Yang, D.W. Goodman, Characterization of Pt/SiO_2 Model Catalysts at UHV and Near Atmospheric Pressures, Catal Lett, 133 (2009) 298-306.
[30] T.H. Lin, G.A. Somorjai, Modulated Molecular-Beam Scattering of CO and NO from Pt(111) and the Stepped Pt(557) Crystal-Surfaces, Surf Sci, 107 (1981) 573-585.
[31] M.M. Schubert, M.J. Kahlich, G. Feldmeyer, M. Huttner, S. Hackenberg, H.A. Gasteiger, R.J. Behm, Bimetallic PtSn catalyst for selective CO oxidation in H_2-rich gases at low temperatures, Phys Chem Chem Phys, 3 (2001) 1123-1131.

[32] M. Boualleg, J.M. Basset, J.P. Candy, V. Caps, J.C. Jumas, S. Norsic, E.A. Quadrelli, L. Veyre, C. Thieuleux, Single-Phase Heterogeneous Pt_3Sn Catalyst Synthesized by Room-Temperature Self-Assembly, Chemcatchem, 4 (2012) 1729-1732.
[33] J.L. Margitfalvi, I. Borbath, M. Hegedus, E. Tfirst, S. Gobolos, K. Lazar, Low-temperature CO oxidation over new types of Sn-Pt/SiO_2 catalysts, J Catal, 196 (2000) 200-204.
[34] E. Merlen, P. Beccat, J.C. Bertolini, P. Delichere, N. Zanier, B. Didillon, Characterization of bimetallic Pt-Sn/Al_2O_3 catalysts: Relationship between particle size and structure, J Catal, 159 (1996) 178-188.
[35] D.R. Schryer, B.T. Upchurch, B.D. Sidney, K.G. Brown, G.B. Hoflund, R.K. Herz, A Proposed Mechanism for Pt/SnO_x-Catalyzed CO Oxidation, J Catal, 130 (1991) 314-317.
[36] P.J. Berlowitz, C.H.F. Peden, D.W. Goodman, Kinetics of Co Oxidation on Single-Crystal Pd, Pt, and Ir, J Phys Chem, 92 (1988) 5213-5221.
[37] A.D. Allian, K. Takanabe, K.L. Fujdala, X. Hao, T.J. Truex, J. Cai, C. Buda, M. Neurock, E. Iglesia, Chemisorption of CO and Mechanism of CO Oxidation on Supported Platinum Nanoclusters, J Am Chem Soc, 133 (2011) 4498-4517.
[38] F. Gao, Y. Wang, Y. Cai, D.W. Goodman, CO Oxidation on Pt-Group Metals from Ultrahigh Vacuum to Near Atmospheric Pressures. 2. Palladium and Platinum, J Phys Chem C, 113 (2009) 174-181.
[39] K. Grass, H.G. Lintz, The kinetics of carbon monoxide oxidation on tin(IV) oxide supported platinum catalysts, J Catal, 172 (1997) 446-452.
[40] J.Y. Park, Y. Zhang, S.H. Joo, Y. Jung, G.A. Somorjai, Size effect of RhPt bimetallic nanoparticles in catalytic activity of CO oxidation: Role of surface segregation, Catal Today, 181 (2012) 133-137.
[41] W.D. Michalak, G.A. Somorjai, Catalysis in Energy: Correlating Composition, Electronic Structure and Nanostructure with Activity and Selectivity using Spectroscopy under Working Conditions (Perspective) Top Catal, to be published (2013).
[42] A. Haghofer, D. Ferri, K. Föttinger, G. Rupprechter, Who Is Doing the Job? Unraveling the Role of Ga_2O_3 in Methanol Steam Reforming on Pd2Ga/Ga2O3, Acs Catal, 2 (2012) 2305-2315.
[43] The inelasitc mean free path calculation was performed using the applet at http://www.lasurface.com/xps/imfpgrapher.php#, which is based on the modeling functions from two publications: P.J.Cumpson and M.P. Seah, Elastic Scattering corrections in AES and XPS. II Estimating Attenuation Lengths and Conditions Required for their Valid Use in Overlayer/Substrate Experiments and M.P.Seah and W.A. Dench, Quantitative Electron Spectroscopy of Surfaces: A Standard Data Base for Electron Inelastic Mean Free Paths in Solids.
[44] A.H. Haner, P.N. Ross, U. Bardi, A. Atrei, Surface-Composition Determination of Pt-Sn Alloys by Chemical Titration with Carbon-Monoxide, J Vac Sci Technol A, 10 (1992) 2718-2722.
[45] D.I. Jerdev, B.E. Koel, Oxidation of ordered Pt-Sn surface alloys by O_2, Surf Sci, 492 (2001) 106-114.
[46] J.M. Themlin, M. Chtaib, L. Henrard, P. Lambin, J. Darville, J.M. Gilles, Characterization of Tin Oxides by X-Ray-Photoemission Spectroscopy, Phys Rev B, 46 (1992) 2460-2466.
[47] P. Depadova, M. Fanfoni, R. Larciprete, M. Mangiantini, S. Priori, P. Perfetti, A Synchrotron-Radiation Photoemission-Study of the Oxidation of Tin, Surf Sci, 313 (1994) 379-391.

[48] B. Hammer, Y. Morikawa, J.K. Norskov, CO chemisorption at metal surfaces and overlayers, Phys Rev Lett, 76 (1996) 2141-2144.
[49] R. Ferrando, J. Jellinek, R.L. Johnston, Nanoalloys: From theory to applications of alloy clusters and nanoparticles, Chem Rev, 108 (2008) 845-910.
[50] J. Luo, C. Xu, XPS Examination of Tin Oxide on Float Glass-Surface, J Non-Cryst Solids, 119 (1990) 37-40.
[51] W. Eberhardt, P. Fayet, D.M. Cox, Z. Fu, A. Kaldor, R. Sherwood, D. Sondericker, Photoemission from Mass-Selected Monodispersed Pt Clusters, Physical Review Letters, 64 (1990) 780-784.
[52] N. Isomura, X.Y. Wu, H. Hirata, Y. Watanabe, Cluster size dependence of Pt core-level shifts for mass-selected Pt clusters on TiO_2(110) surfaces, J Vac Sci Technol A, 28 (2010) 1141-1144.
[53] Y. Uemura, Y. Inada, K.K. Bando, T. Sasaki, N. Kamiuchi, K. Eguchi, A. Yagishita, M. Nomura, M. Tada, Y. Iwasawa, Core-Shell Phase Separation and Structural Transformation of Pt_3Sn Alloy Nanoparticles Supported on gamma-Al_2O_3 in the Reduction and Oxidation Processes Characterized by In Situ Time-Resolved XAFS, J Phys Chem C, 115 (2011) 5823-5833.
[54] L.K. Ono, B. Yuan, H. Heinrich, B.R. Cuenya, Formation and Thermal Stability of Platinum Oxides on Size-Selected Platinum Nanoparticles: Support Effects, J Phys Chem C, 114 (2010) 22119-22133.
[55] M. Batzill, D.E. Beck, B.E. Koel, Self-organized molecular-sized, hexagonally ordered SnOx nanodot superlattices on Pt(111), Appl Phys Lett, 78 (2001) 2766-2768.
[56] C. Xu, B.E. Koel, Probing the Modifier Precursor State - Adsorption of CO on Sn/Pt(111) Surface Alloys, Surf Sci, 304 (1994) L505-L511.
[57] R.K. Herz, A. Badlani, D.R. Schryer, B.T. Upchurch, Two-Component Catalysts for Low-Temperature CO Oxidation: A Monte Carlo Study, J Catal, 141 (1993) 219-238.
[58] A. Boulahouache, G. Kons, H.G. Lintz, P. Schulz, Oxidation of carbon monoxide on platinum-tin dioxide catalysts at low temperatures, Applied Catalysis A: General, 91 (1992) 115-123.
[59] J.F. Weaver, T.J. Campbell, G.B. Hoflund, G.N. Salaita, Oxidation of polycrystalline tin by hyperthermal atomic oxygen: an investigation using electron energy-loss spectroscopy, J Electron Spectrosc, 106 (2000) 81-91.
[60] G.B. Hoflund, G.R. Corallo, Electron-Energy-Loss Study of the Oxidation of Polycrystalline Tin, Phys Rev B, 46 (1992) 7110-7120.
[61] N.A. Saliba, Y.L. Tsai, B.E. Koel, Oxidation of ordered Sn/Pt(111) surface alloys and thermal stability of the oxides formed, J Phys Chem B, 103 (1999) 1532-1541.
[62] Y. Uemura, Y. Inada, K.K. Bando, T. Sasaki, N. Kamiuchi, K. Eguchi, A. Yagishita, M. Nomura, M. Tada, Y. Iwasawa, In situ time-resolved XAFS study on the structural transformation and phase separation of Pt3Sn and PtSn alloy nanoparticles on carbon in the oxidation process, Phys Chem Chem Phys, 13 (2011) 15833-15844.

Supplement to Chapter 6

Morphology of Pt and PtSn nanoparticles

Pt and PtSn nanoparticles that were encapsulated in a porous SiO_2 shell were imaged using a transmission electron microscope prior to treatment. Images shown in Figure S.6.1(a) and (b) indicate the Pt and PtSn nanoparticles (black dots), respectively. The alloy nanoparticles cannot be differentiated from pure Pt nanoparticles using this technique. The inset shows the particle size histograms for the particles measured, which indicates a ~2 nm average particle size for both Pt and PtSn catalysts. The SiO_2 shell inhibits sintering of the PtSn nanoparticles (also for Pt, but not shown). An image of the PtSn nanoparticles that were reclaimed after calcination and reaction procedures is shown with a histogram in Figure S.6.1(c).

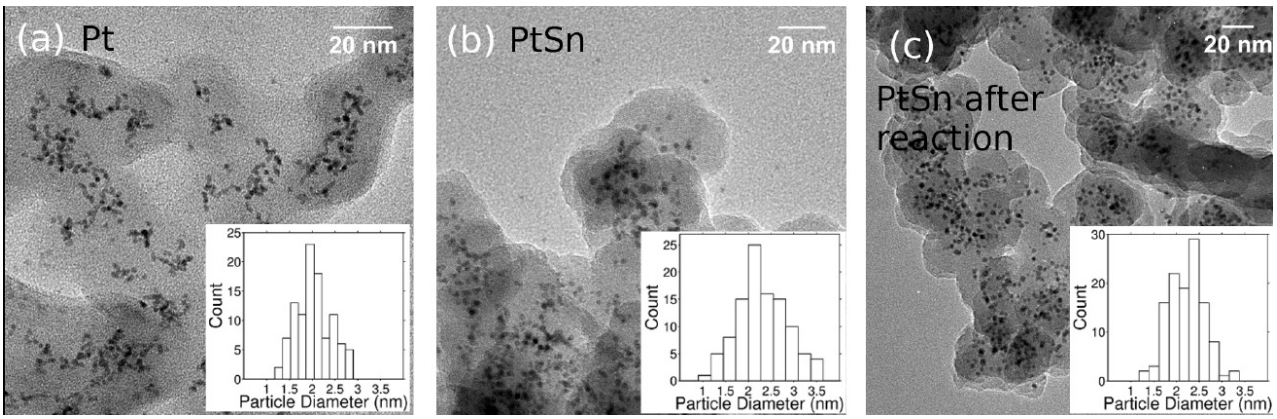

Figure S.6.1: Colloidally prepared Pt nanoparticles. The nanoparticles shown are encapsulated in a porous silica shell to inhibit nanoparticle sintering during heat treatments. (b) Colloidally prepared PtSn nanoparticles encapsulated in silica. (c) PtSn nanoparticles after treatment and reaction studies. The nanoparticle morphology is maintained. Histogram insets show the average and deviation of the particle size in nanometers.

Reaction order in CO for CO_2 formation

The rate of CO_2 formation versus P_{CO} is shown in Figure S.6.2 for the Pt (red) and PtSn (blue) catalysts. At $P_{CO} < 40$ Torr, the $n_{CO,Pt}$ and $n_{CO,PtSn}$ determined from the slope of a ln-ln plot is ~8. Apparent reaction orders > 8 are often related to mass transfer limitations in the gas phase [1]. In this experiment, the Pt and PtSn catalysts are initially covered with O. When CO molecules approach the O-covered Pt surface, the reaction proceeds rapidly and leaves a near surface gas boundary layer that is starved of CO. In addition, when CO_2 is formed two sites become available for further CO adsorption. This autocatalytic behavior has also been observed to provide reaction orders that are much greater (and lower) than expected for an elementary reaction step.[2] When $P_{CO} > 40$ Torr, the reaction rate reaches a maximum and further increase in P_{CO} causes r to decline because CO blocks Pt sites. At this P_{CO}, the O adsorbed on the surface was likely displaced by CO. For the Pt catalysts, we determined a $n_{CO,Pt} = -3.5$ in the pressure range $40 < P_{CO} < 65$ Torr and a $n_{CO,Pt} = -1$ in the pressure range of $65 < P_{CO} < 100$ Torr. A reaction order < -2 was suggested for autocatalytic reactions and growth and mutual inhibition processes [2]. A negative first-order behavior in CO is in agreement with previous reports, which point to CO inhibition of O_2 adsorption and CO_2 formation [3-7]. The PtSn catalysts exhibit a $n_{CO,PtSn} = -1.5$ in the pressure range of $40 < P_{CO} < 100$ Torr. This value suggests a complex reaction network involving CO, but there is an overall inhibition effect. We expect that the Pt surface is still active for O_2 adsorption and CO continues to inhibit O_2 adsorption in the same manner as predicted on the pure Pt catalysts.

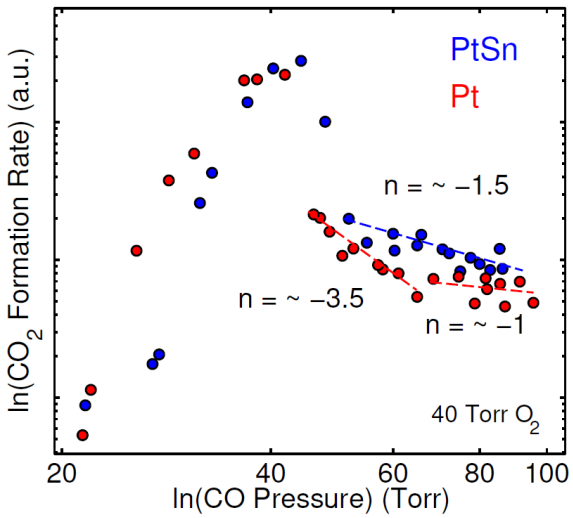

Figure S.6.2: Plot of the ln(CO_2 formation rate) vs ln(P_{CO}) gives reaction order in CO for Pt and PtSn catalysts.

***In vacuo* X-ray photoelectron spectroscopy of pure Sn and Pt nanoparticles as reference to PtSn**

The different chemical states of Pt, Sn, and O were characterized for pure Pt, pure Sn, and PtSn nanoparticles *ex-situ* under vacuum conditions using a lab-based XPS system. A comparison of the Pt 4f, Sn $3d_{5/2}$ and O1s spectra for the three nanoparticles after a reduction treatment at 350 ˚C in 1 atm of H_2 and transfer through ambient conditions to the analysis chamber are shown in Figure S.6.3.

For each nanoparticle system, both oxygen and carbon were observed on the surface; however, since the carbon signal was similar across the nanoparticles, we do not display the spectra. The Pt 4f doublet (variations of green), Sn $3d_{5/2}$ (variations of blue), and O 1s (variations of magenta) core-level photoemission spectra taken *in vacuo* at room temperature are shown in Figure S.6.3. The spectra are organized horizontally by nanoparticle type with Pt ((a) Pt 4f and (b) O1s), PtSn

((c) Pt 4f, (d) Sn $3d_{5/2}$ and (e) O1s), and Sn (Sn $3d_{5/2}$ (f) and O1s (g)) nanoparticles. All nanoparticle samples were treated *ex situ* in H_2 for 20 minutes at 325 ˚C in a tube furnace. The XPS spectra were obtained using an Al Kα X-ray source with a photon energy, $h\nu$ = 1486.6 eV. The binding energies were calibrated using the Au $4f_{7/2}$ feature (from the substrate) at a binding energy of 84 eV [8].

Pure Pt nanoparticles

The XPS spectra in Figures S.6.3(a) and (b) display the chemical states of Pt and O, respectively, on the Pt nanoparticles. The Pt 4f orbitals are described by two features (for each hybrid state). For all datasets, we used a constant spin-orbit splitting value of 3.3 eV, a branching ratio of 0.75 for 5/2:7/2 states, and a unique full width at half maximum (FWHM) value for each chemical state. The dominant core-level feature in the Pt 4f spectra is located at 70.8 eV and is assigned to metallic Pt (Pt^0).[9] The peak locations and FWHM of all core-level features described herein are presented in Table 1. The other feature in the Pt 4f spectra is located at 72.5 eV. We assign this relatively broad feature to a combination of states including Pt bound to chemisorbed CO, O, and Pt-carbonyl from the polyvinylpyrrolidone (PVP) capping agent (Pt-CO/O).[9, 10] The feature does not include Pt oxides, which exhibit a $Pt_{7/2}$ core-level feature that appears above 73 eV [5, 9, 11, 12].

The O 1s orbitals are described by two features at 531.4 and 532.8 eV. The origin of these peaks is uncertain and we do not attempt to make definitive assignments. Nonetheless, they may be related to the carbonyl group of the PVP capping agent.

Pure Sn nanoparticles

The XPS spectra in Figures S.6.3(f) and (g) display the chemical states of Sn and O, respectively, in the Sn nanoparticles. The Sn $3d_{5/2}$ orbital is described by two oxidic states (Sn^{2+} and Sn^{4+}) and a metallic state (Sn^0). The major feature in the spectrum at 487.3 eV corresponds to a Sn^{4+} oxide state. The Sn^{2+} feature is located 0.9 eV below the Sn^{4+} feature, which is in general agreement with previous reports [10, 13-17]. The small feature at 485.2 eV is assigned to metallic Sn (Sn^0) and resides within the previously reported range of binding energies of 484.7 – 485.8 eV [10, 13-17]. While this feature is small in the reference sample, it becomes significant after higher temperature reduction treatments. The locations of these features are shifted to higher energies than reported previously for bulk Sn oxides [14, 18]. The shift is likely a property of the nanoparticle's dimensions [8, 19, 20]. The composition of the nanoparticles comprises 75 % SnO_2, 22% SnO, and 4% Sn^0.

The O 1s signal from the Sn surface required an additional feature compared to the Pt nanoparticles. Features appear at 530.1 eV, 531.7eV, and 533.0 eV. We assign the feature at 530.1 eV to O in a SnO_x environment, which is consistent to previous reports [10, 13-17]. The other two features likely have similar origins as the features observed on Pt.

Comparison to the PtSn nanoparticles

The XPS spectra in Figures S.6.3(c), (d), and (e) display the chemical states of Pt, Sn, and O, respectively, on the PtSn nanoparticles. The Pt, Sn, and O spectra each have features that were observed on the reference samples that reflect Sn^0, Sn-oxides, metallic Pt, and Pt-CO/O; however, a new feature appears in each spectrum that is shifted to higher binding energies with

respect to the metallic component. We assign the feature at 71.4 eV and 485.8 eV to Pt and Sn atoms that are in an alloy environment ($Pt^{(Sn)}$ and $Sn^{(Pt)}$, respectively). A core-level shift of Pt and Sn is consistent with the proposed electron exchange between the Pt and Sn atoms in an alloy environment.

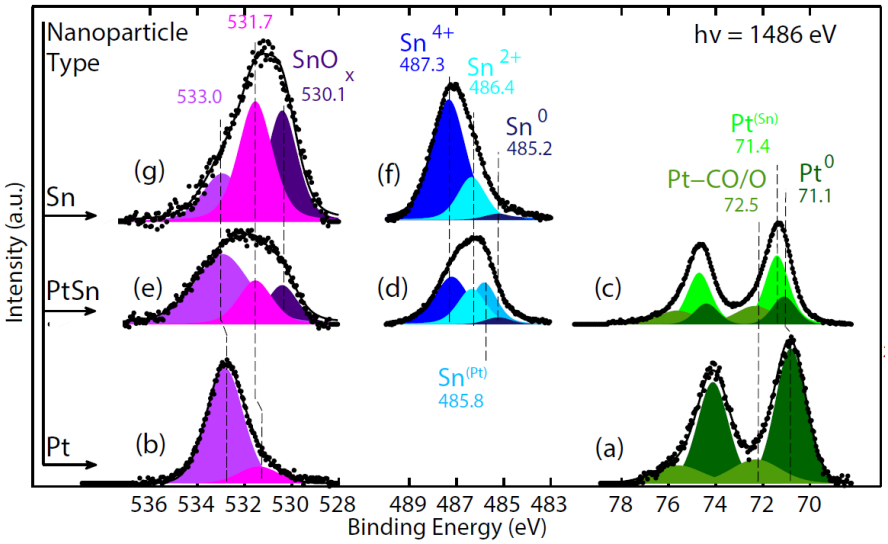

Figure S.6.3: *Ex situ* X-ray photoelectron spectra of Pt 4f, Sn $3d_{5/2}$, and O 1s orbitals for colloidally-prepared Pt (bottom), Sn (top), and PtSn (middle) nanoparticles after a 20 min at 240 ˚C in H_2. The spectra were obtained *in vacuo* with a photon energy of 1486 eV. The spectra are deconvoluted into features with unique chemical shifts that represent different chemical environments. The PtSn nanoparticles have similar chemical states as found in the pure reference nanoparticles with the exception of a feature that is shifted to higher binding energy in the Sn and Pt spectra that corresponds to an alloy phase.

***In situ* ambient pressure X-ray photoelectron spectroscopy showing the evolution of the Sn chemical states during pre-treatment**

The chemical environment of the Sn in the PtSn nanoparticle catalysts was evaluated by monitoring photoemission of Sn $3d_{5/2}$ core-level electrons using APXPS. The spectra were measured using a photon energy, hv = 740 eV, which provides a kinetic energy of photoelectrons of ~250 eV and an inelastic mean free path (IMFP) of 7 Å in a pure Sn environment [21].

The chemical environment of Sn in the PtSn catalysts during heat treatment *in vacuo* from 200 to 356 ˚C followed by exposure to 100 mTorr of H_2 at 370 ˚C is shown in XPS spectra in Figure S.6.4(a)-(e) These spectra reflect the PtSn catalysts during the first heat treatment after deposition of nanoparticles from the colloid onto the Au-coated Si wafer substrate. The binding energies were calibrated using photoemission from the Au $4f_{7/2}$ core-level with a binding energy of 84 eV[8]. In addition, the intensity of the spectra was normalized by the Au $4f_{7/2}$ intensity at the constant photon energy to account for signal attenuation due to X-ray absorption by ambient gases. During fitting, the position and FWHM of the Sn $3d_{5/2}$ features were held constant across different gas environments; only the area was unconstrained.

The progression of the chemical states as the PtSn nanoparticles were heated in vacuum to 356 ˚C is shown in Figure S.6.5. During pre-treatment, the concentration of oxide features diminished at the benefit of the metallic components (Sn^0 and $Sn^{(Pt)}$). At a temperature of 356 ˚C, the Sn^{2+} feature became small, while the Sn^{4+} contributed 11% of the overall Sn signal. When the nanoparticles were exposed to 100 mTorr H_2 at 370 ˚C, the concentration of Sn^{2+} became negligible. The fluctuations in the different components of Sn indicate the reducibility of Sn

atoms in the nanoparticles. In contrast, pure Sn nanoparticles exhibited predominantly Sn^{4+} and Sn^{2+} following reducing treatments (c.f. Figure S.6.3).

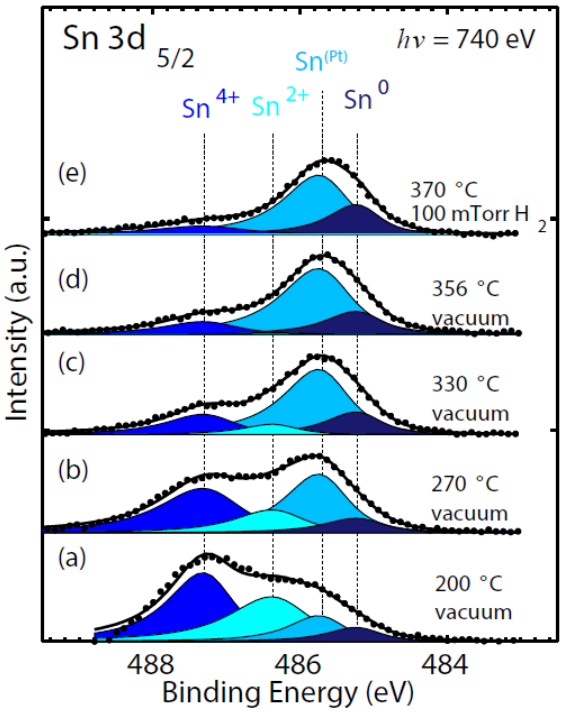

Figure S.6.4: Evolution of the *in situ* Sn $3d_{5/2}$ ambient pressure X-ray photoelectron spectra for the PtSn nanoparticle catalysts during heating pretreatment conditions in vacuum at (a) 200 ˚C, (b) 270 ˚C, (c) 330 ˚C, and (d) 356 ˚C, and (e) in 100 mTorr H_2 at 370 ˚C. The Sn spectra exhibits four contributions that are determined by unique chemical shifts: Sn^{4+} (487.3 eV), Sn^{2+} (486.4 eV), Sn in a Pt environment ($Sn^{(Pt)}$, 485.8 eV), and Sn^0 (485.3 eV). The percentage of each Sn chemical state over the pre-treatment course is shown in Figure S.6.5.

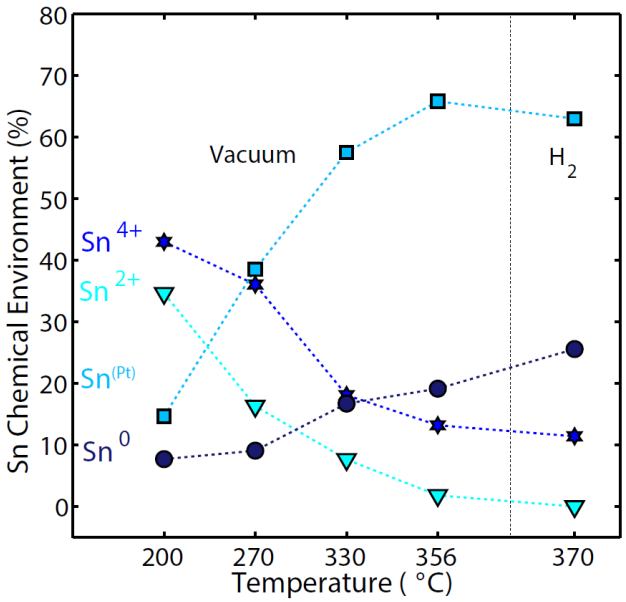

Figure S.6.5: Progression of the different Sn chemical environments in the PtSn nanoparticle catalysts during pretreatment under vacuum and H_2 atmospheres measured using ambient pressure X-ray photoelectron spectroscopy. Each trend line corresponds to a feature in the XPS spectra in Figure S.6.4. The as-prepared 2 nm PtSn catalyst comprised Sn^{4+} and Sn^{2+} oxides that were reduced during heat treatment.

***In situ* ambient pressure X-ray photoelectron spectra for O on the PtSn nanoparticle catalysts**

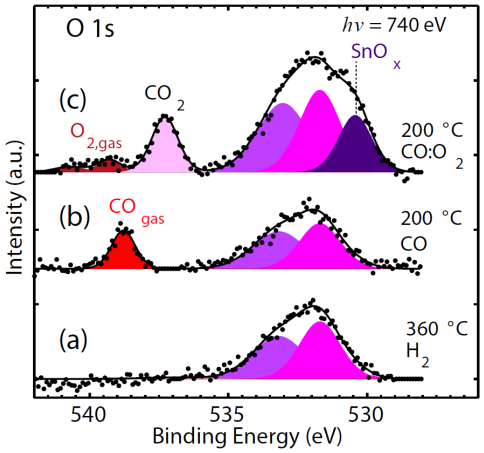

Figure S.6.6: *In situ* O 1s ambient pressure X-ray photoelectron spectra for O on the PtSn nanoparticle catalysts during heating (a) 100 mTorr H_2 at 370 ˚C, (b) 100 mTorr CO at 200 ˚C, (c) 100 mTorr CO and 40 mTorr O_2 at 200 ˚C.

***In situ* ambient pressure X-ray photoelectron spectroscopy showing the evolution of the Sn chemical states during post-treatment reducing conditions**

The APXPS spectra during post-reaction reducing treatments during exposure of 100 mTorr of H_2 at 360 ˚C is shown in Figure S.6.7(b)-(g) over the course of an hour. In comparison, the chemical states of Sn during reaction conditions are shown in Figure S.6.7(a). When switching to reducing conditions, the decrease in Sn^{2+} content prompted an increase in all three other states of Sn. The transformation from Sn^{2+} to Sn^0 and $Sn^{(Pt)}$ occurred over the entire hour long time period. The progression of the different chemical states of Sn is shown in Figure S.6.8.

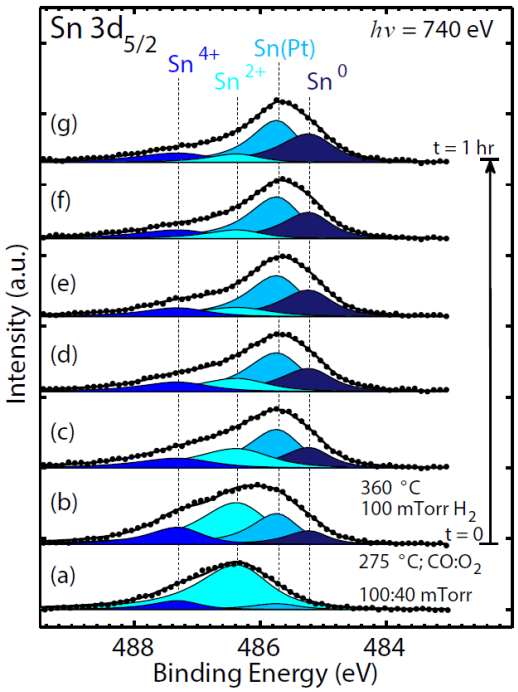

Figure S.6.7: Evolution of the *in situ* Sn $3d_{5/2}$ ambient pressure X-ray photoelectron spectra for the PtSn nanoparticle catalysts during (a) CO oxidation reaction conditions at 275 ˚C, and (b)-(g) reducing post-treatment conditions at 360 ˚C over the course of 1 h. The percentage of each Sn chemical state over the post-treatment course is shown in Figure S.6.8.

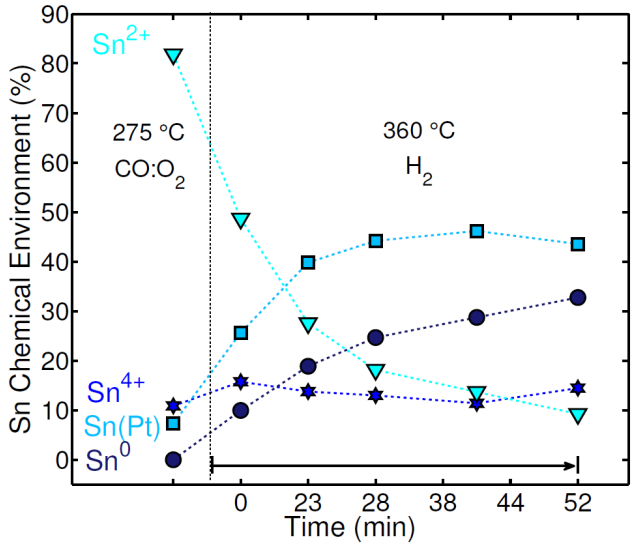

Figure S.6.8: Trends of the different Sn chemical environments in the 2nm PtSn nanoparticle catalysts following CO oxidation reaction at 275 ˚C. At time equal to zero, the sample was exposed to 100 mTorr H_2 at 360 ˚C. Each trend line corresponds to a feature in the APXPS spectra in Figure S.6.7. Under reaction atmospheres, the catalyst surface was comprised of Sn^{2+}, Sn^{4+}, and $Sn^{(Pt)}$. During the post-treatment reduction, Sn^{2+} was readily reduced and the content of $Sn^{(Pt)}$ and Sn^{0} increased.

References

[1] R.H. Venderbosch, W. Prins, W.P.M. van Swaaij, Platinum catalyzed oxidation of carbon monoxide as a model reaction in mass transfer measurements, Chem Eng Sci, 53 (1998) 3355-3366.
[2] D. Lavabre, V. Pimienta, G. Levy, J.C. Micheau, Reversible, Mixed 1st-Order and 2nd-Order and Autocatalytic Reactions as Particular Cases of a Single Kinetic Rate Law, J Phys Chem-Us, 97 (1993) 5321-5326.
[3] A.D. Allian, K. Takanabe, K.L. Fujdala, X. Hao, T.J. Truex, J. Cai, C. Buda, M. Neurock, E. Iglesia, Chemisorption of CO and Mechanism of CO Oxidation on Supported Platinum Nanoclusters, J Am Chem Soc, 133 (2011) 4498-4517.
[4] T.H. Lin, G.A. Somorjai, Modulated Molecular-Beam Scattering of Co and No from Pt(111) and the Stepped Pt(557) Crystal-Surfaces, Surf Sci, 107 (1981) 573-585.
[5] J. Singh, R.C. Nelson, B.C. Vicente, S.L. Scott, J.A. van Bokhoven, Electronic structure of alumina-supported monometallic Pt and bimetallic PtSn catalysts under hydrogen and carbon monoxide environment, Phys Chem Chem Phys, 12 (2010) 5668-5677.

[6] F. Gao, S.M. McClure, Y. Cai, K.K. Gath, Y. Wang, M.S. Chen, Q.L. Guo, D.W. Goodman, CO oxidation trends on Pt-group metals from ultrahigh vacuum to near atmospheric pressures: A combined in situ PM-IRAS and reaction kinetics study, Surf Sci, 603 (2009) 65-70.
[7] F. Gao, Y. Wang, Y. Cai, D.W. Goodman, CO Oxidation on Pt-Group Metals from Ultrahigh Vacuum to Near Atmospheric Pressures. 2. Palladium and Platinum, J Phys Chem C, 113 (2009) 174-181.
[8] H.G. Boyen, A. Ethirajan, G. Kastle, F. Weigl, P. Ziemann, G. Schmid, M.G. Garnier, M. Buttner, P. Oelhafen, Alloy formation of supported gold nanoparticles at their transition from clusters to solids: Does size matter?, Phys Rev Lett, 94 (2005).
[9] D.R. Butcher, M.E. Grass, Z.H. Zeng, F. Aksoy, H. Bluhm, W.X. Li, B.S. Mun, G.A. Somorjai, Z. Liu, In Situ Oxidation Study of Pt(110) and Its Interaction with CO, J Am Chem Soc, 133 (2011) 20319-20325.
[10] Y. Jugnet, D. Loffreda, C. Dupont, F. Delbecq, E. Ehret, F.J.C.S. Aires, B.S. Mun, F.A. Akgul, Z. Liu, Promoter Effect of Early Stage Grown Surface Oxides: A Near-Ambient-Pressure XPS Study of CO Oxidation on PtSn Bimetallics, J Phys Chem Lett, 3 (2012) 3707-3714.
[11] L.K. Ono, B. Yuan, H. Heinrich, B.R. Cuenya, Formation and Thermal Stability of Platinum Oxides on Size-Selected Platinum Nanoparticles: Support Effects, J Phys Chem C, 114 (2010) 22119-22133.
[12] Y. Uemura, Y. Inada, K.K. Bando, T. Sasaki, N. Kamiuchi, K. Eguchi, A. Yagishita, M. Nomura, M. Tada, Y. Iwasawa, Core-Shell Phase Separation and Structural Transformation of Pt_3Sn Alloy Nanoparticles Supported on gamma-Al_2O_3 in the Reduction and Oxidation Processes Characterized by In Situ Time-Resolved XAFS, J Phys Chem C, 115 (2011) 5823-5833.
[13] P. Depadova, M. Fanfoni, R. Larciprete, M. Mangiantini, S. Priori, P. Perfetti, A Synchrotron-Radiation Photoemission-Study of the Oxidation of Tin, Surf Sci, 313 (1994) 379-391.
[14] S. Axnanda, W.P. Zhou, M.G. White, CO oxidation on nanostructured SnO_x/Pt(111) surfaces: unique properties of reduced SnO_x, Phys Chem Chem Phys, 14 (2012) 10207-10214.
[15] D.I. Jerdev, B.E. Koel, Oxidation of ordered Pt-Sn surface alloys by O_2, Surf Sci, 492 (2001) 106-114.
[16] A.H. Haner, P.N. Ross, U. Bardi, A. Atrei, Surface-Composition Determination of Pt-Sn Alloys by Chemical Titration with Carbon-Monoxide, J Vac Sci Technol A, 10 (1992) 2718-2722.
[17] J.M. Themlin, M. Chtaib, L. Henrard, P. Lambin, J. Darville, J.M. Gilles, Characterization of Tin Oxides by X-Ray-Photoemission Spectroscopy, Phys Rev B, 46 (1992) 2460-2466.
[18] J. Luo, C. Xu, XPS Examination of Tin Oxide on Float Glass-Surface, J Non-Cryst Solids, 119 (1990) 37-40.
[19] W. Eberhardt, P. Fayet, D.M. Cox, Z. Fu, A. Kaldor, R. Sherwood, D. Sondericker, Photoemission from Mass-Selected Monodispersed Pt Clusters, Physical Review Letters, 64 (1990) 780-784.
[20] N. Isomura, X.Y. Wu, H. Hirata, Y. Watanabe, Cluster size dependence of Pt core-level shifts for mass-selected Pt clusters on TiO2(110) surfaces, J Vac Sci Technol A, 28 (2010) 1141-1144.
[21] The inelasitc mean free path calculation was performed using the applet at http://www.lasurface.com/xps/imfpgrapher.php#, which is based on the modeling functions from two publications: P.J.Cumpson and M.P. Seah, Elastic Scateering corrections in AES and XPS.

II Estimating Attenuation Lengths and Conditions Required for their Valid Use in Overlayer/Substrate Experiments, and M.P.Seah and W.A. Dench, Quantitative Electron Spectroscopy of Surfaces: A standard Data Base for Electron Inelastic Mean Free Paths in Solids.

Chapter 7: Promotion of Hydrogenation of Organic Molecules by Incorporating Iron into Platinum Nanoparticle Catalysts: Displacement of Less Active Reaction Intermediates

7.1 Introduction

Platinum and its alloys have long been used as catalysts in the chemical industry.[1-3] Although nano-sized Pt particles loaded on various types of supports have been used in heterogeneous catalysis for many decades, it was not until the synthetic capability to control size, shape and composition of nanoparticles was developed that the correlation between structural properties and chemical properties of Pt-based nanoparticles was carefully examined.[1,4-7] Many interesting effects in chemical catalysis posed by the size, shape and composition of Pt-based nanoparticles have been observed, which is essential towards understanding the structure-property relationship in model catalyst systems as well as advancing further optimization of catalytic activity and selectivity for challenging reactions. [8-11]

Pt-Fe bimetallic nanoparticles are promising materials for catalysis, data-storage, permanent-magnet and biomedical applications.[12] Incorporation of Fe into the structure of Pt nanoparticles could enhance the catalytic performance for certain reactions.[13-16] For example, Pt-Fe bimetallic nanoparticles have been observed to be better catalysts than Pt nanoparticles for both the methanol oxidation reaction and the oxygen reduction reaction in direct methanol fuel cells.[13] It has also been reported that Pt-Fe bimetallic nanoparticles exhibited considerably higher activity and more desirable selectivity than Pt nanoparticles in catalysis of reactions such as selective CO oxidation in hydrogen and cinnamaldehyde hydrogenation.[14-16] Understanding of such enhancement in catalytic performance requires synthetic control of the size, shape and

composition of the bimetallic nanoparticles as well as characterizations of chemical states on the catalyst surface under reaction conditions.

We developed a synthesis strategy that could readily produce 2 nm Pt-Fe bimetallic nanoparticles with tunable compositions by reduction of platinum (II) acetylacetonate and iron (II) acetylacetonate in ethylene glycol solution in the presence of polyvinylpyrrolidone (PVP). The obtained 2 nm Pt-Fe nanoparticles were tested for catalysis of ethylene hydrogenation reaction. It was observed that the activity was highly dependent on the composition of the nanoparticles. In particular, the PtFe nanoparticles showed ~3 times higher activity at 25 ^{o}C and considerably lower activation energy than the Pt nanoparticles with a similar size. Sum frequency generation (SFG) vibrational spectroscopy under reaction conditions suggested less adsorption of ethylidyne (a relatively inactive reaction intermediate compared to di-σ-ethylene) and more of di-σ-ethylene on the PtFe nanoparticle surface than on the Pt surface. Negligible ethylene intermediate adsorption on the $PtFe_3$ nanoparticle surface was observed. The promotion of ethylene hydrogenation on PtFe was thus believed to be due to Fe incorporation into Pt which decreased the surface concentration of less active intermediates. Similarly, the turnover rate of cyclohexene hydrogenation was increased on the PtFe nanoparticles than the Pt. Ambient-pressure X-ray photoelectron spectroscopy (AP-XPS) study of the PtFe nanoparticles revealed that while the Pt atoms remained largely metallic, the oxidation states of the Fe atoms were responsive to the gas atmosphere as well as the probing depth.

7.2 Experimental

To synthesize the Pt-Fe bimetallic nanoparticles, a total amount of ~0.2 mmol of platinum (II) acetylacetonate and iron (II) acetylacetonate with various designed ratios (9:1, 3:1, 1:1, and 1:3) were dissolved in 5 mL of ethylene glycol together with 55 mg of PVP (M_w = 55,000). The solution was then heated to 200 ^oC in an oil bath and held at that temperature for 5 min under Argon atmosphere. Cooled to room temperature, the resulting nanoparticles were precipitated with 45 mL of acetone and re-dispersed in 10 mL of ethanol. The nanoparticles were repeatedly washed by precipitating with hexane, centrifuging, and re-dispersing in ethanol before use. In control experiments, either platinum (II) acetylacetonate or iron (II) acetylacetonate was used as the sole precursor, while the other conditions were kept unchanged.

To synthesize the 2 nm Pt nanoparticles, 100 mg of NaOH was dissolved in 5 ml of ethylene glycol and the solution was added to another 5 mL of ethylene glycol solution containing 80 mg of $H_2PtCl_6 \cdot xH_2O$ (~0.2 mmol). The mixture was heated to 160 ^oC in an oil bath and held at that temperature for 2 hr under Argon atmosphere. The resulting nanoparticles were precipitated with 2 mL of 2 M HCl solution and re-dispersed in ethanol with 100 mg of PVP (M_w = 55,000). The nanoparticles were repeatedly washed by precipitating with hexane, centrifuging, and re-dispersing in ethanol before use.

The catalyst samples for ethylene hydrogenation reaction were prepared by depositing Langmuir-Blodgett (LB) monolayer films of the nanoparticles on 500 nm thermally grown SiO_2 on top of Si chips. The SiO_2 substrates were pre-treated in Piranha solution for at least 30 min to make the surface hydrophilic. Nanoparticles were dispersed in chloroform prior to LB film

deposition. The nanoparticle chloroform suspension was then deposited on to a water surface and at least 30 min was allowed for the organic solvent to evaporate. The film was then compressed, and the increase in surface pressure was monitored. When the desired surface pressure between 20 and 30 N/m was reached, the SiO_2 substrate was pulled up through the water at a rate of 1.5 mm/min, and a monolayer film of nanoparticles was deposited onto the substrate. A SiO-coated Cu TEM grid was dropped on the compressed film and retrieved in about 10 seconds to prepare the sample that was imaged to estimate the nanoparticle density of the LB film. For some types of nanoparticles that were not well dispersed in pure chloroform, a mixed solvent of ethanol and chloroform was used.

The catalysts for cyclohexene hydrogenation reactions were prepared by drop-casting ethanol dispersions of nanoparticles on Si chips. Number of active sites for each catalyst was estimated from ethylene hydrogenation reactions with known turnover frequency listed in Figure 7.2.

The reactions were carried out in a batch reactor equipped with a boron nitride substrate heater and a metal bellows recirculation pump for gas mixing. For ethylene hydrogenation reaction, the reactor was filled in sequence with 100 Torr of hydrogen, 10 Torr of ethylene and 660 Torr of helium at a certain temperature. For cyclohexene hydrogenation reaction, the reactor was filled with 10 Torr of cyclohexene, 200 Torr of hydrogenation and 560 Torr of helium at 20 ^{o}C. Total conversion was kept below 10% in order to assess the initial reaction rates. The products were detected by a gas chromatography with a thermal conductivity detector (ethylene hydrogenation) or a flame ionization detector (cyclohexene hydrogenation).

XPS samples were prepared by depositing LB films of the nanoparticles onto Si substrates. AP-XPS experiments were performed on Scienta 4000 HiPP workstation at Beamline 9.3.2 at Advanced Light Source in Lawrence Berkeley National Laboratory. Pt 4f and Fe 3p core level spectra were acquired with X-ray energies of 370, 490, and 750 eV to monitor the atomic fractions and the oxidation state distributions of the two elements. At certain excitation energy, the probing depths for Pt and Fe were approximately the same, because the Pt 4f and Fe 3p photoelectrons had similar kinetic energies as the Pt 4f and 3p electrons had similar binding energies. All series of XPS spectra were quantitatively analyzed by deconvoluting Voigt-type line-shapes, preceded by subtracting the Shirley-type background.

Samples for SFG vibrational spectroscopy were prepared by depositing LB films of nanoparticles onto polished fused silica equilateral (60°) prisms (ISP Optics). A mode-locked Nd:YAG dye laser (Continuum D-20) with 1064 nm output, 20 Hz repetition, and 20 ps pulse width was used for all SFG experiments. A frequency-doubling crystal (BBO) was used to generate a visible beam (532 nm) from the fundamental 1064 nm beam. An optical parametric generator and optical parametric amplifier produced tunable infrared (2740−3090 cm^{-1}). Visible and infrared beams of 150 μJ power were overlapped at the base of the prism at angles of 63 and 48°, respectively, to achieve total internal reflection. Experiments were performed in the *ppp* polarization combination. A photomultiplier tube with a gated boxcar integrator detected SFG photons. Samples were probed under a total pressure of 1 atm.

7.3 Results and Discussion

In the synthesis, we utilized ethylene glycol as the solvent and reducing agent, and PVP was used as a capping agent. When platinum (II) acetylacetonate was used as the sole precursor, Pt nanoparticles with an average size of ~6 nm were obtained (Figure 7.1a). Interestingly, addition of the other precursor iron (II) acetylacetonate into the system posed a size-reducing effect on the produced nanoparticles. ~3 nm nanoparticles (Figure 7.1b) were produced with a precursor ratio of 9:1 (Pt/Fe). Further decreasing the Pt/Fe ratio in the precursors gave ~2 nm Pt-Fe bimetallic nanoparticles with various compositions (Figure 7.1c, 7.1e and 7.1g). If iron (II) acetylacetonate was used as the sole precursor, only aggregates of tiny Fe particles were obtained (Figure S.7.1). Control experiments indicated that iron (II) acetylacetonate decomposed at a lower temperature than platinum (II) acetylacetonate in ethylene glycol. It was thus suggested that the Fe precursor was first reduced and then the generated Fe seeds promoted the reduction of the Pt precursor through a galvanic replacement reaction which eventually formed the Pt-Fe bimetallic nanoparticles.

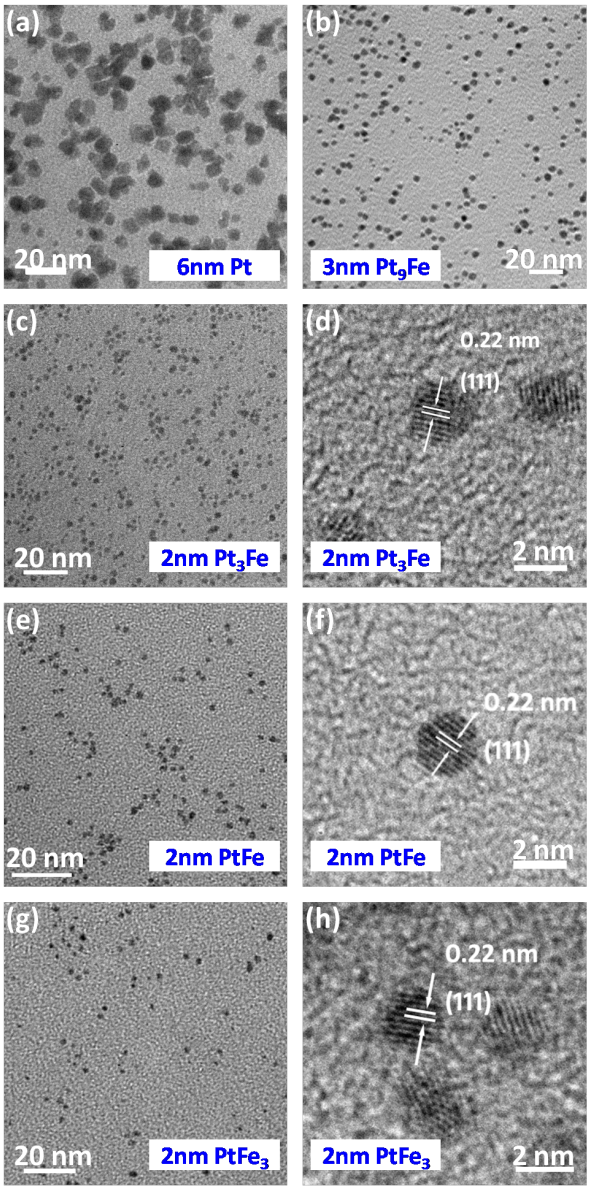

Figure 7.1: TEM images of Pt and Pt-Fe bimetallic nanoparticles with various compositions synthesized by changing the ratio of Pt and Fe precursors.

Our method afforded Pt-Fe nanoparticles with tunable composition and narrow size distribution. Transmission electron microscopy (TEM) images of the Pt_3Fe, PtFe and $PtFe_3$ nanoparticles are shown in Figure 7.1c-h. The average sizes of the three types of Pt-Fe nanoparticles were all about 2 nm, which provided a suitable system to study the composition dependence of the Pt-Fe

bimetallic nanoparticles in catalysis. High resolution TEM imaging (Figure 7.1d, 7.1f and 7.1h) revealed the lattice fringes of the nanoparticles, indicating the nanoparticles were in a disordered face-centered cubic structure (the Pt and Fe atoms were in random atomic arrangement). According to previous studies, high temperature annealing was needed to obtain intermetallic Pt-Fe alloy with an ordered face-centered tetragonal structure.[12,17] None of the as-prepared Pt-Fe nanoparticles were found to be ferromagnetic.

Compositions of the bimetallic nanoparticles were analyzed by energy dispersive spectroscopy (EDS) equipped on the TEM (Figure S.7.2). While the Fe atomic fractions measured by EDS came slightly lower than designed for all types of the bimetallic nanoparticles (Table S.7.1), they in general correlated well with the Pt/Fe ratios of the precursors used in the synthesis.

The 2 nm Pt-Fe bimetallic nanoparticles were compared with 2 nm Pt nanoparticles as catalysts for ethylene hydrogenation. The catalysts were prepared by depositing LB films of the nanoparticles on SiO_2 substrates.[18,19] The reactions took place in a batch reactor filled in sequence with 100 Torr of hydrogen, 10 Torr of ethylene and 660 Torr of helium at 25 °C.[18] Turnover frequency (TOF) was calculated based on the number of active sites derived from the surface coverage of the nanoparticles, assuming the atomic density of the spherical nanoparticle surface was the same as that of a Pt (111) surface.[19] Activation energy was obtained by running the reactions at temperatures of 25, 40, and 55 °C.

TOF and activation energy obtained for the nanoparticles are shown in Figure 7.2. A TOF of ~9.5 s^{-1} was observed for the Pt nanoparticles. This was comparable to previous results of

ethylene hydrogenation reactions catalyzed by Pt nanoparticles under similar conditions, slightly lower compared to that for a single-crystal Pt (111) surface.[10,20,21] The difference was likely due to the assumption of a (111) surface for the nanoparticles and deactivation by PVP capping. The activation energy was calculated to be ~42 kJ/mol, which was consistent with previous studies.[10,20] The Pt_3Fe nanoparticles showed an increased TOF of ~12.8 s^{-1} and a decreased activation energy of ~31 kJ/mol compared to the Pt nanoparticles. Further increase in catalytic activity was achieved by lowering the Pt/Fe ratio in the bimetallic nanoparticles. The PtFe nanoparticles exhibited a TOF of ~28.9 s^{-1}, ~3 times higher than that of the Pt nanoparticles. The activation energy was ~23 kJ/mol, which was about 50% lower than that observed for the Pt nanoparticles. With an even lower Pt/Fe ratio, the $PtFe_3$ nanoparticles showed lower TOF (~3.6 s^{-1}) than that of the Pt nanoparticles. The activation energy was measured to be ~33 kJ/mol.

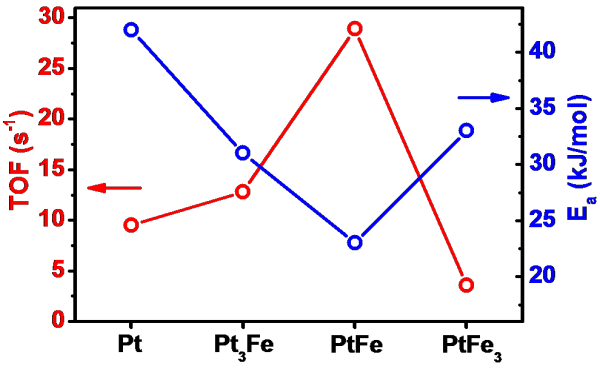

Figure 7.2: TOF and activation energy measured for ethylene hydrogenation reactions on 2 nm Pt and Pt-Fe nanoparticle catalysts. Turnover frequency was measured in a batch reactor with 10 Torr of C_2H_4, 100 Torr of H_2 and 660 Torr of He at 25 °C. Activation energy was calculated from reaction rates at 25, 40 and 55 °C.

SFG vibrational spectroscopy was employed to investigate ethylene hydrogenation intermediates adsorbed on the surface of the 2 nm Pt, PtFe and $PtFe_3$ nanoparticles, in order to elucidate the composition effect of the Pt-Fe bimetallic nanoparticles in ethylene hydrogenation catalysis from a molecular-level perspective. The Pt nanoparticles showed a low SFG background in H_2 atmosphere (Figure 7.3a black curve), owing to the disordering of PVP by H_2. Under the ethylene hydrogenation reaction condition of 35 Torr of ethylene and 100 Torr of hydrogen at 20 °C, SFG vibrational peak signals at ~2875 and ~2910 cm^{-1} were detected (Figure 7.3a red curve), corresponding to C-H stretching modes of ethylidyne and di-σ-bonded ethylene on the catalyst surface.[22,23] The PtFe nanoparticles also showed a low background in H_2 (Figure 7.3b black curve). Under reaction conditions (ethylene plus hydrogen), a lower-intensity ethylidyne peak and a higher-intensity di-σ-bonded ethylene peak were observed for the PtFe nanoparticles compared to those for the Pt nanoparticles (Figure 7.3b red curve). This indicated a lower density of ethylidyne and a higher density of di-σ-bonded ethylene adsorbed on the PtFe nanoparticle surface than on the Pt surface. This could explain the higher catalytic activity of the PtFe nanoparticles compared to Pt since ethylidyne has been identified as a less active intermediate in ethylene hydrogenation (Figure 7.3e).[22,23]

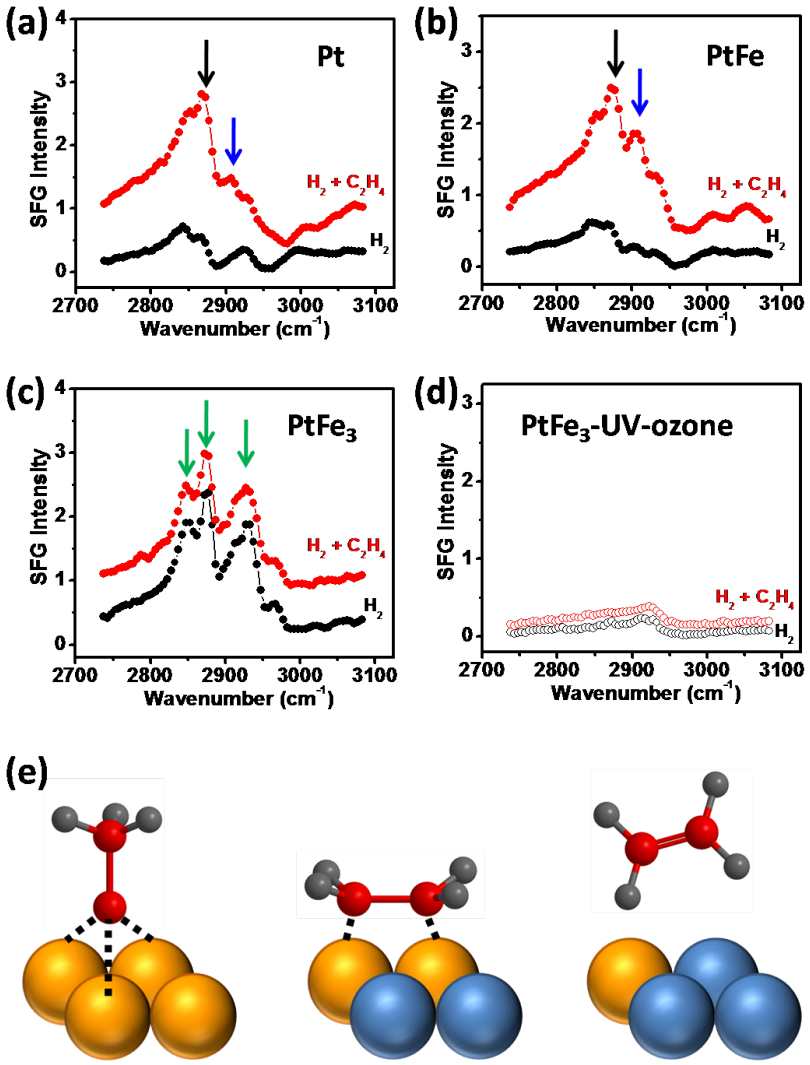

Figure 7.3: SFG vibrational spectroscopy study of ethylene intermediates adsorbed on the surface of Pt, PtFe and $PtFe_3$ nanoparticles under hydrogenation reaction conditions. (a-d) SFG vibrational spectra of 2 nm (a) Pt, (b) PtFe, (c) $PtFe_3$ and (d) UV-ozone treated $PtFe_3$ nanoparticles obtained at 20 °C under hydrogen and ethylene hydrogenation conditions. The cell was first filled with 100 Torr of H_2 and 660 Torr of Ar (black curves). Then the cell was evacuated and filled with 35 Torr of C_2H_4, 100 Torr of H_2 and 625 Torr of Ar (red curves). Black and blue arrows in (a) and (b) mark the vibrational frequencies of ethylidyne (~2875 cm^{-1}) and di-σ-bonded ethylene (~2910 cm^{-1}) adsorbed on the catalyst surface, respectively. The green arrows in (c) mark the vibrational frequencies of PVP on the nanoparticle surface. (e) Schematic

illustration of ethylidyne adsorbed on Pt surface (left), di-σ-ethylene adsorbed on PtFe surface (middle), and weak ethylene interaction with the $PtFe_3$ surface (right).

Unlike the Pt and PtFe nanoparticles, the $PtFe_3$ nanoparticles showed a high background in H_2, with the SFG peaks corresponding to the vibrational features of PVP (Figure 7.3c black curve). This was probably due to the Fe-rich surface that was in contrast to the Pt-rich surface on which the PVP became disordered when exposed to H_2.[19] Switching to the ethylene hydrogenation reaction condition had no evident effect on the SFG vibrational spectrum (Figure 7.3c red curve), which could suggest weak interactions between ethylene species and the $PtFe_3$ nanoparticle surface. However, the large SFG background from PVP made it difficult to tell slight spectral changes induced by ethylene. For this reason, we thus treated the $PtFe_3$ nanoparticles with UV-ozone to remove PVP. The SFG background signal in H_2 was significantly reduced after UV-ozone treatment (Figure 7.3d black curve), indicating extensive PVP removal. The cleaned nanoparticles were then probed by SFG vibrational spectroscopy under ethylene hydrogenation reaction conditions, and again, no ethylene intermediates were observed (Figure 7.3d red curve). It was therefore confirmed that ethylene did not produce observable reaction intermediates on the $PtFe_3$ (Figure 7.3e), which was consistent with the low reaction rate.

In order to assess the dynamic distributions and oxidation states of the two constituent elements in the Pt-Fe bimetallic nanoparticles under reaction conditions, we performed AP-XPS measurements for the 2 nm PtFe nanoparticles in different gas atmospheres at 25 °C with various incident X-ray photon energies allowing for probing the nanoparticles at different depth levels.[24-

[27] Pt 4f and Fe 3p core level spectra were recorded with incident photon energy at 370, 490 and 750 eV, corresponding to approximate probing depth of 0.7, 0.9 and 1.2 nm respectively.[28]

Deconvolution of the Pt4f and Fe 3p XPS spectra could give the oxidation state distribution of Pt and Fe.[29-33] We found the Fe atoms on the surface were more oxidized than those in the bulk of the nanoparticles. At the probing depth of ~0.7 nm from the surface, ~52% of Fe was metallic, ~10% was Fe (II), and ~38% was in 3+ oxidation state (Figure 7.4a). At larger probing depth of ~0.9 and ~1.2 nm, the percentage of Fe (0) increased to ~55% and ~65% at the expense of the decrease of Fe (III) to ~33% and ~23% respectively (Figure 7.4a). The percentage of Fe (II) showed a weak increase trend over the increased probing depth (Figure 7.4a) as Fe (II) was generally considered reductive under ambient conditions. Such changes in the oxidation states of Fe were accompanied with evident changes in the shape of the Fe 3p peaks (Figure S.7.3b, d and f). In contrast, Pt remained largely metallic over the probed depth range (Figure 7.4b) and the shape of the Pt 4f peaks did not change with incident X-ray energy (Figure S.7.3a, c and e).

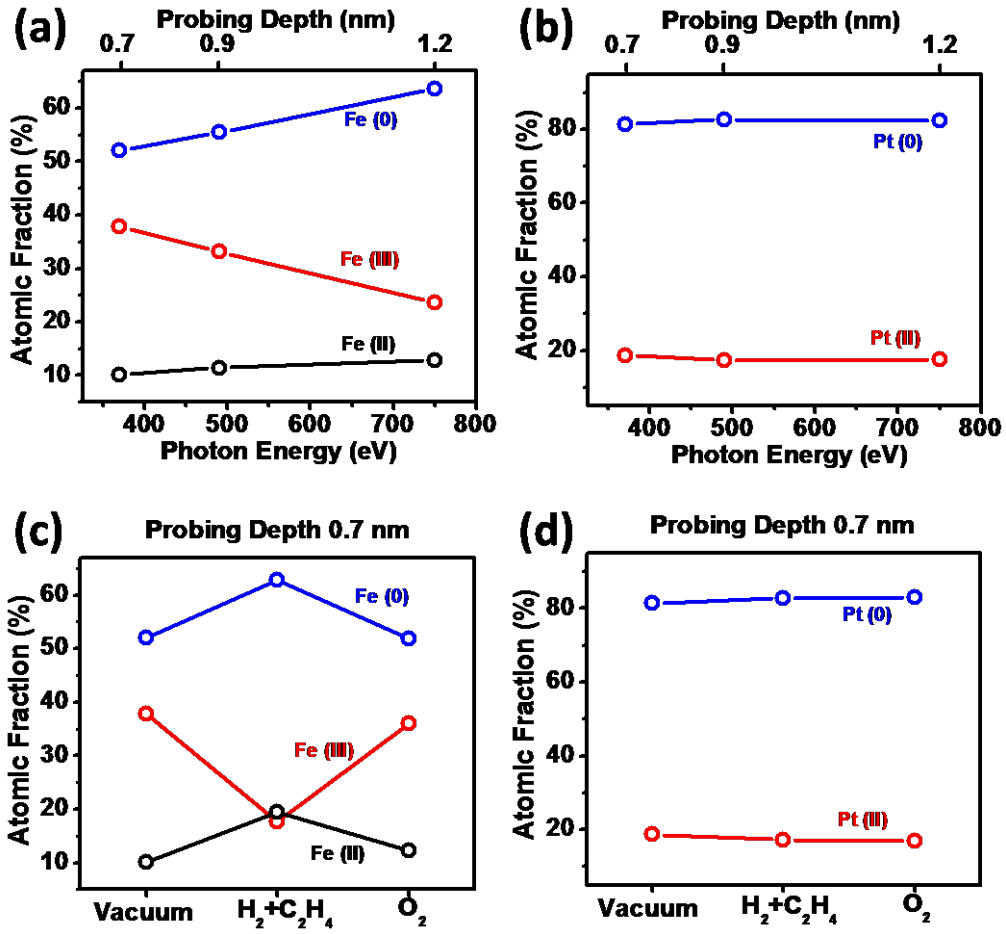

Figure 7.4: Probing depth and gas atmosphere dependent oxidation state distributions of Pt and Fe in 2 nm PtFe nanoparticles as probed by AP-XPS. Probing depth dependent oxidation states were probed by XPS in vacuum with incident X-ray photon energies of 370, 490 and 750 eV (corresponding to approximate probing depths of 0.7, 0.9 and 1.2 nm) at 25°C. Gas atmosphere dependent oxidation states were probed by XPS in H_2 + C_2H_4 (100 + 10 mTorr) and O_2 (100 mTorr) environment at 25°C with incident X-ray photon energy of 370 eV (~0.7 nm probing depth). (a) Atomic fractions of Fe species with different oxidation states in the PtFe nanoparticles vs. incident X-ray photon energy and probing depth. (b) Atomic fractions of Pt species with different oxidation states in the PtFe nanoparticles vs. incident X-ray photon energy and probing depth. (c) Atomic fractions of Fe species with different oxidation states at the

surface of the PtFe nanoparticles under various atmospheres. (d) Atomic fractions of Pt species with different oxidation states at the surface of the PtFe nanoparticles under various atmospheres.

The surface chemical states of the PtFe nanoparticles were further studied in different gas environments including hydrogen-ethylene mixture and oxygen. Low incident X-ray photon energy (370 eV) allowed for probing the few layers (~0.7 nm) of atoms on nanoparticle surface. Oxidation states of the surface Fe atoms responded to the gas environments (Figure 7.4c), resulting in changes in the shape of the Fe 3p XPS spectra (Figure S.7.4b, d and f), although the surface Pt atoms remained largely metallic (Figure 7.4d) and the shape of the Pt 4f peaks did not change with gas environment (Figure S.7.4a, c and e). In vacuum, the surface Fe atoms comprised of ~52% of Fe (0), ~10% of Fe (II) and ~38% of Fe (III) (Figure 7.4c). Upon introduction of 100 mTorr of hydrogen and 10 mTorr of ethylene into the system, Fe (0) and Fe (II) increased to ~64% and ~19% respectively and Fe (III) decreased to ~17% (Figure 7.4c). The reduction of Fe could be due to the spillover of hydrogen atoms from the co-existing Pt atoms.[34-36] After the hydrogen and ethylene were replaced by 100 mTorr of oxygen, Fe (0) and Fe (II) were partially oxidized to Fe (III), with the oxidation state distribution of Fe recovered to that in vacuum (Figure 7.4c).

Despite the significant changes in Fe oxidation states, no strong dependence of Pt/Fe ratio on XPS probing depth was observed (Figure S.7.5), which was different from some other bimetallic nanoparticle systems where the elemental composition varied through the probed depth range.[24,25] Response of the surface composition to the gas environment was also weak (Figure

S.7.5), possibly for the reason that the temperature was not high enough for surface segregation to take place.[24,25]

The 2 nm Pt and Pt-Fe bimetallic nanoparticles were also tested for catalysis of cyclohexene hydrogenation reaction at 20 °C, where cyclohexane was the only product.[37] Compared to the Pt nanoparticles, the Pt-Fe nanoparticles exhibited higher activity (Figure 7.5). Similar to the ethylene hydrogenation case, the PtFe nanoparticles were the most active catalyst for cyclohexene hydrogenation among all the Pt and Pt-Fe bimetallic nanoparticles. The TOF was ~8 times faster on the PtFe catalyst than on the Pt catalyst (Figure 7.5). The activity enhancement of Fe incorporation into Pt nanoparticle catalysts was likely realized by decreasing the concentration of relatively inactive intermediates such as 1,4-cyclohexadiene while increasing the concentration of relatively active intermediates such as di-σ-cyclohexene and 1,3-cyclohexadiene on the catalyst surface.[38,39]

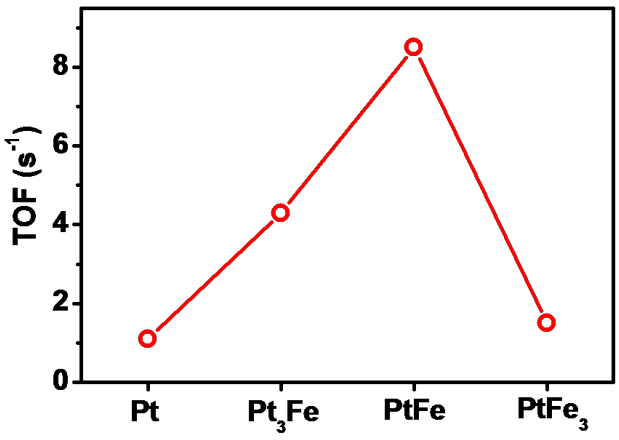

Figure 7.5: TOF measured for cyclohexene hydrogenation reaction over Pt and Pt-Fe nanoparticle catalysts. Reactions were carried out in a batch reactor filled with 10 Torr of cyclohexene, 200 Torr of H_2 and 560 Torr of He at 20 °C.

7.4 Conclusions

We investigated the influence of composition of 2 nm Pt-Fe bimetallic nanoparticles with tunable compositions on their catalytic performance of hydrogenation of organic molecules. The turnover rates of ethylene and cyclohexene hydrogenation were considerably increased by incorporation iron into platinum nanoparticle catalysts. SFG vibrational spectroscopy indicated that the activity enhancement was realized by displacing less active intermediates on the catalyst surface. AP-XPS was employed to study the dynamic composition and oxidation states of the most active 2 nm PtFe nanoparticle catalyst under reaction conditions. This work provides new insight into understanding the structure-property relationship for Pt-based bimetallic nanoparticle catalysts.

References

1 Somorjai, G. A. & Li, Y. *Introduction to surface chemistry and catalysis*. (Wiley, 2010).

2 Yu, W., Porosoff, M. D. & Chen, J. G. Review of Pt-Based Bimetallic Catalysis: From Model Surfaces to Supported Catalysts. *Chemical Reviews* **112**, 5780-5817, doi:10.1021/cr300096b (2012).

3 Greeley, J. *et al.* Alloys of platinum and early transition metals as oxygen reduction electrocatalysts. *Nature chemistry* **1**, 552-556 (2009).

4 Shiju, N. R. & Guliants, V. V. Recent developments in catalysis using nanostructured materials. *Applied Catalysis A: General* **356**, 1-17 (2009).

5 Li, Y. M. & Somorjai, G. A. Nanoscale Advances in Catalysis and Energy Applications. *Nano Letters* **10**, 2289-2295, doi:10.1021/nl101807g (2010).

6 Wang, D. & Li, Y. Bimetallic Nanocrystals: Liquid-Phase Synthesis and Catalytic Applications. *Advanced Materials* **23**, 1044-1060 (2011).

7 Gu, J., Zhang, Y. W. & Tao, F. Shape control of bimetallic nanocatalysts through well-designed colloidal chemistry approaches. *Chemical Society Reviews* **41**, 8050-8065, doi:10.1039/c2cs35184f (2012).

8 Alayoglu, S., Aliaga, C., Sprung, C. & Somorjai, G. Size and shape dependence on Pt nanoparticles for the methylcyclopentane/hydrogen ring opening/ring enlargement reaction. *Catalysis letters* **141**, 914-924 (2011).

9 Narayanan, R. & El-Sayed, M. A. Shape-dependent catalytic activity of platinum nanoparticles in colloidal solution. *Nano Letters* **4**, 1343-1348, doi:10.1021/nl0495256 (2004).

10 Tsung, C.-K. *et al.* Sub-10 nm platinum nanocrystals with size and shape control: Catalytic study for ethylene and pyrrole hydrogenation. *Journal of the American Chemical Society* **131**, 5816-5822 (2009).
11 Xu, D., Bliznakov, S., Liu, Z., Fang, J. & Dimitrov, N. Composition-Dependent Electrocatalytic Activity of Pt-Cu Nanocube Catalysts for Formic Acid Oxidation. *Angewandte Chemie* **122**, 1304-1307 (2010).
12 Sun, S. H. Recent advances in chemical synthesis, self-assembly, and applications of FePt nanoparticles. *Advanced Materials* **18**, 393-403, doi:10.1002/adma.200501464 (2006).
13 Xiang, D. & Yin, L. Well-dispersed and size-tuned bimetallic PtFex nanoparticle catalysts supported on ordered mesoporous carbon for enhanced electrocatalytic activity in direct methanol fuel cells. *Journal of Materials Chemistry* **22**, 9584-9593, doi:10.1039/c2jm16641k (2012).
14 Yin, J., Wang, J. H., Zhang, T. & Wang, X. D. Novel alumina-supported PtFe alloy nanoparticles for preferential oxidation of carbon monoxide in hydrogen. *Catalysis letters* **125**, 76-82, doi:10.1007/s10562-008-9513-6 (2008).
15 Guo, Z. *et al.* Carbon nanotube-supported Pt-based bimetallic catalysts prepared by a microwave-assisted polyol reduction method and their catalytic applications in the selective hydrogenation. *Journal of Catalysis* **276**, 314-326, doi:10.1016/j.jcat.2010.09.021 (2010).
16 Liu, Z., Tan, L. X., Li, J. & Lv, C. Easy synthesis of bimetal PtFe-containing ordered mesoporous carbons and their use as catalysts for selective cinnamaldehyde hydrogenation. *New J. Chem.* (2013).
17 Yu, C. H., Caiulo, N., Lo, C. C. H., Tam, K. & Tsang, S. C. Synthesis and fabrication of a thin film containing silica-encapsulated face-centered tetragonal FePt nanoparticles. *Advanced Materials* **18**, 2312-+, doi:10.1002/adma.200600802 (2006).
18 Baker, L. R. *et al.* Furfuraldehyde Hydrogenation on Titanium Oxide-Supported Platinum Nanoparticles Studied by Sum Frequency Generation Vibrational Spectroscopy: Acid–Base Catalysis Explains the Molecular Origin of Strong Metal–Support Interactions. *Journal of the American Chemical Society* (2012).
19 Krier, J. M. *et al.* Sum Frequency Generation Vibrational Spectroscopy of Colloidal Platinum Nanoparticle Catalysts: Disordering versus Removal of Organic Capping. *The Journal of Physical Chemistry C* **116**, 17540-17546 (2012).
20 Rioux, R. M., Song, H., Hoefelmeyer, J. D., Yang, P. & Somorjai, G. A. High-surface-area catalyst design: Synthesis, characterization, and reaction studies of platinum nanoparticles in mesoporous SBA-15 silica. *Journal of Physical Chemistry B* **109**, 2192-2202, doi:10.1021/jp048867x (2005).
21 Kuhn, J. N., Tsung, C. K., Huang, W. & Somorjai, G. A. Effect of organic capping layers over monodisperse platinum nanoparticles upon activity for ethylene hydrogenation and carbon monoxide oxidation. *Journal of Catalysis* **265**, 209-215, doi:10.1016/j.jcat.2009.05.001 (2009).
22 Cremer, P. S., Su, X., Shen, Y. R. & Somorjai, G. A. Ethylene hydrogenation on Pt (111) monitored in situ at high pressures using sum frequency generation. *Journal of the American Chemical Society* **118**, 2942-2949 (1996).

23 Kweskin, S. *et al.* High-Pressure Adsorption of Ethylene on Cubic Pt Nanoparticles and Pt (100) Single Crystals Probed by in Situ Sum Frequency Generation Vibrational Spectroscopy. *ACS Catalysis* **2**, 2377-2386 (2012).
24 Tao, F. *et al.* Evolution of Structure and Chemistry of Bimetallic Nanoparticle Catalysts under Reaction Conditions. *Journal of the American Chemical Society* **132**, 8697-8703, doi:10.1021/ja101502t (2010).
25 Tao, F. *et al.* Reaction-Driven Restructuring of Rh-Pd and Pt-Pd Core-Shell Nanoparticles. *Science* **322**, 932-934, doi:10.1126/science.1164170 (2008).
26 Grass, M. E. *et al.* New ambient pressure photoemission endstation at Advanced Light Source beamline 9.3.2. *Review of Scientific Instruments* **81**, doi: 05310610.1063/1.3427218 (2010).
27 Qadir, K. *et al.* Intrinsic Relation between Catalytic Activity of CO Oxidation on Ru Nanoparticles and Ru Oxides Uncovered with Ambient Pressure XPS. *Nano Letters* **12**, 5761-5768, doi:10.1021/nl303072d (2012).
28 Jablonski, A. & Powell, C. Elastic photoelectron-scattering effects in quantitative X-ray photoelectron spectroscopy. *Surface Science* (2011).
29 Sevilla, M., Sanchís, C., Valdés-Solís, T., Morallón, E. & Fuertes, A. Highly dispersed platinum nanoparticles on carbon nanocoils and their electrocatalytic performance for fuel cell reactions. *Electrochimica Acta* **54**, 2234-2238 (2009).
30 Murugesan, M. *et al.* Investigation of the effect of in situ annealing of FePt nanodots under high vacuum on the chemical states of Fe and Pt by x-ray photoelectron spectroscopy. *Journal of Applied Physics* **104**, 074316-074316-074315 (2008).
31 Yamashita, T. & Hayes, P. Analysis of XPS spectra of Fe< sup> 2+</sup> and Fe< sup> 3+</sup> ions in oxide materials. *Applied surface science* **254**, 2441-2449 (2008).
32 Wang, J., Mao, B., White, M., Burda, C. & Gole, J. Interactive metal ion–silicon oxidation/reduction processes on fumed silica. *RSC Advances* (2012).
33 Sasaki, K., Blowes, D. W. & Ptacek, C. J. Spectroscopic study of precipitates formed during removal of selenium from mine drainage spiked with selenate using permeable reactive materials. *Geochemical Journal* **42**, 283-294 (2008).
34 Dutta, G., Waghmare, U. V., Baidya, T. & Hegde, M. S. Hydrogen spillover on CeO2/Pt: Enhanced storage of active hydrogen. *Chemistry of Materials* **19**, 6430-6436, doi:10.1021/cm071330m (2007).
35 Yu, W. Q. *et al.* Effect of Pt impregnation on a precipitated iron-based Fischer-Tropsch synthesis catalyst. *Catalysis letters* **125**, 116-122, doi:10.1007/s10562-008-9524-3 (2008).
36 Xu, H., Fu, Q., Yao, Y. & Bao, X. Highly active Pt–Fe bicomponent catalysts for CO oxidation in the presence and absence of H2. *Energy & Environmental Science* **5**, 6313-6320 (2012).
37 Rioux, R., Hsu, B., Grass, M., Song, H. & Somorjai, G. A. Influence of particle size on reaction selectivity in cyclohexene hydrogenation and dehydrogenation over silica-supported monodisperse Pt particles. *Catalysis letters* **126**, 10-19 (2008).
38 Su, X., Shen, Y. R. & Somorjai, G. A. The surface chemistry of 1, 3-cyclohexadiene and 1, 4-cyclohexadiene on Pt (111) studied by surface vibrational spectroscopy with sum frequency generation. *Chemical physics letters* **280**, 302-307 (1997).
39 Su, X., Kung, K., Lahtinen, J., Shen, R. Y. & Somorjai, G. A. Cyclohexene dehydrogenation and hydrogenation on Pt (111) monitored by SFG surface vibrational

spectroscopy: different reaction mechanisms at high pressures and in vacuum. *Catalysis letters* **54**, 9-15 (1998).

Supplement to Chapter 7

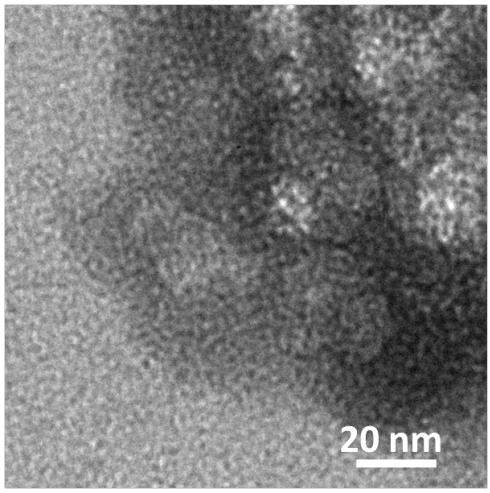

Figure S.7.1: TEM image of the product resulted from synthesis using iron (II) acetylacetonate as the only metal precursor.

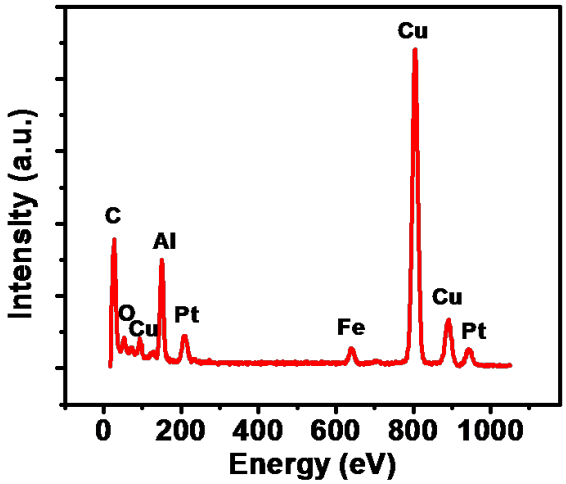

Figure S.7.2: A typical EDS spectrum of the PtFe nanoparticles. The Al and Cu signals were due to the TEM sample holder and the grid.

	Pt_9Fe (2 nm)	Pt_3Fe (2 nm)	PtFe (2 nm)	$PtFe_3$ (2 nm)
Fe%	14-21	23-29	35-49	67-75

Table S.7.1: Atomic concentration of Fe in various Pt-Fe bimetallic nanoparticles measured by EDS.

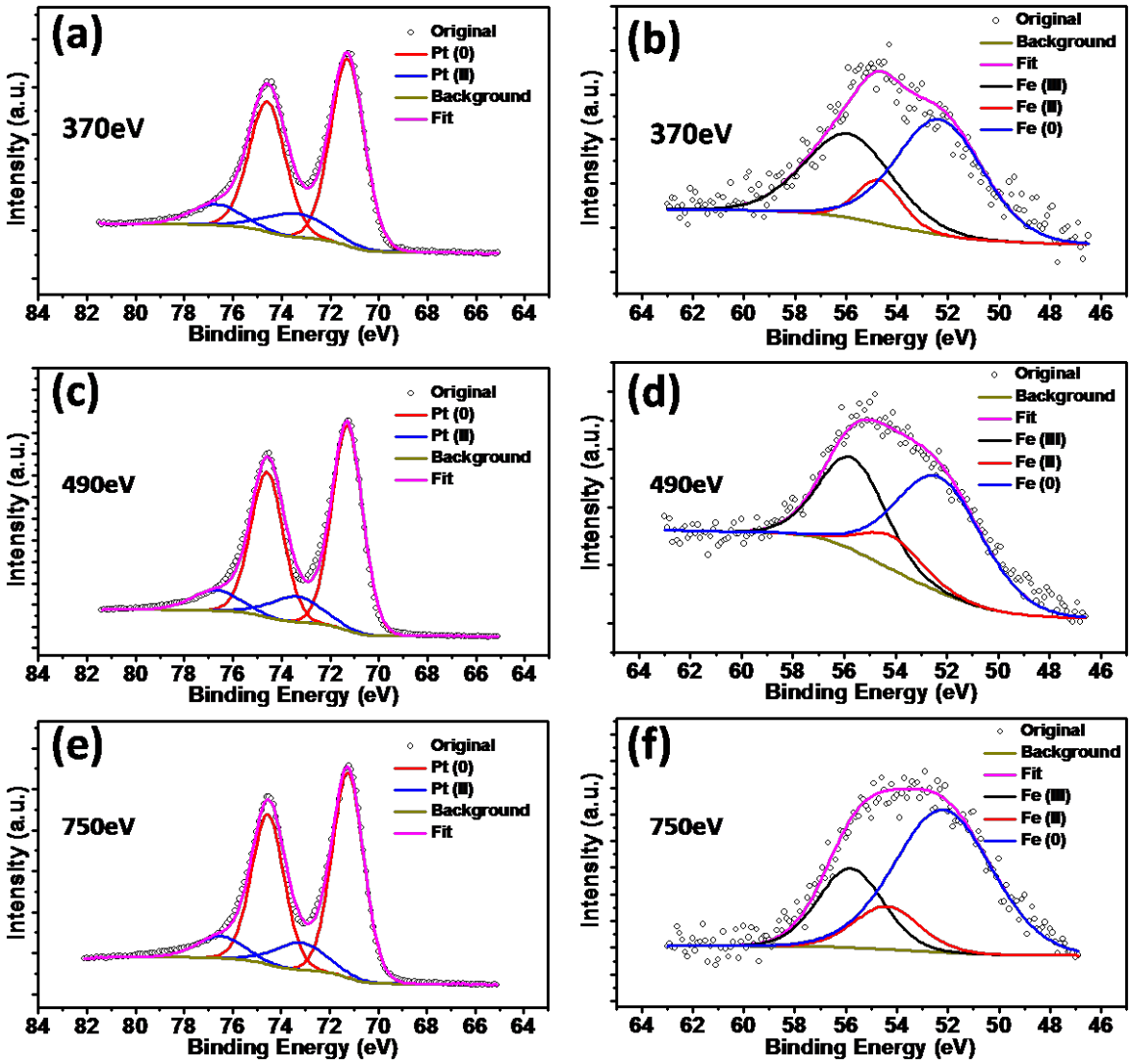

Figure S.7.3: Pt 4f (a, c, e) and Fe 3p (b, d, f) XPS spectra of 2 nm PtFe nanoparticles measured in vacuum at 25°C with incident photon energy of 370 eV (a, b), 490 eV (c, d) and 750 eV (e, f). The approximate probing depths were 0.7, 0.9 and 1.2 nm at X-ray energies of 370, 490 and 750

eV respectively. The spectra were deconvoluted to reveal the oxidation state distributions of Pt and Fe in the PtFe nanoparticles. While Pt remained mostly metallic over the three probing depths, significantly more Fe was found in reduced form with increasing probing depth.

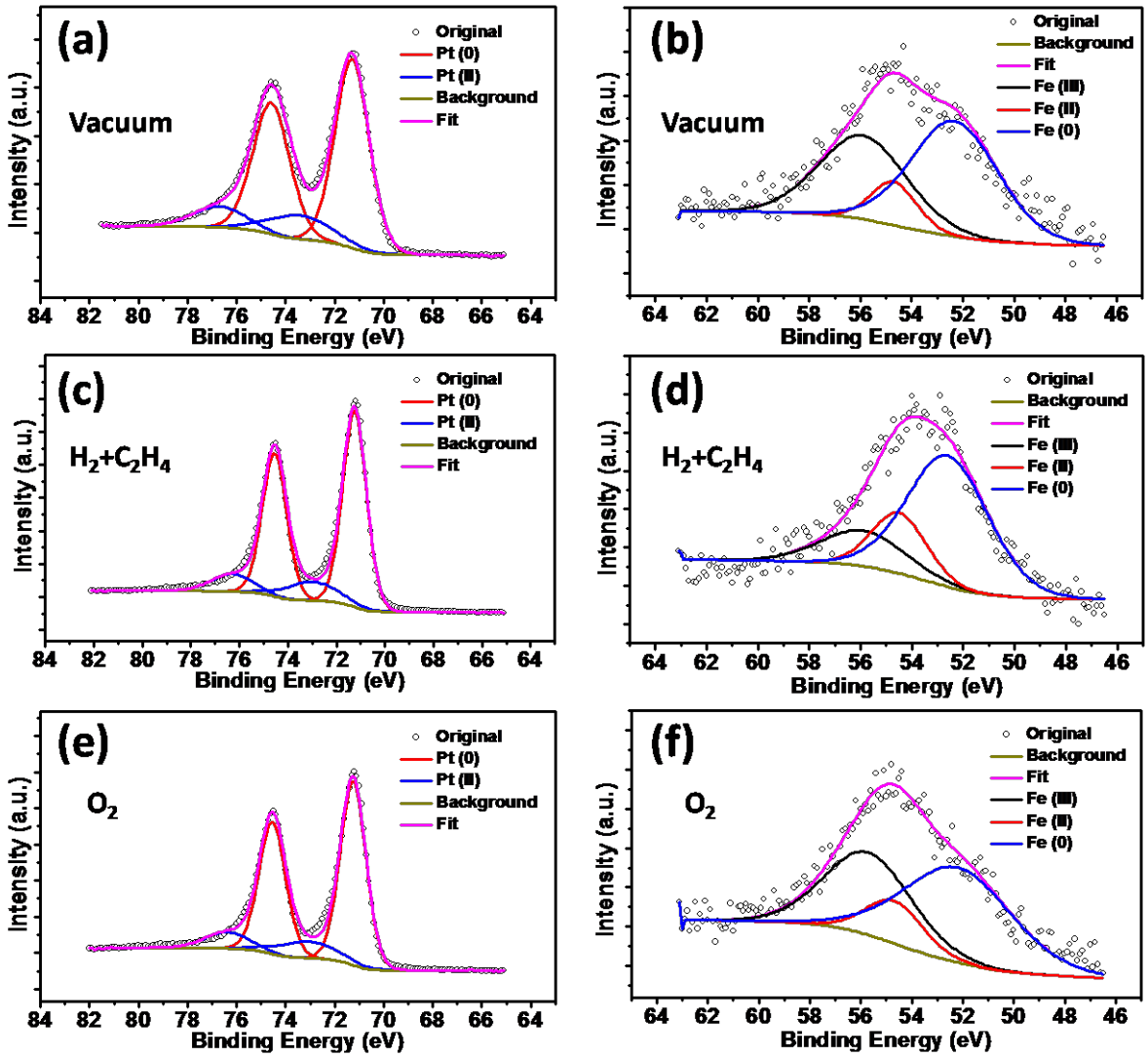

Figure S.7.4: Pt 4f (a, c, e) and Fe 3p (b, d, f) XPS spectra of 2 nm PtFe nanoparticles measured in various gas environment at 25°C with incident photon energy of 370 eV (probing depth ~0.7 nm). The spectra were deconvoluted to reveal the oxidation state distributions of Pt and Fe in the

PtFe nanoparticles under various conditions. While Pt remained mostly metallic over the three probing environments, significantly more Fe was found in reduced form in the H_2 + C_2H_4 atmosphere than in vacuum or O_2.

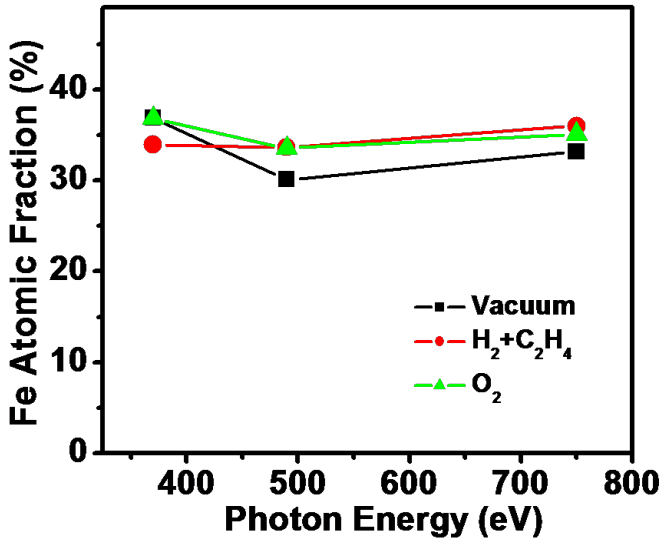

Figure S.7.5: Atomic fractions of Fe measured by XPS with various incident photon energies under various gas atmospheres for the 2 nm PtFe nanoparticles.